Ryerson University
Digital Commons @ Ryerson

Theses and dissertations

1-1-2007

A simplified model of the thermal interaction of a Venetian blind located on the indoor glazing surface of a window

Derek Roeleveld
Ryerson University

Follow this and additional works at: http://digitalcommons.ryerson.ca/dissertations
Part of the Mechanical Engineering Commons

Recommended Citation

Roeleveld, Derek, "A simplified model of the thermal interaction of a Venetian blind located on the indoor glazing surface of a window" (2007). *Theses and dissertations.* Paper 150.

This Thesis is brought to you for free and open access by Digital Commons @ Ryerson. It has been accepted for inclusion in Theses and dissertations by an authorized administrator of Digital Commons @ Ryerson. For more information, please contact bcameron@ryerson.ca.

A SIMPLIFIED MODEL OF THE THERMAL INTERACTION OF A VENETIAN BLIND LOCATED ON THE INDOOR GLAZING SURFACE OF A WINDOW

by
Derek Roeleveld
BEng, Ryerson University, Toronto, 2005.

A thesis
presented to Ryerson University

In partial fulfillment of the
requirements for the degree of
Masters of Applied Science
in the Program of
Mechanical Engineering

Toronto, Ontario, Canada, 2007
© Derek Roeleveld 2007

PROPERTY OF
RYERSON UNIVERSITY LIBRARY

AUTHOR'S DECLARATION

I hereby declare that I am the sole author of this thesis.

I authorize Ryerson University to lend this thesis to other institutions or individuals for the purpose of scholarly research.

Signature:

I further authorize Ryerson University to reproduce this thesis by photocopying or by other means, in total or in part, at the request of other institutions or individuals for the purpose of scholarly research.

Signature:

BORROWER'S PAGE

Ryerson University requires the signatures of all persons using or photocopying this thesis. Please sign below, and give address and date.

A SIMPLIFIED MODEL OF THE THERMAL INTERACTION OF A VENETIAN BLIND LOCATED ON THE INDOOR GLAZING SURFACE OF A WINDOW

Derek Roeleveld
Masters of Applied Science
Department of Mechanical & Industrial Engineering
Ryerson University, Toronto, Ontario, Canada, 2007

ABSTRACT

A simplified model was developed to predict the radiative and convective heat transfer in complex fenestrations systems, including the effect of solar radiation. The focus of the current work was on Venetian blinds mounted adjacent to the indoor window surface. From the perspective of convection, the model used a convective flat plate flow between the blind and ambient surroundings and a convective channel flow between the window and blinds. It was necessary to develop new empirical correlations to predict the average channel Nusselt numbers of the hot and cold walls separately. Therefore, a CFD study of free convection in an asymmetrically heated channel was performed. Then, the new empirical correlations were used to develop a simplified one-dimensional model of the heat transfer in the system. The radiative heat exchange between the blind, window and room was calculated using a four surface grey-diffuse model. Sample predicted results were compared with existing experimental and numerical data from the literature.

ACKNOWLEDGEMENTS

I would like to thank Dr. David Naylor for his insight and support with this thesis. Without his persistence, guidance, and enthusiasm, this thesis would not have been possible.

I would also like to thank Dr. P. H. Oosthuzien from the Department of Mechanical and Materials Engineering at Queen's University who was a collaborator on the research involved in this thesis.

I would also like to thank the Solar Buildings Research Network under the Strategic Network Grants Program of the Natural Sciences and Engineering Research Council of Canada for part of the funding for this research.

I would like to thank my friends and family for their support of my studying over the past two years. Special thanks to my parents for their encouragement and understanding. I would also like to thank Ivan Nikolaev and Fabio Almeida in the research lab for the great research related discussions we had.

TABLE OF CONTENTS

TITLE PAGE i
AUTHOR'S DECLARATION iii
BORROWER'S PAGE iv
ABSTRACT v
ACKNOWLEDGEMENTS vi
TABLE OF CONTENTS vii
LIST OF TABLES xi
LIST OF FIGURES xv
NOMENCLATURE xviii

CHAPTER 1: INTRODUCTION AND LITERATURE REVIEW

1.1 Introduction 1
1.2 Literature Review 4
  1.2.1 Studies Related to Free Convection in a Heated Vertical Channel 5
  1.2.2 Studies Related to Heat Transfer in Complex Fenestration Systems 10
    1.2.2.1 Studies Related to Solar Optical Models 10
    1.2.2.2 Studies Related to a Venetian Blind Located in between Window Panes 13
    1.2.2.3 Studies Related to a Venetian Blind Located on the Indoor Window Surface 15
1.3 Scope of Research and Problem Statement 19

CHAPTER 2: NUMERICAL MODEL

2.1 Introduction 23
  2.1.1 Problem Geometry 23
2.2 Governing Equations 23
  2.2.1 Non-Dimensionalized Governing Equations 25
2.3 Computational Domain and Boundary Conditions 27
  2.3.1 Grid Study 29

2.4 Numerical Model Validation 33

CHAPTER 3: PARAMETRIC RESULTS

3.1 Introduction 37
3.2 Results 37
  3.2.1 Hot Wall Average Nusselt Number Correlation using ΔT_{max} 42
3.3 Hot Wall Average Nusselt Number Correlation using ΔT_{eff} 43
  3.3.1 Least Sum-Squared Minimization Technique 47

CHAPTER 4: SIMPLIFIED MODEL OF A COMPLEX FENESTRATION SYSTEM

4.1 Introduction 51
  4.1.1 Effective Channel Width 53
4.2 Blind Slat Energy Balance 54
  4.2.1 Hottel's Crossed String Method 55
  4.2.2 Four Surface Radiation Model and Radiative Heat Transfer 55
  4.2.3 Channel Convective Heat Transfer 57
  4.2.4 Flat Plate Convective Heat Transfer 59
  4.2.5 Correction Functions for Flat Plate and Channel Heat Transfer 59
  4.2.6 Iteration Process of the Energy Balance 60
4.3 Convective and Radiative Heat Transfer of the Window 62

CHAPTER 5: COMPARISON OF THE SIMPLIFIED MODEL WITH EXPERIMENTAL AND NUMERICAL RESULTS

5.1 Introduction 63
  5.1.1 Least Sum-Squares Minimization 63
  5.1.2 Percent Error 64
5.2 Comparison with Experimental Results 65
5.3 Comparison with Numerical Results 66
  5.3.1 Experimental Results of a Larger Blind-to-Window Spacing and Higher Absorbed Solar Heat Flux on the Blind Slats 69

5.4 Room Heat Transfer Comparisons..70

CHAPTER 6: SUMMARY, CONCLUSIONS AND RECOMMENDATIONS

6.1 Summary and Conclusions 77
6.2 Recommendations..79

APPENDIX A: RICHARDSON EXTRAPOLATION PERFORMED ON THE NUMERICAL MODEL

A.1 Introduction..83
A.2 Calculation of the Estimation of Discretization Error for Grid 1 83
A.3 Calculation of the Estimation of Discretization Error for Grid 2 85

APPENDIX B: SAMPLE CALCULATION OF THE SIMPLIFIED MODEL

B.1 Problem Introduction..87
    B.1.1 Effective Channel Width..88
B.2 Energy Balance 88
    B.2.1 Hottel's Crossed String Method..88
    B.2.2 Calculating the Four Surface Radiation Model..90
    B.2.3 Calculating the Channel Convective Heat Transfer Rates..............................93
    B.2.4 Calculating the Flat Plate Convective Heat Transfer.......................................96
    B.2.5 Calculating the Correction Functions...96
    B.2.6 Calculating the Energy Balance 97
B.3 Comparing the Results 97

APPENDIX C: SIMPLIFIED MODEL COMPUTER CODE

C.1 Simplified Model Computer Code using Matlab(2004) 99

APPENDIX D: COMPARISON OF CURRENT MODEL RESULTS VERSUS THE NUMERICAL DATA OF COLLINS (2001)

D.1 Introduction..113
D.2 Tables of Comparison between the Numerical Data and the Current Model 113

Table 5.8: Comparison of the numerical results (Collins 2001) with the current model for $\varepsilon_w = 0.84$, $\varepsilon_b = 0.9$, $q''_{solar} = 125$ W/m^2, $T_w = 297$ K, $T_\infty = 297$ K, and L = 379.6 mm 75

Table B.1: Geometric measurements, constants, and properties of the ambient air at 297 K determined from Touloukian et al. (1970), Touloukian et al. (1975), Touloukian and Malita (1970), and Incropera and DeWitt (2002) 87

Table B.2: View factors calculated from Hottel's crossed strings method (Hottel 1967) for use in the four surface radiation model 90

Table B.2: Iterative calculation of the radiosities for the radiation model 92

Table B.3: Comparison of Collins et al. (2002b) and model sample calculations with $\varepsilon_p = 0.81$, $\varepsilon_b = 0.81$, $q''_{solar} = 150$ W/m^2, $T_w = 298$ K, and $T_\infty = 297$ K 98

Table D.1: Comparison of the numerical results (Collins 2001) with the current model for $\varepsilon_w = 0.57$, $\varepsilon_b = 0.6$, $q''_{solar} = 75$ W/m2, $T_w = 297$ K, $T_\infty = 297$ K, and L = 379.6 mm 113

Table D.2: Comparison of the numerical results (Collins 2001) with the current model for $\varepsilon_w = 0.84$, $\varepsilon_b = 0.9$, $q''_{solar} = 125$ W/m^2, $T_w = 297$ K, $T_\infty = 297$ K, and L = 379.6 mm 113

Table D.3: Comparison of the numerical results (Collins 2001) with the current model for $\varepsilon_w = 0.3$, $\varepsilon_b = 0.3$, $q''_{solar} = 75$ W/m^2, Tw = 311 K, $T_\infty = 297$ K, and L = 379.6 mm 114

Table D.4: Comparison of the numerical results (Collins 2001) with the current model for $\varepsilon_w = 0.57$, $\varepsilon_b = 0.6$, $q''_{solar} = 125$ W/m^2, $T_w = 311$ K, $T_\infty = 297$ K, and L = 379.6 mm 114

Table D.5: Comparison of the numerical results (Collins 2001) with the current model for $\varepsilon_w = 0.84$, $\varepsilon_b = 0.9$, $q''_{solar} = 25$ W/m^2, $T_w = 311$ K, $T_\infty = 297$ K, and L = 379.6 mm 114

Table D.6: Comparison of the numerical results (Collins 2001) with the current model for $\varepsilon_w = 0.57$, $\varepsilon_b = 0.3$, $q''_{solar} = 125$ W/m^2, $T_w = 297$ K, $T_\infty = 297$ K, and L = 379.6 mm....114
Table D.7: Comparison of the numerical results (Collins 2001) with the current model for $\varepsilon_w = 0.84$, $\varepsilon_b = 0.6$, $q''_{solar} = 25$ W/m^2, $T_w = 297$ K, $T_\infty = 297$ K, and L = 379.6 mm....115
Table D.8: Comparison of the numerical results (Collins 2001) with the current model for $\varepsilon_w = 0.3$, $\varepsilon_b = 0.9$, $q''_{solar} = 75$ W/m^2, $T_w = 297$ K, $T_\infty = 297$ K, and L = 379.6 mm....115
Table D.9: Comparison of the numerical results (Collins 2001) with the current model for $\varepsilon_w = 0.84$, $\varepsilon_b = 0.3$, $q''_{solar} = 25$ W/m^2, $T_w = 311$ K, $T_\infty = 297$ K, and L = 379.6 mm....115
Table D.10: Comparison of the numerical results (Collins 2001) with the current model for $\varepsilon_w = 0.57$, $\varepsilon_b = 0.9$, $q''_{solar} = 125$ W/m^2, $T_w = 311$ K, $T_\infty = 297$ K, and L = 379.6 mm....115
Table D.11: Comparison of the numerical results (Collins 2001) with the current model for $\varepsilon_w = 0.3$, $\varepsilon_b = 0.3$, $q''_{solar} = 125$ W/m^2, $T_w = 297$ K, $T_\infty = 297$ K, and L = 379.6 mm....116
Table D.12: Comparison of the numerical results (Collins 2001) with the current model for $\varepsilon_w = 0.57$, $\varepsilon_b = 0.6$, $q''_{solar} = 25$ W/m^2, $T_w = 297$ K, $T_\infty = 297$ K, and L = 379.6 mm....116
Table D.13: Comparison of the numerical results (Collins 2001) with the current model for $\varepsilon_w = 0.57$, $\varepsilon_b = 0.3$, $q''_{solar} = 75$ W/m^2, $T_w = 311$ K, $T_\infty = 297$ K, and L = 379.6 mm....116
Table D.14: Comparison of the numerical results (Collins 2001) with the current model for $\varepsilon_w = 0.84$, $\varepsilon_b = 0.6$, $q''_{solar} = 125$ W/m^2, $T_w = 311$ K, $T_\infty = 297$ K, and L = 379.6 mm....116

Table D.15: Comparison of the numerical results (Collins 2001) with the current model for $\varepsilon_w = 0.3$, $\varepsilon_b = 0.9$, $q''_{solar} = 25$ W/m^2, $T_w = 311$ K, $T_\infty = 297$ K, and L = 379.6 mm 117

LIST OF FIGURES

Figure 1.1: Diagram of a typical double pane window located in a building wall with a Venetian blind located at the indoor window surface 3

Figure 1.2: Vertical channel problem geometry and coordinate system 4

Figure 1.3: Plot of Elenbaas' (1942) experimental work and empirical correlation, showing the upper and lower asymptotes 6

Figure 1.4: Diagram of the between panes Venetian blind geometry used by Huang (2005) 11

Figure 1.5: Venetian blind located on the indoor window surface geometry....................11

Figure 1.6: Convective heat transfer model of a Venetian blind located on the indoor window surface used by Lomanowski and Wright (2007) 19

Figure 2.1: Vertical channel dimensionless computational domain 28

Figure 2.2: Grid density study of Grid 1: $T_R^* = 0.9$, $Ra_{\overline{\Delta T}}^* = 1$, and $L/b = 100$ 30

Figure 2.3: Grid density study of Grid 2: $T_R^* = 0.9$, $Ra_{\overline{\Delta T}}^* = 1000$, and $L/b = 50$ 30

Figure 2.4: Sensitivity of the overall channel average Nusselt number to the far field boundary size for Grid 1, with $T_R^* = 0.9$, $Ra_{\overline{\Delta T}}^* = 1$, and $L/b = 100$.............32

Figure 2.5: Sensitivity of the overall channel average Nusselt number to the far field boundary size for Grid 2, with $T_R^* = 0.9$, $Ra_{\overline{\Delta T}}^* = 1000$, and $L/b = 50$..........32

Figure 2.6: Validation of the numerical solution with the experimental data of Aung et al. (1972), Aihara (1963) and Elenbaas (1942)..34

Figure 2.7: Local Nusselt number distributions on the hot and cold walls comparison between the experimental (Aung et al., 1972) and the current numerical solution for $Ra_{\overline{\Delta T}}^* = 24$ and $T_R^* = 0.33$ 34

Figure 3.1: Variation of hot wall average Nusselt number based on $\overline{\Delta T}$ with respect to modified Rayleigh number 39

Figure 3.2: Variation of hot wall average Nusselt number based on ΔT_{walls} with respect to modified Rayleigh number 39

Figure 3.3: Temperature contour plots showing the lower half of the channel for $T_R^* = 0.5$: (a) in the conduction dominated regime, $Ra_{\overline{\Delta T}}^* = 0.1$ and $L/b = 100$ and (b) approaching the isolated plate regime, $Ra_{\overline{\Delta T}}^* = 1000$ and $L/b = 50$ 41

Figure 3.4: Variation of hot wall average Nusselt number based on ΔT_{max} with Respect to modified Rayleigh number 42

Figure 3.5: Hot wall average Nusselt number correlation and variation of hot wall average Nusselt number based on ΔT_{max} with modified Rayleigh number 45

Figure 3.6: Variation of weighting function A with respect to modified Rayleigh Number 45

Figure 3.7: Hot wall average Nusselt number correlation and variation of hot wall average Nusselt number based on ΔT_{eff} with modified Rayleigh number....... 48

Figure 3.8: Cold wall average Nusselt number correlation and variation of cold wall average Nusselt number based on $\overline{\Delta T}$ with modified Rayleigh number 48

Figure 4.1: (a) Window and Venetian blind problem geometry; (b) Channel and flat plate approximation geometry 52

Figure 4.2: Infinite fringe interferograms from Machin (1998) with blind slats at 90° 52

Figure 4.3: Geometry of blind-to-window spacing, n, and effective channel width, b_{eff} .. 53

Figure 4.4: Energy balance of a single blind slat 54

Figure 4.5: Hottel's crossed string method: (a) Two surfaces (strings showing); (b) Two surfaces with a common corner; (c) Two surfaces with a common corner (strings showing) 56

Figure 4.6: (a) Infinite length Venetian blind on inside surface of an infinite length window; (b) Infinite array of 4 surface boxes; (c) Four surface radiation model 57

Figure 4.7: Flowchart showing the calculation procedure of the simplified model for a specific case with given constants C_1, C_2, and N 61

Figure 5.1: Plan view of a Mach-Zehnder interferometer (not to scale) 70

Figure 5.2: Interferometric pictures of a window with a Venetian blind on the inside window surface with test conditions of $T_\infty = 22.5$ °C, $T_w = 22.5$ °C, $\varepsilon_p = 0.81$, $\varepsilon_w = 0.81$, $q''_{solar} = 125$ W/m^2, and n = 40 mm at (a)$\phi = -45°$, (b) $\phi = 0°$, (c) $\phi = 45°$ 71

Figure 5.3: Diagram of a control volume of a room with the complex fenestration system as the only source of heat input or output 72

Figure E.1: (a) Sample case 1 and (b) sample case 2 of a bidirectional flow in an asymmetrically, isothermally heated vertical channel 121

Figure E.2: Variation of the overall average Nusselt number based on $\overline{\Delta T}$ with modified Rayleigh number for bidirectional flow in a vertical channel 122

NOMENCLATURE

A	weighting function for calculating ΔT_{eff}
A_b	area of the blind slat, (m^2)
A_i	area of surface i, (m^2)
b	channel width, (m)
b_{eff}	effective channel width, (m)
B	number of blind slats
C_1, C_2	adjustable constants in F_1 and F_2
c_p	specific heat of fluid, (kJ/kgK)
E	minimization error
F_1	adjustable correction function for channel heat transfer (Eq. (4.3))
F_2	adjustable correction function for flat plate heat transfer (Eq. (4.3))
F_{i-k}	view factor from surface i to surface k
g	gravitational acceleration, (m/s^2)
G	irradition, (W)
Gr	Grashof number
h	heat transfer coefficient, (W/m^2K)
j	radiosity, (W/m^2)
k	thermal conductivity, (W/mK)
k_f	thermal conductivity of fluid, (W/mK)
L	channel height, (m)
L^*_x , L^*_y , L^*_A	dimensionless far field boundary lengths
n	blind-to-window spacing, (m)
N	adjustable constant for the effective channel width (Eq. (4.1))
Nu	local Nusselt number
$\overline{Nu}$	average Nusselt number
p	fluid pressure, (Pa)
p'	pressure defect, (Pa)

p^*	dimensionless pressure
Pr	Prandtl number
q	heat transfer rate per unit depth, (W/m)
q''	heat flux, (W/m^2)
r_c	radius of curvature of the blind slat, (m)
Ra^*	modified Rayleigh number based channel aspect ratio
Ra_L	flat plate Rayleigh number based on L
t	curvature spacing, (m)
T	temperature, (K)
T^*	dimensionless temperature
T_R^*	temperature difference ratio defined by equation (1.8)
$\overline{\Delta T}$	average channel wall temperature difference, (K)
ΔT_{eff}	effective temperature difference, equation (3.12), (K)
ΔT_{max}	maximum wall temperature difference, $T_H - T_\infty$, (K)
ΔT_{walls}	hot to cold wall temperature difference, $T_H - T_C$, (K)
u, v	fluid velocity in x, y-direction, (m/s)
u^*, v^*	dimensionless velocities
w	blind slat length, (m)
x, y	Cartesian coordinate system, (m)
x^*, y^*	dimensionless coordinate system

Greek Symbols

α	thermal diffusivity, $\alpha = \frac{k_f}{\rho c}$, (m^2/s)
β	thermal expansion coefficient of fluid, (1/K)
ε	emissivity
μ	dynamic viscosity of fluid, (Ns/m^2)
ν	kinematic viscosity of fluid, (m^2/s)
ρ	density of fluid, (kg/m^3)
ρ_i	reflectivity of surface i

ϕ	blind slat angle, (deg)

Subscripts

b	blind
ch	channel
conv	convective
C	cooler wall
f	film temperature
fd	fully developed conditions
fp	flat plate
H	hotter wall
O	overall channel
rad	radiation
solar	absorbed solar
w	window
$\overline{\Delta T}$	based on average wall temperature difference
ΔT_{eff}	based on maximum wall temperature difference
ΔT_{walls}	based on hot to cold wall temperature difference
∞	ambient

Chapter 1

Introduction and Literature Review

1.1 Introduction

Climate change is a major issue in the world. Increasing levels of carbon dioxide are affecting the world around us by increasing the temperature of the earth and decreasing the amount of snow and ice in the polar caps (IPCC 2007). Air pollution is another concern due to its affect on health issues. Many reports have been made addressing both the state of the environment and the affects of air pollution on world health. Because of this concern about the environment, it is important to develop strategies for conserving energy. The more energy that can be conserved, the less energy that needs to be produced by polluting power plants. Again, a lot of effort has been put into researching energy conservation.

One method of conserving energy is by designing buildings that are more energy efficient. This is done by using hour-by-hour building energy simulation programs, such as ESP-r (2005) and TRNSYS (2000). These programs are used to design buildings of various types and they include methods of calculating the heat transfer through a multitude of building materials, such as brick or aluminum siding, wood or steel framing, various insulation types and window designs. By using a building energy simulation program, the heating and cooling loads can be reduced by utilizing the most effective building designs. If the heating and cooling loads can be reduced, then less energy is required to maintain the building at a comfortable condition.

Of particular interest to this study is the implementation of window analysis in a building simulation program. Windows can be found in almost all buildings around the world because of the aesthetic appeal and the natural light they provide the indoor spaces. Due to the ability to increase the insulation in the walls of a building, most of the heat loss or gain through a building is due to windows. This has led to an extensive study of window performance without shading layers, which has led to double and triple glazing windows with low conductivity fill gases to reduce these heat gains and losses. Low emissivity coatings have also been utilized to reduce the heat transfer through a window.

These design specifications affect the thermal performance of the window, which affects the heating and cooling loads in a building energy simulation program. Other programs such as WINDOW 4.0 (Finlayson et al. 1993) and VISION3 (Wright 1992) offer a quick analysis of these types of window designs under different indoor and outdoor conditions without a shading layer present.

Shading devices are usually added to windows for privacy and occupant comfort, but they can have a significant impact on the performance of a window. A window with a shading device present is referred to as a complex fenestration system. One area of study is to control the natural light, called "daylighting", coming from a window by adjusting a shading device to allow the sun's light into the building. If more natural light is allowed into a building, then less energy will be used by lighting fixtures. This is one area of interest for implementation into a building energy simulation program for increasing building efficiency.

Another area of study, which is the area of this thesis, is the thermal performance of a complex fenestration system. The presence of a shading device in the window system will also have an effect on the thermal performance. Recent studies have explored the thermal effects of various shading devices in a complex fenestration system. A Venetian blind is of particular interest because the blind slat angle could potentially be adjusted to control both "daylighting" and thermal performance throughout the day. Some previous studies have shown that in certain conditions, blind slat angle can either increase or decrease the convective heat transfer of the system. Also, blind slat angle has a significant effect on the amount of solar irradiation that can be absorbed and reflected away from the interior. In terms of solar heat gain the Venetian blind can be used as shielding for incoming radiation. For example, if the blind slats are closed, solar energy is blocked from entering the indoor space through the complex fenestration system, but if the blind slats are open, some of the solar energy is allowed through the system and into the room. This is very important in determining how much heat is gained or lost into a room of a building.

Studies have investigated a Venetian blind located at both the indoor window surface and in-between the window glazings. This study concentrates on a Venetian blind mounted on the indoor window surface. Figure 1.1 shows a typical double-pane window mounted in a building wall, with a Venetian blind mounted at the indoor window surface. As the figure shows, the window is placed in the wall, with the window framing holding the window in place. The window framing has its own effects on the thermal performance of the window, but the current thesis is only interested in the center glass region, which is taken as the area of the window at a distance away from the framing. For this study, only the interaction of the Venetian blind on the indoor window glazing surface with the heat transfer is of interest.

This study is important for possible implementation into a building energy simulation program. Current building energy simulation programs only implement the effects of various types of windows without shading devices. If the heat transfer through a window and a shading device can be predicted by a correlation, then this can be used to predict the heating or cooling loads in a building energy simulation program more accurately. Other interest is in controlling the angle of a Venetian blind throughout the day to maximize the amount of heat gain or loss that can be obtained from the complex fenestration system to reduce the heating and cooling loads of a building. This is of more

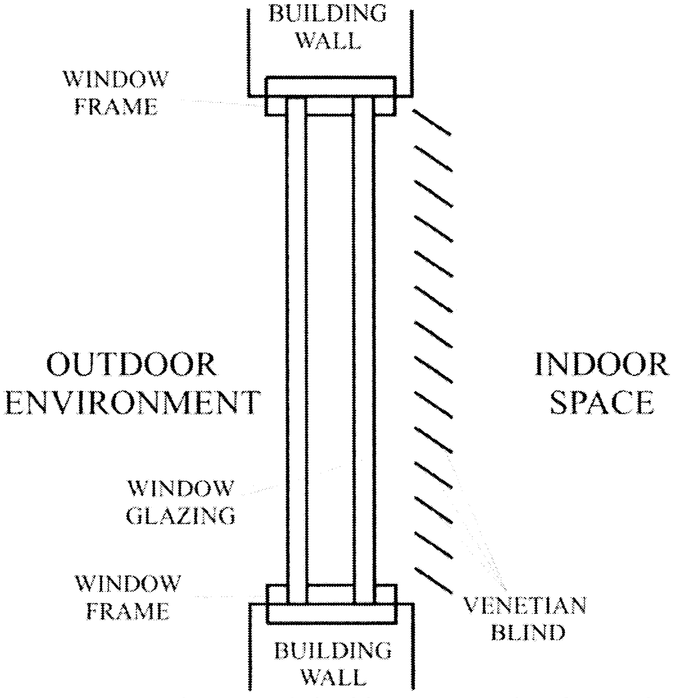

Figure 1.1: Diagram of a typical double pane window located in a building wall with a Venetian blind located at the indoor window surface.

use in residential applications where there are no occupants during the day, as personal preferences will interfere with such control systems. For example, if a person was working at a desk next to a window, a control system might want to let as much heat and sunlight into the room as possible, but the occupant would prefer to have the blind slats closed to decrease glare and decrease the amount of incoming solar heat.

1.2 Literature Review

There are two main areas of study in this thesis, which calls for a review of related literature in these two main areas. The first main area of interest, in section 1.2.1, is on the natural convective heat transfer in symmetrically and asymmetrically, isothermally heated vertical channels. The channel geometry is shown in Figure 1.2, where one channel wall is the hot wall set at temperature T_H, the other channel wall is the cold wall set at temperature T_C, and the ambient is set to temperature T_∞. The channel walls are set at height L and are separated by the channel width b. The other main area of interest, in section 1.2.2, is on complex fenestration systems, specifically studies involving a Venetian blind.

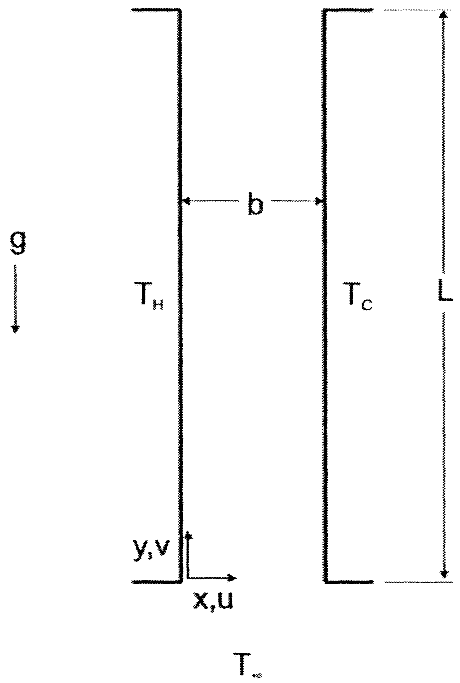

Figure 1.2: Vertical channel problem geometry and coordinate system.

1.2.1 Studies Related to Free Convection in a Heated Vertical Channel

Elenbaas (1942) was one of the first to study the heat flow of a symmetrically, isothermally heated vertical channel (in the symmetrical case: $T_H = T_C$). Using two square plates separated by varying distances and temperature differences, he was able to obtain experimental data for a wide range of modified Rayleigh numbers. The non-dimensional general-case correlation was developed through some analytical and experimental work. The overall channel average Nusselt number was determined to be:

$$\overline{Nu}_{O,\Delta T_{max}} = \frac{1}{24} Ra^{*}_{\Delta T_{max}} \left(1 - e^{\frac{-35}{Ra^{*}_{\Delta T_{max}}}} \right)^{\frac{3}{4}} \tag{1.1}$$

where $\overline{Nu}_{O,\Delta T_{max}}$ is the overall channel average Nusselt number based on a temperature difference ΔT_{max} and $Ra^{*}_{\Delta T_{max}}$ is the modified Rayleigh number based on ΔT_{max} defined as:

$$Ra^{*}_{\Delta T_{max}} = Gr_{\Delta T_{max}} \, Pr \frac{b}{L} \tag{1.2}$$

where Pr is the Prandtl number and $Gr_{\Delta T_{max}}$ is the Grashof number, defined as:

$$Gr_{\Delta T_{max}} = \frac{g\beta \Delta T_{max} b^3}{\nu_f^{\,2}} \tag{1.3}$$

and

$$\Delta T_{max} = T_H - T_\infty \tag{1.4}$$

Figure 1.3 shows a plot of some experimental data and the empirical correlation. It is important to note that the experimental data and correlation curve fits into two asymptotes. The upper limit asymptote is the isolated flat plate limit and the lower asymptote is fully developed flow.

Bodoia and Osterle (1962) developed a finite difference numerical solution for free convection in a symmetrically heated channel. A range of solutions was acquired for a Prandtl number of 0.7, where two asymptotes were discovered at high and low modified Rayleigh numbers. The lower asymptote approaches the fully developed flow equation:

$$\overline{Nu}_{O,\Delta T_{max}} = \frac{1}{24} Ra^{*}_{\Delta T_{max}} \tag{1.5}$$

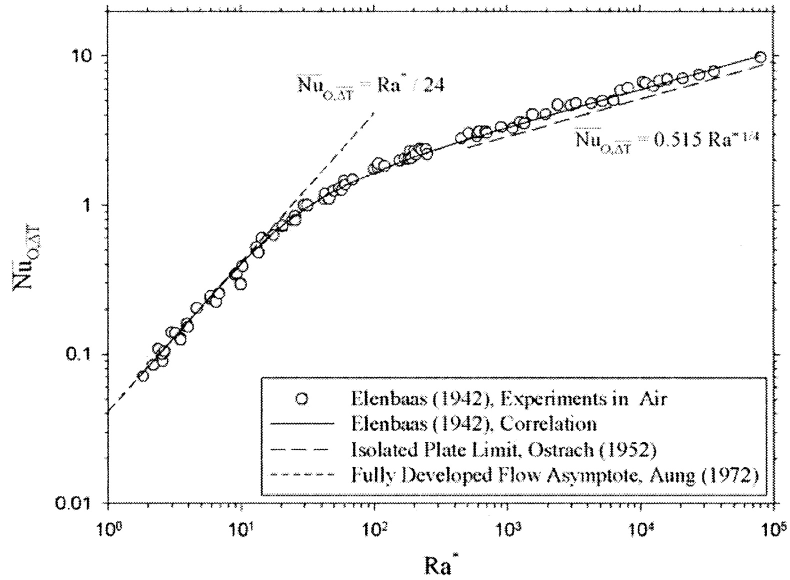

Figure 1.3: Plot of Elenbaas' (1942) experimental work and empirical correlation, showing the upper and lower asymptotes.

and at high modified Rayleigh number, the asymptote approaches the isolated plate limit:

$$\overline{Nu}_{O,\Delta T_{max}} = f\left(Ra^{*}_{\Delta T_{max}}{}^{\frac{1}{4}}\right) \tag{1.6}$$

where f was determined to equal 0.680. The results were in good agreement with Elenbaas' work, except at low modified Rayleigh number, where Elenbaas' results were slightly higher due to edge effects of his apparatus.

Miyatake and Fujii (1972) produced numerical results for asymmetrically heated channels. The specific case of interest is where one channel wall is heated and the other channel wall is thermally insulated (unheated). It was determined that for a Prandtl number of 0.7 and a modified Rayleigh number range of $10^3 > Ra^* > 300$, the upper asymptote is:

$$\overline{Nu}_{O,\Delta T_{max}} = 0.613\left(Ra^{*}_{\Delta T_{max}}\right)^{0.25} \tag{1.7}$$

and the lower asymptote is:

$$\overline{\mathrm{Nu}}_{O,\Delta T_{max}} = \frac{1}{12}\mathrm{Ra}^{*}_{\Delta T_{max}} \tag{1.8}$$

The upper asymptote showed a 19% increase over the isolated flat plate solution. The results of the numerical work were comparable to the experimental work of Aihara (1963).

Aung et al. (1972) studied the conditions of a uniform heat flux and a uniform wall temperature in an asymmetrically heated channel flow. The finite difference method was used to obtain numerical solutions and some experimental work was performed to verify the results. For the uniform wall temperature, a nearly universal curve can be used to relate the Nusselt numbers and the modified Rayleigh numbers for a wide range of wall temperature ratios, if the Nusselt numbers and modified Rayleigh numbers are defined appropriately. A wall temperature difference ratio is defined as:

$$T_R^{*} = \frac{T_C - T_\infty}{T_H - T_\infty} \tag{1.9}$$

This ratio is used to define the entire range of possible asymmetrically heated channel cases. However, the results of this work only apply to the cases where fluid flows out of the channel in one direction (unidirectional flow). This applied to cases where both channel walls are either heated at or above the ambient temperature or both cooled at or below the ambient temperature. In this study, both channel walls are heated above the ambient temperature. The average temperature of the two walls of the channel must be used as the characteristic temperature difference when calculating the Nusselt number and modified Rayleigh number:

$$\overline{\Delta T} = \frac{(T_H + T_C)}{2} - T_\infty \tag{1.10}$$

Aung (1972) also investigated the fully developed flow of an asymmetrically heated channel. It was found that at low modified Rayleigh numbers ($\mathrm{Ra}^{*} < 2$), the asymptote of the Nusselt number varied depending on the temperature ratio. The average Nusselt number at the fully developed limit can be expressed as:

$$\overline{\mathrm{Nu}}_{fd} = \frac{4T_R^{*\,2} + 7T_R^{*} + 4}{90\left(1 - T_R^{*}\right)^2}\mathrm{Ra}^{*}_{\overline{\Delta T}} \tag{1.11}$$

where:

$$Ra^*_{\overline{\Delta T}} = Gr_{\overline{\Delta T}}\, Pr \frac{b}{L} \tag{1.12}$$

and

$$Gr_{\overline{\Delta T}} = \frac{g\beta\overline{\Delta T} b^3}{{\nu_f}^2} \tag{1.13}$$

Bar-Cohen and Rohsenow (1984) used analytical expressions for the asymptotes at low and high modified Rayleigh numbers to develop correlations for various channel heating configurations. By using the curve fitting methods of Churchill and Usagi (1972), they developed correlations for both symmetrically and asymmetrically heated plates for both isoflux and isothermal plates. The new correlations were developed to fit various experimental and numerical data and the approach was validated against the work of Elenbaas (1942), Miyatake and Fujii (1972) and others. For the isothermal, symmetrically heated channel walls case the overall channel Nusselt number is:

$$\overline{Nu}_{O,\overline{\Delta T}} = \left(\frac{576}{\left(Ra^*_{\overline{\Delta T}}\right)^2} + \frac{2.873}{\sqrt{Ra^*_{\overline{\Delta T}}}} \right)^{-\frac{1}{2}} \tag{1.14}$$

and for the asymmetric case, with one channel wall isothermally heated and the other channel wall insulated (at ambient temperature):

$$\overline{Nu}_{O,\overline{\Delta T}} = \left(\frac{144}{\left(Ra^*_{\overline{\Delta T}}\right)^2} + \frac{2.873}{\sqrt{Ra^*_{\overline{\Delta T}}}} \right)^{-\frac{1}{2}} \tag{1.15}$$

Webb and Hill (1989) studied experimentally the effects of higher modified Rayleigh numbers on an asymmetrically, isothermally heated vertical channel. The $Ra^*_{\overline{\Delta T}}$ was set between 500 and 1.75 x 10^7, which is well above the deviation from the isolated flat plate limit of $Ra^*_{\overline{\Delta T}} = 400$ determined by Bar-Cohen and Rohsenow (1984). The results showed little deviation from the isolated flat plate Nusselt numbers.

A review of all the correlations was preformed by Raithby and Hollands (1998). It was determined that the best correlation for the overall channel average Nusselt number for isothermally heated channel walls is:

$$\overline{\mathrm{Nu}}_{\mathrm{O.\overline{\Delta T}}} = \left[\left(\overline{\mathrm{Nu}}_{\mathrm{fd}}\right)^{-1.9} + \left(0.618\left(\mathrm{Ra}^*_{\overline{\Delta T}}\right)^{0.25}\right)^{-1.9} \right]^{\frac{1}{-1.9}} \quad (1.16)$$

where $\overline{\mathrm{Nu}}_{\mathrm{fd}}$ is determined from equation (1.11) by Aung (1972). This is the overall channel average Nusselt number correlation that will be used in this study.

Other studies have been performed on free convective flow in isothermally heated vertical channels. Kettleborough (1971) and Nakamura et al. (1982) performed some transient numerical solutions for a symmetrically heated vertical channel. Other correlations on asymmetrically and symmetrically, isothermally heated channels have been developed experimentally by Currie and Newman (1970) and Guo et al. (1988) and numerically by Ramanathan and Kumar (1991) and Martin et al. (1991).

There are also numerous studies on symmetrical and asymmetrical uniform channel wall heat flux, such as Lauber and Welch (1966), Miyatake and Fujii (1973), and Kim et al. (1990). Other areas of study include inlet conditions of the vertical channel (Chappidi and Eno 1990), unheated entrances to a heated vertical channel (Wirtz and Haag, 1985 and Campo et al., 2004), and turbulent flow in a vertical channel (Federov and Viskanta 1997 and Habib et al. 2002). Some other variations of the classic vertical channel problem have studied recently. Numerical studies of convergent and divergent channel walls have been investigated by Bianco and Nardini (2005) and Marcondes et al. (2006). Many other sources study the effects of various objects inside a vertical channel. Studies include objects such as heated cylinders, (Marsters 1975 and Karim et al. 1986), a singular heat source (Higuera and Ryazantsev 2000), rectangular ribs on the channel walls (Desrayaud and Fichera 2002), an auxiliary plate (Andreozzi et al. 2002), a square cylinder (Khodary and Bhattacharyya 2006), and pin fins (Boyalakuntla et al 2004). These areas of study, while related, are not of direct interest to the present work.

There are many studies that have developed correlations to predict the overall heat transfer from both channel walls of a vertical channel. However in the current study the heat transfer from each individual channel wall is required. At present, simple correlations that can predict these heat transfer rates are not available in the literature. Part of the focus of this thesis is to develop these correlations for use in developing a simplified model of a window and blind system.

1.2.2 Studies Related to Heat Transfer in Complex Fenestration Systems

The hot and cold wall average Nusselt number correlations developed will be utilized in developing a simplified model to predict the heat transfer of a complex fenestration system. The simplified model is based on approximating the convective heat transfer between the Venetian blind and the indoor window surface as a vertical channel flow. The convective heat transfer of each channel wall is required to determine the heat transfer of the window and Venetian blind separately. There has been extensive research on the thermal interaction of the components in complex fenestration systems. There are three areas of study of interest to this thesis: section 1.2.2.1 solar optical models, section 1.2.2.2 thermal interaction of a Venetian blind located between window panes, and section 1.2.2.3 thermal interaction of a Venetian blind located on the indoor window surface. Solar optical models are reviewed because the results of such a model will be utilized in the current simplified model that will be developed. Even though the present study focuses on a Venetian blind located on the indoor window surface, a review of papers investigating the thermal effects of a Venetian blind located between window panes is beneficial because of the methods that can be used in the present study. Finally, a review of studies on the thermal interaction of a Venetian blind located at the indoor window surface is conducted to obtain experimental and numerical data for comparison with the present simplified model.

Figure 1.4 shows a between-panes Venetian blind geometry and Figure 1.5 shows the geometry of a Venetian blind located on the indoor window surface. The blind-to-window spacing is W_{12} and W_{23} in Figure 1.4 and n in Figure 1.5. The blind slat angle is ϕ and the blind slat length is w.

1.2.2.1 Studies Related to Solar Optical Models

It is important to understand solar optical modeling because it provides an estimate of the amount of total transmitted solar radiation, as well as the amount of absorbed solar radiation in each layer of the window and blind system. The absorbed solar radiation is then used as "inputs" into a thermal model to aide in calculating the convective, conductive, and radiative heat transfer rates in the system. Many studies

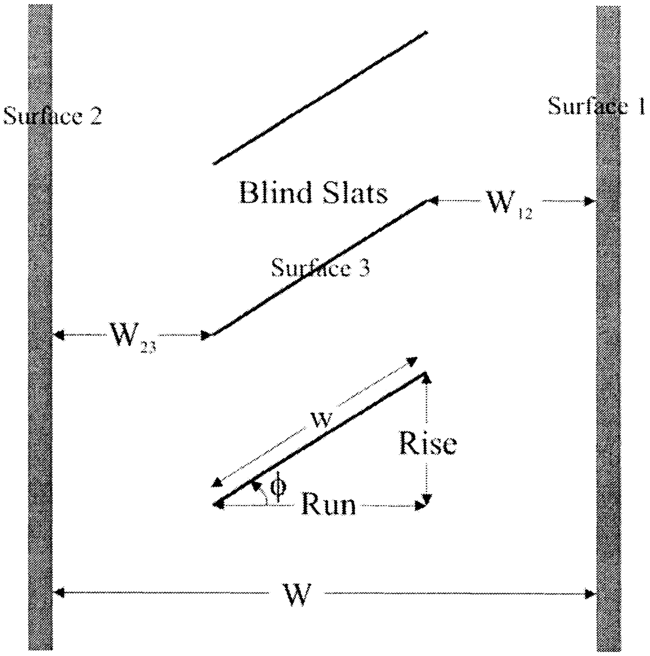
Surface 2
Surface 1
Blind Slats
W_{12}
Surface 3
W_{23}
w
Rise
ϕ
Run
W

Figure 1.4: Diagram of the between panes Venetian blind geometry used by Huang (2005).

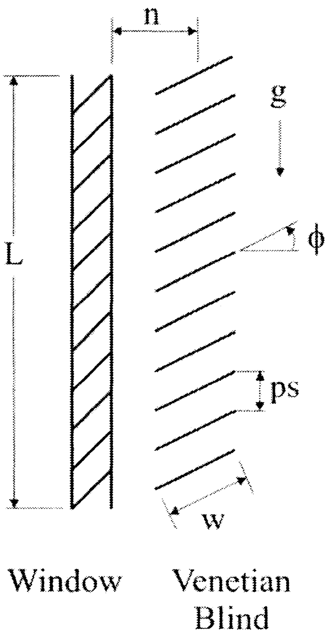
n
g
L
ϕ
ps
w
Window
Venetian Blind

Figure 1.5: Venetian blind located on the indoor window surface geometry.

have investigated the effect of how solar radiation is absorbed into various layers of a complex fenestration system.

Klems (1994a and 1994b) developed a method to predict the solar gains in a complex fenestration system. The method measures the bidirectional optical properties of a shading layer and then uses complex calculations to produce the properties of the overall complex fenestration system. Yahoda and Wright (2005) developed models for the calculation of the effective optical properties of a blind using blind slat geometry and reflectance. The models used a ray tracing technique, which is very computationally intensive.

Kotey and Wright (2006) developed a simplified solar optical model to calculate transmitted, reflected and absorbed fluxes of solar radiation for complex fenestration systems. They looked at systems with a Venetian blind located on the indoor window glazing, outdoor window glazing and between two window glazings. A detailed radiation analysis was conducted to present the hour-by-hour transmitted, reflected and absorbed solar fluxes of the window and blind surfaces for a summertime and wintertime condition. All the calculations were carried out with a blind slat angle of 10° and a blind-to-window spacing of 12.3 mm. Results were obtained for both light coloured and dark coloured blind slats.

Wright and Kotey (2006) developed a simplified optical model to calculate the beam and diffuse fluxes of each layer of a multiple layer fenestration system. This model provides full detail of the transmitted, reflected and absorbed radiation on each layer. This model was developed with computational speed and simplicity for use in hour-by-hour simulation models. An example of a multiple layer fenestration system is given in the paper: a two glazing window with an insect screen on the outdoor surface and a Venetian blind on the indoor surface. With their model, the solar absorption of the Venetian blind is 15%, the indoor glass is 10%, the outdoor glass is 15%, the insect screen is 17%, and the indoor space is 16%. These studies are of interest to the present study because the absorbed solar fluxes that are determined are used in the present simplified model. Of particular interest is the absorbed solar heat flux on the blind, which is needed for calculation in the simplified model presented in this study.

1.2.2.2 Studies Related to a Venetian Blind located in between Window Panes

Rheault and Bilgen (1989 and 1990) performed analytical and experimental studies to investigate the overall heat transfer rates of a between-panes Venetian blind system. They used climatic conditions of a typical Canadian winter and summer. Conduction effects were neglected in the blind slats and the window glazings in the analytical study. A large blind-to-window spacing was used between the blind slats and the window glazings such that the effect of the blind slats on the heat flow through the window glazings was assumed minimal when at any blind slat angle other than a closed position. Their results showed the heating and cooling load of the room could be reduced by 36% and 47% respectively with the presence of a Venetian blind. The analytical study was verified with some experimental work. Cho et al. (1995) performed a similar study using the typical climate in Seoul (South Korea) both experimentally and numerically. Again conduction was neglected, but the heating and cooling loads could be reduced by 5% and 30% respectively.

Garnet et al. (1995) determined the center-glass U-values of a between panes unheated Venetian blind system using a guarded heater plate apparatus. They studied a small blind-to-window spacing for multiple blind slat angles. Their studies showed that the presence of a Venetian blind in the window cavity improved the performance of the window when the blind slat angle increased above 35° from the horizontal, but that at a blind slat angle of 0° the performance of the window was worse than a window with no blind present. They concluded that this was because of conduction through the blind slats. They also showed that a negative blind slat angle from the hot wall had slightly better performance than a positive blind slat angle. They also concluded that more studies on this type of system were required.

Yahoda and Wright (2004b) performed studies on the effective long-wave absorbed, reflected and transmitted radiation of a Venetian blind layer using a simplified 6 surface model. This study is of great interest to the current study because a similar method of calculating the long-wave radiation between the window surface and the blind slats is utilized. Another study by Yahoda and Wright (2004a) developed a between-panes Venetian blind model to calculate the heat transfer through the system. The model used a simplified convective model and the effective long-wave radiative properties of the Venetian blind. The results of this work showed that the predicted U-values of the complex fenestration system were within 10% of the experimental results of Garnet et al. (1995).

Other experimental and numerical studies have also been performed on a Venetian blind located between two panes of a window (Huang et al. 2006 and Naylor and Lai, 2007). Simplified models have also been developed to predict the U-values of these systems (Yahoda et al. 2004a). A similar simplified model to the current study has been developed by Huang (2005) for a between-panes Venetian blind. This model uses a gray diffuse radiation analysis model along with a natural convection model to predict the heat transfer of the system. A four surface radiation model of the blind layer is used to predict the radiative heat transfer of the system. The convective heat transfer is modeled by splitting the window cavity with the Venetian blind into two enclosures, with the middle surface acting as a representation of the Venetian blind. Figure 1.4 shows the system of a Venetian blind between window glazings. The convective heat transfer of the two enclosures is calculated using vertical enclosure correlations from the literature using the effective channel widths of the two enclosures. The effective enclosure widths, W_{12} and W_{23}, are determined by:

$$W_{12} = W_{23} = \frac{W - N \cdot \mathrm{Run}}{2} \qquad (1.17)$$

where $\mathrm{Run} = w\cos(\phi)$, w is the blind slat length, ϕ is the blind slat angle, W is the width between the window panes, and N is an adjustable constant. In order to obtain accurate predicted results, the blind slat Run length is multiplied by a factor N which adjusts the widths of the two enclosures to improve the predicted results of the simplified model. This factor N was determined to be 0.7, which reduces the blind slats Run length by about 15%. This model predicted U-values within 3% of the experimental work. A method similar to that of Huang (2005) is utilized in the present study. Of particular interest to the current thesis are the effective channel width and the four surface radiation methodology.

1.2.2.3 Studies Related to a Venetian Blind located on the Indoor Window Surface

Fang and Ge (1993) experimentally studied a single and double glazed window with an unheated Venetian blind located on the indoor window surface. The blind-to-window spacing was fixed, but several different blind slat angles and temperature differences across the window were considered. They found that both the blind slat angle and window temperature difference affected the results. Two correlations were developed to determine the U-value of the system. For a single glazed window:

$$U = 0.535(2.34 + 0.73\sin\phi)(\Delta T)^{0.25} \tag{1.18}$$

where ϕ is the blind slat angle and ΔT is the temperature between the outdoor environment and the indoor space. For a double glazed window:

$$U = 0.227(1.95 + 0.32\sin\phi)(\Delta T)^{0.42} \tag{1.19}$$

The effects of different frames and outer wind velocity were also considered in further experiments with a table of correction factors being used to calculate the U-value of the window including these effects.

Klems and Kelley (1996) studied the inward flowing fraction of solar energy absorbed by each layer of a complex glazing and shading system. Using room sized calorimeters in a mobile structure capable of measuring the net heat flow through two windows under indoor and outdoor conditions, the inward flowing fraction of solar energy was measured. Multiple results were obtained for various types of window and blind combinations. A similar study was performed by Collins and Harrison (1999) in which it was determined that the inward-flowing fraction of solar energy was dependant on: the outdoor to indoor temperature difference, the blind slat angle, the exterior film coefficient, and the level of absorbed irradiance. These two studies obtain experimental results of the amount of energy that enters an indoor space from the sun through a complex fenestration system. These results can be used as comparison for numerical results and simplified models.

Machin et al. (1998) performed an experimental study on the effects of a Venetian blind located on the indoor surface of a window. The local and overall convective heat transfers of the system were examined using a Mach-Zehnder Interferometer. Flow visualization was also used to determine the buoyancy driven flow and interaction with the blind. The indoor window surface was approximated as an isothermal vertical flat plate because the center glass region was the only area of interest. The blind slats were unheated, simulating "nighttime" conditions. Three different blind-to-window spacings and four different blind slat angles were utilized to study the affects of the spacing and angle on the fluid flow of the system. The closer blind-to-window spacings showed more interaction with the fluid flow on the window, which showed that the heat transfer rate decreased because the fluid flow was deflected around the blind slats. The blind slats produce a periodic variation in the local heat transfer distribution on the plate, with sharp local maxima occurring near the inner blade tips when they are close to the plate surface. The maxima are increased when the blind is moved closer to the plate and decreased when the blind is moved away from the plate. The average convective heat transfer rates of the window and blind systems showed a slight decrease from the isolated vertical flat plate results. Their study examines the local convective heat transfer for all cases, but only a blind slat angle of 90° has the overall convective heat transfer presented. These overall convective heat transfer results are used as experimental data for the current study. It should also be noted that the temperatures of the blind slats were recorded using thermocouples, which will be used in the present study to calculate the radiative heat transfer rates of these cases.

Ye (1997) created a numerical model of a Venetian Blind located at the indoor surface of a window. The model solved only for convection and did not include any radiation. The blind slats were modeled with no curvature, zero thickness, and no conduction effects. The results showed the same trends as the experimental work of Machin et al. (1998), but the convection coefficients were lower than the experimental results. Phillips et al. (2001) created a similar numerical model including radiation and convection effects of the Venetian blind. Multiple variables were adjusted to observe the effects of the blind on the radiative and convective heat transfer of the system. The results were found be in good agreement with the experimental work of Machin et al. (1998). It was noticed that when the blind slats were placed close to the window, at low modified Rayleigh numbers the convective heat transfer was increased compared to a window without a blind present. At high modified Rayleigh numbers, the convective heat transfer was decreased at the closer blind-to-window spacing. It was also noticed that the presence of the blind reduces the radiative heat transfer significantly, even at a blind slat angle of 0°. Similar experimental studies were performed by Naylor et al. (2000) and Duarte et al. (2001).

Two studies by Collins et al. (2002a and 2002b) also examine the effects of a Venetian blind present on the indoor surface of a window. The studies represent a "daytime" model of the system including the effects of incident solar radiation. A Mach-Zehnder Interferometer was used to experimentally determine the convective heat transfer rates and temperature field. Thermocouples were placed on the surfaces of the blind slats to record the average blind temperature (which are used in the present thesis to calculate the radiative heat transfer rates). Eight different cases were performed. Four of the cases studied were for a blind temperature greater than the ambient temperature with a window temperature below the ambient temperature. Those four cases created bidirectional flow results, which are not of interest to the present study. The other four cases in which the flow is purely in the upward direction showed good agreement between the numerical and experimental results. The instantaneous heat flux agreed in both trend and magnitude and the temperature field also showed good qualitative agreement. Their study showed the same effect of maxima in the local heat flux as in Machin et al. (1998). A full parametric study of a Venetian blind on the indoor window surface was performed by Collins (2001). His study includes numerical results for a wide range of variables, such as varying the emissivites of the blind and window, the window temperature, the blind slat angle, and the incident solar radiation. The results of the full parametric study are used as comparison in the present study, along with three experimental results from Machin et al. (1998) and three experimental cases from Collins et al. (2002b). Further numerical work by Collins (2004) uncoupled the radiation and convection. The results showed that empirical correlations of the convective heat transfer coefficients could be possible.

Shahid and Naylor (2005) performed a numerical study on a more complete window and Venetian blind system. The model was developed with a full single or double glazed window and a 29 slat Venetian blind located on the indoor window surface. The model was validated against the experimental work of Machin et al. (1998) and the numerical work of Phillips et al. (2001). Summer design conditions with zero solar irradiation were used with two different blind-to-window spacings. The results showed that the blind reduces the U-value of the window by as much as 38%. It was also revealed that a blind slat angle of 90° at the closest blind-to-window spacing produced the greatest decrease in both the U-value and the radiative heat transfer. Overall they concluded that the presence of a Venetian blind on the indoor surface of the window improved the thermal performance of the system. Naylor et al. (2006) used this study as comparison to a simplified method of modeling the thermal performance effect of the Venetian blind on the window. A CFD numerical solution was used to determine the average heat transfer coefficients of the indoor glazing surface and the blind. This numerical model uses a different approach in that blind slats are set to a fixed temperature and not an equilibrium temperature based on an energy balance. A database of CFD produced coefficients are required to obtain a solution. These heat transfer coefficients were then used in a simplified model of the complete window system. They showed that a compromise is needed as increasing the blind-to-window spacing increases the U-value of the system, but this reduces the radiative heat transfer into the room. This simplified model approach showed great agreement with the numerical results of the complete window system of Shahid et al. (2005). This simplified model requires a large database of heat transfer coefficients, which for each different case a CFD solution is necessary to obtain these heat transfer coefficients. The current study is to develop a simplified model similar to Naylor et al. (2006), but to include a method of calculating the heat transfer coefficients in an empirical correlation rather than using a large database of numerical solutions.

A recent study by Lomanowski and Wright (2007) developed a simplified model similar to the current study. Three different locations for the Venetian blind were studied: on the outdoor window surface, between the window panes, and on the indoor window surface. Various radiative and convective heat fluxes were compared with the three different blind locations. Of particular interest is the case of the Venetian blind located on the indoor window surface. The convection model used in this case was modeled so that the Venetian blind was located far enough away from the indoor window surface such that there was no interaction between the two in the heat flow. Figure 1.6 shows a resistance diagram of this convection model. The blind slats are set at the blind temperature, T_1 and the indoor window surface is set to temperature, T_2. Now the blind is set at a large blind-to-window spacing so that the temperature between the window and blind is at the ambient temperature, T_{in}. The average Nusselt number of the indoor window surface and both sides of the Venetian blind were calculated from an empirical correlation for free convection on a vertical surface. This model may be applicable to large blind-to-window spacings, but it is not an accurate approximation for close blind-to-window spacings because it does not include the interaction between the Venetian blind and window in the convective heat flow. The results were taken at a single blind slat angle of 10° and at fixed emissitivies for all window and blind surfaces. The simplified model of this studyis also similar to Lomanowski and Wright (2007), but the convection model will use an approximation for the convection model that includes the interaction between the Venetian blind and the indoor window surface at close blind-to-window spacings. It will also investigate a wide range of blind slat angles and emissivities.

1.3 Scope of Research and Problem Statement

The purpose of this study is to develop a simplified model to predict the heat transfer through a complex fenestration system. The complex fenestration system of interest includes an indoor window surface and Venetian blind located at a distance from

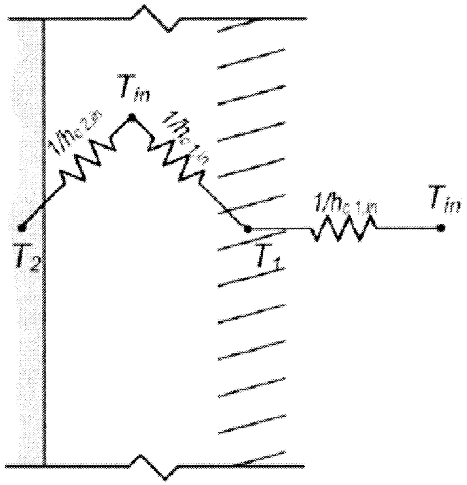

Figure 1.6: Convective heat transfer model of a Venetian blind located on the indoor window surface used by Lomanowski and Wright (2007).

the indoor window surface. The effects of a single or multiple glazing window are not considered in this study as these models are readily available in commercial fenestration analysis programs such as VISION3 (Wright 1992) and WINDOW 4.0 (Finlayson et al. 1993). The focus of this study is on the interaction of the indoor window surface and the Venetian blind. This simplified model uses a center of glass region approximation to calculate the convective and radiative heat transfer of the complex fenestration system. The simplified model will utilize both "daytime" and "nighttime" conditions as it will include solar irradiation on the blind slats. This simplified model is designed to incorporate multiple variables in calculating the heat transfer rates, such as varying the system geometry (most notably the blind-to-window spacing), the angle of the blind slats, the amount of solar irradiation on the blind slats, the window temperature, and the emissivities of the window and blind.

The simplified model is developed based on an assumption that the heat flow between the window surface and Venetian blind acts as a vertical channel flow. In order to use this assumption in the simplified model, the convective heat transfer of each wall of a vertical channel is needed for the calculation. The literature only covers correlations that determine the overall channel convective heat transfer, so a parametric study is performed to develop correlations that predict the heat transfer of each channel wall separately. This is accomplished by conducting a numerical study using Fluent (2004). This work was motivated by the application to complex fenestration systems, but the correlations developed also have utility to many other engineering applications, such as electronics cooling and simulation of flow in nuclear reactors. Once these correlations are determined, they will be used along with a radiation model to predict the radiative and conductive heat transfer of the complex fenestration system. These results will be compared with the experimental and numerical data obtained by Machin et al (1997), Collins et al. (2002b) and Collins (2001). It should be noted that the simplified model is developed based on using painted metal blinds as used in the experimental and numerical models.

This simplified model may be useful for implementation in commercial fenestration analysis programs such as WINDOW 4.0 (Finlayson et al. 1993) and VISION3 (Wright 1992) or other building simulation programs such as ESP-r (2005) and

TRNSYS (2000) so they may include the thermal effects of a Venetian blind shading layer. By using hour-by-hour solar absorption and temperature data with this simplified model, this work could be also useful in designing blind control systems to reduce heating and cooling loads throughout the day.

Chapter 2

Numerical Model

2.1 Introduction

In order to predict the heat transfer of a complex fenestration system by the simplified model developed later in this thesis, the convective heat transfer of each channel wall of an isothermally, asymmetrically heated vertical channel must be determined. This chapter develops a two-dimensional numerical model to calculate the convective heat transfer data from each channel wall separately. This data will be used in the next chapter to develop correlations for use in the simplified model. The governing equations are presented and non-dimensionalized in order to obtain a general solution set for the computational domain. The boundary conditions of the computational domain are also examined. A detailed grid study is conducted on the numerical grid, which includes grid size and far-field boundary conditions. The numerical data is then validated against the experimental work of Elenbaas (1942), Aung et al. (1972), and Aihara (1963).

2.1.1 Problem Geometry

The numerical model is developed to calculate the heat transfer of each channel wall in an isothermally, asymmetrically heated vertical channel. The vertical channel geometry is shown in Figure 1.2. The two-dimensional geometry consists of two isothermal walls of height L, separated by a channel width b. Because the two channel walls are asymmetrically heated, one channel wall is the hot wall at temperature T_H, and the other channel wall is the cold wall at temperature T_C. Both the hot wall and the cold wall are heated above the ambient temperature T_∞, such that the main buoyancy-driven flow is in the upward direction. Figure 1.2 also shows the geometry coordinate system and the direction of the gravitational force.

2.2 Governing Equations

Free convection is present in this problem because of the gravitational force and the temperature variations in the fluid. The temperature variations cause density gradients that are affected by the gravitational body force. The heat transfer due to this fluid motion is mathematically described by the governing equations. These equations are derived from the laws of mass, momentum and energy conservation. The continuity equation is Eq. (2.1), the X momentum equation is Eq. (2.2), the Y momentum equation is Eq. (2.3) and the energy equation is Eq. (2.4). The properties of the fluid are assumed to be constant and viscous dissipation is neglected in the energy equation. The flow is laminar, incompressible, two-dimensional, and at steady state for this problem.

$$\frac{\partial u}{\partial x}+\frac{\partial v}{\partial y}=0 \tag{2.1}$$

$$\rho_f\left(u\frac{\partial u}{\partial x}+v\frac{\partial u}{\partial y}\right)=-\frac{\partial p}{\partial x}+\mu_f\left(\frac{\partial^2 u}{\partial x^2}+\frac{\partial^2 u}{\partial y^2}\right) \tag{2.2}$$

$$\rho_f\left(u\frac{\partial v}{\partial x}+v\frac{\partial v}{\partial y}\right)=-\frac{\partial p}{\partial y}+\mu_f\left(\frac{\partial^2 v}{\partial x^2}+\frac{\partial^2 v}{\partial y^2}\right)-\rho_f g \tag{2.3}$$

$$u\frac{\partial T}{\partial x}+v\frac{\partial T}{\partial y}=\alpha_f\left(\frac{\partial^2 T}{\partial x^2}+\frac{\partial^2 T}{\partial y^2}\right) \tag{2.4}$$

where $\alpha_f=\frac{k_f}{\rho_f c_p}$. Since the properties are assumed to be constant, equation (2.3) shows the gravitational body force in the vertical direction as a constant. In order to include the effects of fluid density variations in the body force, the Boussinesq approximation must be introduced. This approximation only affects the fluid density variations in the gravitational body force term only. The Boussinesq approximation is accomplished by defining a pressure defect term between the local pressure and the ambient pressure in the flow field:

$$p'=p-p_\infty \tag{2.5}$$

The ambient pressure, p_∞ is the hydrostatic pressure measured from some reference point:

$$p_\infty=-\rho_\infty gy+\text{const.} \tag{2.6}$$

The change in the pressure defect is taken over the x and y directions:

$$\frac{\partial p'}{\partial x}=\frac{\partial p}{\partial x} \tag{2.7a}$$

$$\frac{\partial p'}{\partial y} = \frac{\partial p}{\partial y} + \rho_\infty g \tag{2.7b}$$

The density can be expanded as a function of the temperature:

$$\rho_f = \rho_f(T) \cong \rho_\infty + \frac{\partial \rho_f}{\partial T}(T - T_\infty) \tag{2.8}$$

The volumetric expansion coefficient is:

$$\beta = \frac{1}{V}\frac{\partial V}{\partial T} = \frac{-1}{\rho_\infty}\frac{\partial \rho_f}{\partial T} \tag{2.9}$$

The density defect then becomes:

$$\rho_f - \rho_\infty = -\rho_\infty \beta (T - T_\infty) \tag{2.10}$$

By substituting equations (2.7a) and (2.10) into equations (2.2) and (2.3), the X and Y momentum equations become:

$$\rho_f\left(u\frac{\partial u}{\partial x} + v\frac{\partial u}{\partial y}\right) = -\frac{\partial p'}{\partial x} + \mu_f\left(\frac{\partial^2 u}{\partial x^2} + \frac{\partial^2 u}{\partial y^2}\right) \tag{2.11}$$

$$\rho_f\left(u\frac{\partial v}{\partial x} + v\frac{\partial v}{\partial y}\right) = -\frac{\partial p'}{\partial y} + \mu_f\left(\frac{\partial^2 v}{\partial x^2} + \frac{\partial^2 v}{\partial y^2}\right) + \rho_\infty g \beta (T - T_\infty) \tag{2.12}$$

2.2.1 Non-Dimensionalized Governing Equations

In order to generalize the numerical solution of the governing equations over a wide range of variables, a non-dimensionalization scheme is used. The dimensionless variables are:

$$x^*, y^* = \frac{x, y}{b} \qquad u^*, v^* = \frac{u, v}{\frac{\alpha_f}{b}\Pr \mathrm{Gr}_{\Delta T_{\max}}^{\frac{1}{2}}}$$

$$p^* = \frac{p' b^2}{\mu \alpha_f \Pr \mathrm{Gr}_{\Delta T_{\max}}^{\frac{1}{2}}} \qquad T^* = \frac{T - T_\infty}{T_H - T_\infty} \tag{2.13}$$

These dimensionless variables (2.13) are substituted into the continuity equation (2.1), the energy equation (2.4), and the X and Y momentum equations (2.11) and (2.12) to produce the non-dimensionalized governing equations:

$$\frac{\partial u^*}{\partial x^*} + \frac{\partial v^*}{\partial y^*} = 0 \tag{2.14}$$

$$Gr_{\Delta T_{max}}^{\frac{1}{2}} \left(u^* \frac{\partial u^*}{\partial x^*} + v^* \frac{\partial u^*}{\partial y^*} \right) = -\frac{\partial p^*}{\partial x^*} + \left(\frac{\partial^2 u^*}{\partial x^{*2}} + \frac{\partial^2 u^*}{\partial y^{*2}} \right) \tag{2.15}$$

$$Gr_{\Delta T_{max}}^{\frac{1}{2}} \left(u^* \frac{\partial v^*}{\partial x^*} + v^* \frac{\partial v^*}{\partial y^*} \right) = -\frac{\partial p^*}{\partial y^*} + \left(\frac{\partial^2 v^*}{\partial x^{*2}} + \frac{\partial^2 v^*}{\partial y^{*2}} \right) + Gr_{\Delta T_{max}}^{\frac{1}{2}} T^* \tag{2.16}$$

$$Pr\, Gr_{\Delta T_{max}}^{\frac{1}{2}} \left(u^* \frac{\partial T^*}{\partial x^*} + v^* \frac{\partial T^*}{\partial y^*} \right) = \frac{\partial^2 T^*}{\partial x^{*2}} + \frac{\partial^2 T^*}{\partial y^{*2}} \tag{2.17}$$

where Pr is the Prandtl number and Gr is the Grashof number:

$$Pr = \frac{\nu_f}{\alpha_f} \tag{2.18}$$

$$Gr_{\Delta T_{max}} = \frac{g\beta(\Delta T_{max})b^3}{\nu_f^2} \tag{1.2}$$

where

$$\Delta T_{max} = T_H - T_\infty \tag{1.4}$$

The Prandtl number of this study is fixed at 0.707 as the fluid of interest is air near room temperature and at atmospheric pressure. The dimensionless convective heat transfer rates are presented in terms of the Nusselt number. In this study, there are a few different definitions of Nusselt number that will be introduced as they are needed to reduce confusion. The modified Rayleigh number is defined as:

$$Ra_{\overline{\Delta T}}^* = Gr_{\overline{\Delta T}}\, Pr \frac{b}{L} \tag{1.12}$$

where

$$Gr_{\overline{\Delta T}} = \frac{g\beta(\overline{\Delta T})b^3}{\nu_f^2} \tag{1.13}$$

and

$$\overline{\Delta T} = \frac{(T_H + T_C)}{2} - T_\infty \tag{1.10}$$

2.3 Computational Domain and Boundary Conditions

In the present study, the non-dimensionalized governing equations (2.14) to (2.17) are solved numerically using the commercial CFD code Fluent (2004). A control-volume formulation with a second-order upwind scheme for evaluation of the convective terms is used in this solution. The SIMPLEC algorithm (Van Doormal and Raithby 1984) was used for the pressure-velocity coupling and the PRESTO (Patankar, 1980) option was used to discretize the pressure. Under-relaxation and incremental loading was required for solutions at the higher modified Rayleigh numbers, where the relaxation parameters were between 0.3 and 0.7. The two-dimensional computational domain that equations (2.14) through (2.17) are used to solve is shown in Figure 2.1. Unheated entrances and varying entrance geometry could be used to develop correlations that are more accurate for the specific application to the window and blind geometry of the simplified model developed in Chapter 4, but the computational domain is developed to create general case correlations that can be used in a wider range of engineering applications. The boundary conditions of the computational domain are applied to the solution of the continuity, X and Y momentum, and energy equations. The non-dimensional boundary conditions are:

$$
\begin{array}{llll}
u^* = v^* = 0,\ T^* = 1 & \text{for } x^* = 0,\ 0 \le y^* \le L/b & \text{(BC)} & \\
u^* = v^* = 0,\ T^* = T_R^* & \text{for } x^* = 1,\ 0 \le y^* \le L/b & \text{(DE)} & \\
u^* = v^* = 0,\ \dfrac{\partial T^*}{\partial y^*} = 0 & \text{for } 0 \le x^* \le -L_A^*,\ y^* = 0 & \text{(AB)} & \\
u^* = v^* = 0,\ \dfrac{\partial T^*}{\partial y^*} = 0 & \text{for } 1 \le x^* \le L_A^*,\ y^* = 0 & \text{(EF)} & (2.19) \\
\text{Pressure Inlet, } v^* = T^* = 0 & \text{for } x^* = -L_A^*,\ -L_y^* \le y^* \le 0 & \text{(AH)} & \\
\text{Pressure Inlet, } v^* = T^* = 0 & \text{for } x^* = L_A^* + 1,\ -L_y^* \le y^* \le 0 & \text{(FG)} & \\
\text{Pressure Inlet, } u^* = T^* = 0 & \text{for } -L_A^* \le x^* \le L_A^* + 1,\ y^* = -L_y^* & \text{(HG)} & \\
\text{Pressure Outlet, } u^* = 0 & \text{for } 0 \le x^* \le 1,\ y^* = L/b & \text{(CD)} &
\end{array}
$$

The hot wall of the vertical channel is surface BC, which is set at a fixed temperature (1) in this non-dimensional case. Surface DE is the cold wall of the vertical channel and it is also set at a fixed temperature (T_R^*). A channel wall temperature difference ratio is defined as:

$$T_R^* = \frac{T_C - T_\infty}{T_H - T_\infty} \tag{1.9}$$

The temperature difference ratio is designed to vary from 0 to 1 so that the channel is heated symmetrically when $T_R^* = 1$ and the cold wall is at the ambient temperature when $T_R^* = 0$. Three different channel wall temperature difference ratios are used in this study to obtain data for varying asymmetrical heating of the vertical channel. Both surfaces BC and DE have no-slip and impermeability conditions applied. No-slip and impermeability conditions are also applied to surfaces AB and EF, which are adiabatic surfaces. The fluid flows out of the computational domain at boundary CD where a pressure outlet is defined. The pressure defect is set to zero at this boundary and the fluid leaves normal to the boundary. A pressure inlet condition is applied to boundaries AH, FG, and HG where the fluid is entrained into the computational domain normal to the boundary. The fluid

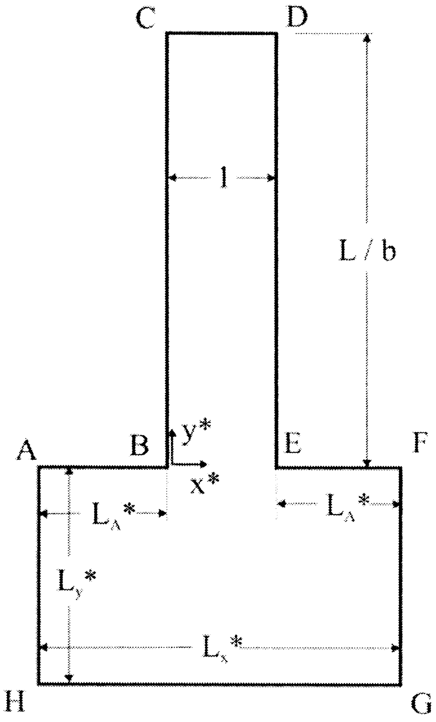

Figure 2.1: Vertical channel dimensionless computational domain.

enters the computational domain at ambient temperature with the pressure defect set to zero at these boundaries.

2.3.1 Grid Study

An extensive grid study was performed to ensure that the numerical solution was grid independent. There are two grids used in this study to obtain a wide range of data from a modified Rayleigh number of 0.1 to a modified Rayleigh number of 10,000. For the lower modified Rayleigh number range, $Ra^*_{\overline{\Delta T}} = 0.1$ to $Ra^*_{\overline{\Delta T}} = 100$, Grid 1 is used with a channel aspect ratio, $L/b = 100$. For the higher modified Rayleigh number range, $Ra^*_{\overline{\Delta T}} = 200$ to $Ra^*_{\overline{\Delta T}} = 10{,}000$, Grid 2 is used with a channel aspect ratio of 50. It should be noted that both grids have a non-uniform grid, with higher node density close to the channel walls and the entrance to the channel. Both the grid density and the far-field boundary conditions were tested on Grid 1 and Grid 2. The numerical solution was solved making sure that iterative convergence had been achieved. This occurred when the momentum, continuity and energy equations normalized residuals were reduced to less than 10^{-4}.

Figure 2.2 shows the grid density study performed on Grid 1, which was solved for $T^*_R = 0.9$ and $Ra^*_{\overline{\Delta T}} = 1$. A numerical solution was calculated for multiple grid sizes, starting with the smallest grid size of 2,876 nodes and then doubling the grid size until a grid size of 80,241 nodes. The graph shows that the overall average Nusselt numbers from the numerical solutions of all the different grid sizes are reasonably close. From Figure 2.2, a grid size of 21,076 nodes was chosen as sufficient for the numerical model. This grid size shows only a 0.17% change from a grid size of 10,391 nodes and a 0.14% change from a grid size of 41,956 nodes. The graph also shows that the curve is approaching an asymptote as the grid size increases, which looks to be fairly close to the grid size of 21,076 nodes. Figure 2.3 shows the grid density study of Grid 2, which is solved for $T^*_R = 0.9$ and $Ra^*_{\overline{\Delta T}} = 1000$. The same grid size of 21,076 nodes was chosen, as there is only a 0.03% change from 10,391 nodes and 0.03% change from 41,956

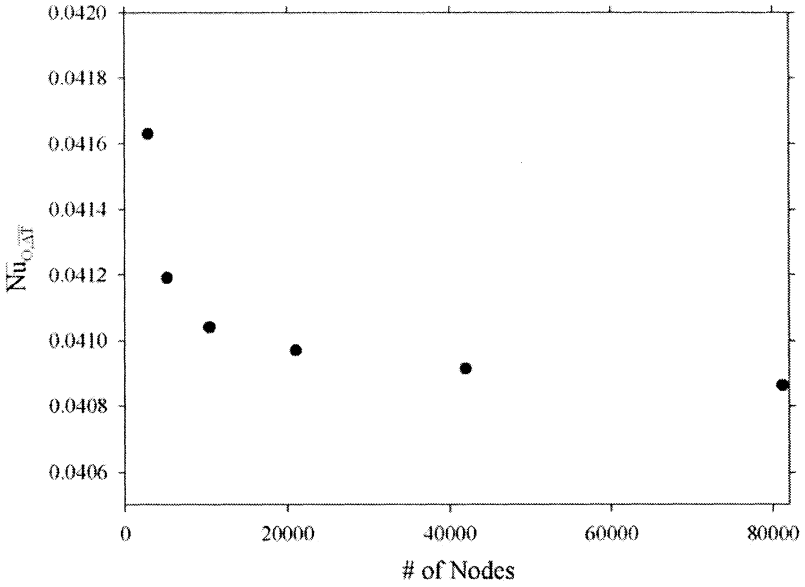

Figure 2.2: Grid density study of Grid 1: $T_R^* = 0.9$, $Ra_{\overline{\Delta T}}^* = 1$, *and* $L/b = 100$.

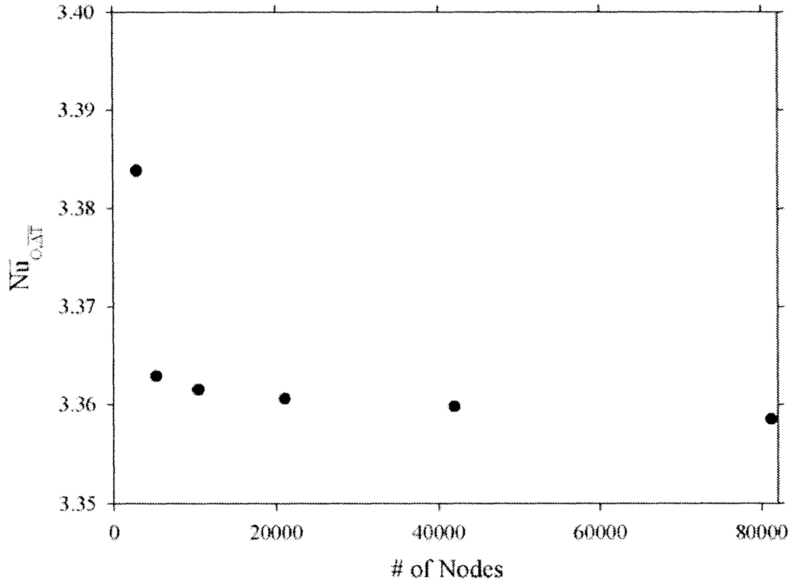

Figure 2.3: Grid density study of Grid 2: $T_R^* = 0.9$, $Ra_{\overline{\Delta T}}^* = 1000$, *and* $L/b = 50$.

nodes. The graph shows the same characteristics of the Grid 1 grid density study, with the results approaching an asymptote as the grid size increases.

Figure 2.4 shows the far-field boundary study of Grid 1 conducted at $T_R^* = 0.9$ and $Ra_{\overline{\Delta T}}^* = 1$. Boundary sizes of $L_x^* = L_y^* = 3$ to $L_x^* = L_y^* = 81$ were used to determine a suitable distance for the entrance region boundary. From the graph of Figure 2.4, a boundary of $L_x^* = L_y^* = 21$ was determined to be adequate for the numerical model. This boundary was chosen as the graph shows minor changes in the overall average Nusselt number at larger boundaries, but slightly larger changes at smaller boundaries. A boundary size of $L_x^* = L_y^* = 21$ has a 0.09% change from $L_x^* = L_y^* = 11$ and a 0.15% change from $L_x^* = L_y^* = 41$. Figure 2.4 shows an asymptote as the computational domain boundary size is increased. Grid 1 was created with 20,681 nodes, $L_x^* = L_y^* = 21$, and a channel aspect ratio, $L/b = 100$ to obtain results for $Ra_{\overline{\Delta T}}^* = 0.1$ to $Ra_{\overline{\Delta T}}^* = 100$. Figure 2.5 shows the far-field boundary study of Grid 2 at $T_R^* = 0.9$ and $Ra_{\overline{\Delta T}}^* = 1000$. Again, the boundary size of $L_x^* = L_y^* = 21$ was chosen as there is only 0.06% change from $L_x^* = L_y^* = 11$ and 0.03% change from $L_x^* = L_y^* = 41$. A channel aspect ratio, L/b of 50, was used for Grid 2 to obtain results for $Ra_{\overline{\Delta T}}^* = 200$ to $Ra_{\overline{\Delta T}}^* = 10000$ with a grid size of 20,681 nodes and the boundary conditions of $L_x^* = L_y^* = 21$.

A Richardson extrapolation (Celik 2006) was performed at $Ra_{\overline{\Delta T}}^* = 1$ for Grid 1 with a channel aspect ratio of 100 and at $Ra_{\overline{\Delta T}}^* = 1000$ for Grid 2 with a channel aspect ratio of 50. For this method, three different grid sizes are utilized, so for these two numerical grids, the three grid sizes are 21,076 nodes, 41,956 nodes, and 81,201 nodes. With these three grid sizes, a critical variable is determined, which is $Nu_{O,\overline{\Delta T}}$ in this case. Grid 1 at $Ra_{\overline{\Delta T}}^* = 1$ has a numerical uncertainty of 0.94% and Grid 2 at $Ra_{\overline{\Delta T}}^* = 1000$ has a numerical uncertainty of 0.04%. For a detailed calculation of the Richardson extrapolation for both numerical grids, see Appendix A.

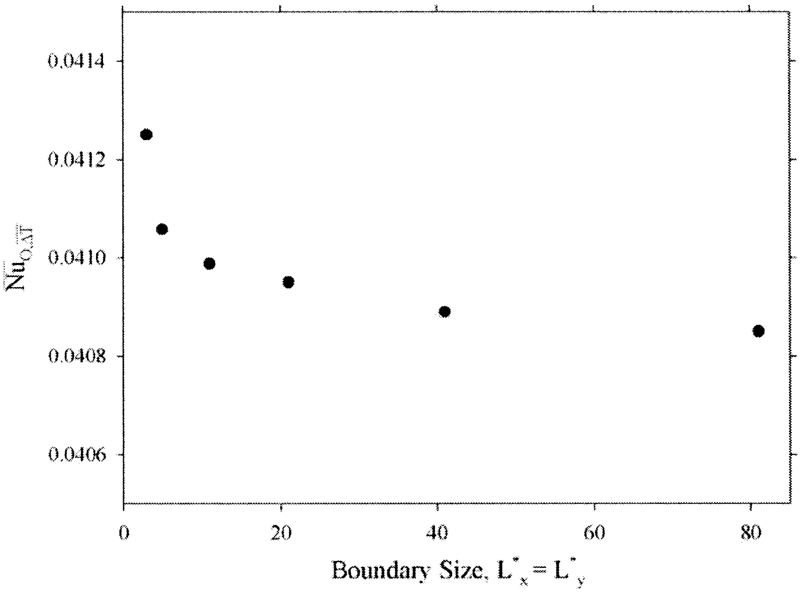

Figure 2.4: Sensitivity of the overall channel average Nusselt number to the far field boundary size for Grid 1, with $T_R^* = 0.9$, $Ra^*_{\overline{\Delta T}} = 1$, and $L/b = 100$.

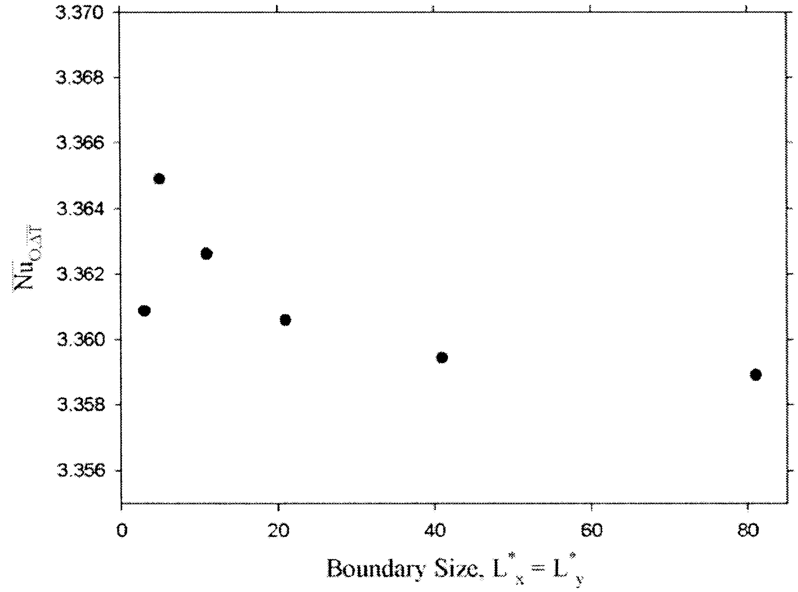

Figure 2.5: Sensitivity of the overall channel average Nusselt number to the far field boundary size for Grid 2, with $T_R^* = 0.9$, $Ra^*_{\overline{\Delta T}} = 1000$, and $L/b = 50$.

2.4 Numerical Model Validation

The numerical model is validated against the overall channel average Nusselt number, which has been extensively studied (Elenbaas 1942, Aung 1972, and Bar-Cohen and Rohsenow 1984). The overall channel average Nusselt number is defined as:

$$\overline{\mathrm{Nu}}_{\mathrm{O},\overline{\Delta T}} = \frac{qb}{2Lk_f\overline{\Delta T}} \tag{2.20}$$

where q is the convective heat transfer rate per unit depth of both channel walls. It has been shown (Aung et al. 1972) that the appropriate characteristic temperature difference that gives the best correlation for the overall channel average Nusselt number is $\overline{\Delta T}$. However, the appropriate temperature difference that should be used to correlate the hot and cold wall average Nusselt Numbers is unclear. In fact, this is discussed in detail in the next chapter when fitting a correlation to the data.

Figure 2.6 shows a comparison of the overall channel average Nusselt number between the current numerical solution and some experiment work from the literature (Elenbaas 1942, Aung et al. 1972, and Aihara 1963). The upper and lower asymptotes are also present in Figure 2.6, with the upper asymptote being the isolated flat plate limit developed by Ostrach (1953) and the lower asymptotes being the fully developed flow limit developed by Aung (1972). It should be noted that the numerical solutions of only two of the three channel wall temperature difference ratios are presented on the graph in Figure 2.7, $T_R^* = 0$ and $T_R^* = 0.9$. The numerical data agrees well with the experimental data.

Interferometric measurements of the local Nusselt number distribution on the hot and cold walls of an asymmetrically heated vertical channel were conducted by Aung et al. (1972). These results are used for comparison with the current numerical results in Figure 2.7. The local Nusselt numbers of the hot and cold wall are:

$$\mathrm{Nu}_{y,H} = \frac{-k_{f,H}\left.\frac{dT}{dx}\right|_{x=0} b}{k_f\left(T_H - T_C\right)} \qquad \mathrm{Nu}_{y,C} = \frac{-k_{f,C}\left.\frac{dT}{dx}\right|_{x=b} b}{k_f\left(T_H - T_C\right)} \tag{2.26}$$

where $k_{f,H}$ is the conductivity of the fluid near the hot channel wall and $k_{f,C}$ is the conductivity of the fluid near the cold channel wall. The channel wall temperature

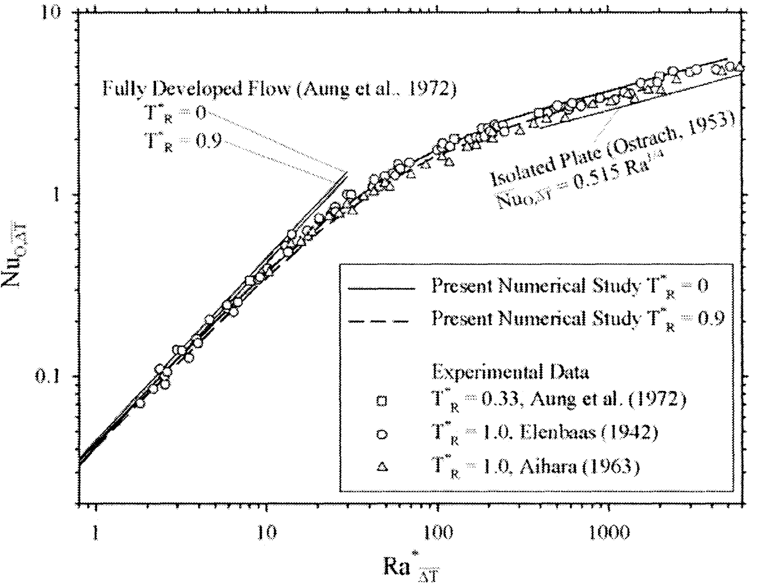

Figure 2.6: Validation of numerical solution with experimental data of Aung et al. (1972), Aihara (1963) and Elenbaas (1942).

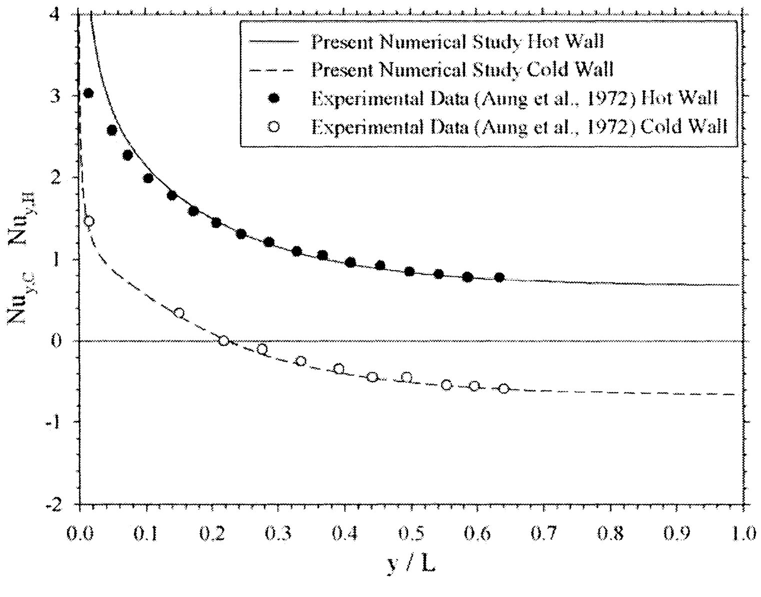

Figure 2.7: Local Nusselt number distributions on the hot and cold walls comparison between the experimental (Aung et al., 1972) and the current numerical solution for $Ra^*_{\overline{\Delta T}} = 24$ *and* $T^*_R = 0.33$.

difference ratio is T_R^* = 0.33 and the modified Rayleigh number is $Ra_{\overline{\Delta T}}^*$ = 24 for the case in Figure 2.7. The comparison shows very good agreement between the experimental and numerical results except near the leading edge of the hot wall. This discrepancy was also discovered by Aung et al. (1972), who explained that the temperature was slightly lower due to the apparatus construction.

Another issue of note when looking at two-dimensional vertical channels is the effect of conduction losses out of the ends of the channel. At low modified Rayleigh numbers in short channels, it was shown by Ramanathan and Kumar (1991) that the conduction loses can become significant. The numerical model of this study uses a dimensionless channel aspect ratio of 100 at low modified Rayleigh numbers, which is sufficiently long enough to neglect the effect of the conduction losses for the modified Rayleigh numbers of interest in this study. With such a long channel, the overall channel average Nusselt numbers calculated by the numerical solution are accurate within the fully developed flow asymptote as can be seen in Figure 2.6.

Chapter 3
Parametric Results

3.1 Introduction

Once the numerical model is developed and validated, a parametric study is performed. Average Nusselt number data is obtained for multiple temperature difference ratios for a wide range of modified Rayleigh numbers using two channel aspect ratios. This data is then plotted using various characteristic temperature differences in the hot wall average Nusselt number. However, it is shown that the hot wall average Nusselt number data is not easily correlated. The Churchill and Usagi (1972) correlation technique is used to develop a correlation that does not clearly fit the numerical data. It is then determined that a blended characteristic temperature difference is best suited and an equation is developed to calculate this blended characteristic temperature difference. The Churchill and Usagi (1972) correlation technique is used with the upper and lower asymptotes and a hot wall average Nusselt number correlation is created that fits the numerical data. A cold wall average Nusselt number is then developed with the overall channel average Nusselt number and the hot wall average Nusselt number. Finally, the sum-squared error minimization technique is explained.

3.2 Results

The average Nusselt number data was obtained for three channel wall temperature difference ratios, $T_R^* = 0$, 0.5, and 0.9, over a modified Rayleigh number range of $0.1 \leq Ra^*_{\overline{\Delta T}} \leq 10^4$. It should be noted that a channel aspect ratio of 100 was used for the numerical solution over the modified Rayleigh number range of $0.1 \leq Ra^*_{\overline{\Delta T}} \leq 100$ and a channel aspect ratio of 50 was used for modified Rayleigh numbers of $100 < Ra^*_{\overline{\Delta T}} \leq 10^4$. This data was used to develop a correlation to predict the hot and cold wall average Nusselt numbers of the asymmetrically heated channel.

As a side comment, it must be mentioned that the case of $T_R^* = 1$ is not included in this parametric study. For $T_R^* = 1$, the heat transfer rate will approach zero as

$Ra^*_{\overline{\Delta T}} \rightarrow 0$, since both walls of the channel are at the same temperature. However, this does not present a problem. For symmetrical heating, the hot and cold wall average Nusselt numbers are equal to the overall channel average Nusselt number, which can be calculated from existing correlations in the literature. So, this case can be excluded without loss of generality.

A problem occurs in the selection of the appropriate characteristic temperature difference for correlating the hot wall average Nusselt number. Figure 3.1 illustrates this problem when using $\overline{\Delta T}$ as the characteristic temperature difference. The hot wall average Nusselt number based on $\overline{\Delta T}$ as the characteristic temperature difference is defined as:

$$\overline{Nu}_{H,\overline{\Delta T}} = \frac{q_H b}{L k_f \overline{\Delta T}} \tag{3.1}$$

where q_H is the convective heat transfer rate per unit depth of the hot wall. The characteristic temperature difference ratio of $\overline{\Delta T}$ was chosen first because the overall channel average Nusselt number uses this characteristic temperature ratio. It can be seen in Figure 2.6 that $\overline{\Delta T}$ closely correlates the overall channel Nusselt number for all values of T^*_R. But, it is clear from Figure 3.1 that the hot wall average Nusselt number does not correlate with $\overline{\Delta T}$.

The hot wall average Nusselt number is then defined with ΔT_{walls} as the characteristic temperature difference as:

$$\overline{Nu}_{H,\Delta T_{walls}} = \frac{q_H b}{L k_f \Delta T_{walls}} \tag{3.2}$$

where

$$\Delta T_{walls} = T_H - T_C \tag{3.3}$$

The hot wall average Nusselt number using ΔT_{walls} as the characteristic temperature difference is graphed versus the modified Rayleigh number in Figure 3.2. As the modified Rayleigh number approaches zero, the strength of the convective flow diminishes in the channel and the heat transfer occurs by pure conduction from the hot

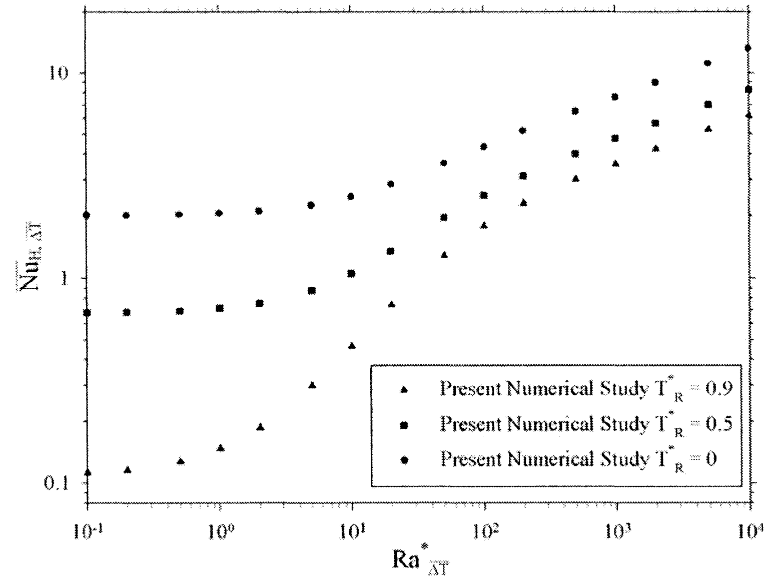

Figure 3.1: Variation of hot wall average Nusselt number based on $\overline{\Delta T}$ with respect to modified Rayleigh number.

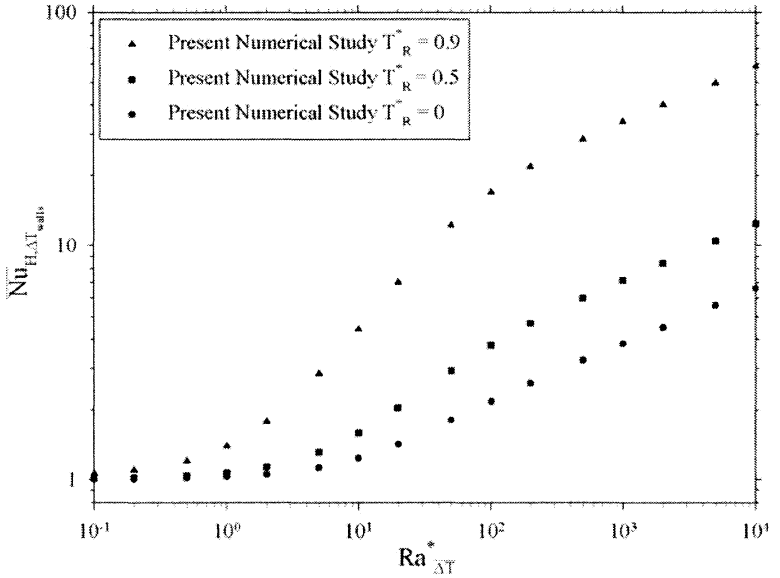

Figure 3.2: Variation of hot wall average Nusselt number based on ΔT_{walls} with respect to modified Rayleigh number.

wall to the cold wall. For this reason, the hot wall average Nusselt number based on ΔT_{walls} approaches 1 for all values of T_R^* at low modified Rayleigh number. Figure 3.2 shows that at high modified Rayleigh number, each curve approaches a different asymptotic limit. The characteristic temperature difference ΔT_{walls} is only useful for correlating the hot wall average Nusselt number at low Raleigh number. A sample temperature contour plot at low modified Rayleigh number (near the pure conduction limit) is shown in Figure 3.3(a). This figure shows that pure conduction exists between the two channel walls at low modified Rayleigh number. It also shows the end loses out the bottom of the channel. So, at low modified Rayleigh number, it is clear that ΔT_{walls} is the best characteristic temperature difference to use for correlating the hot wall average Nusselt number.

Figure 3.4 shows the variation of the hot wall average Nusselt number with modified Rayleigh number, with ΔT_{max} as the characteristic temperature difference in the hot wall average Nusselt number. It is defined as:

$$\overline{Nu}_{H,\Delta T_{max}} = \frac{q_H b}{L k_f \Delta T_{max}} \tag{3.4}$$

At high modified Rayleigh number, the convective flow in the channel is strong, so the hot wall average Nusselt number approaches the isolated plate limit. In this regime, two boundary layers form on the channel walls and the fluid outside the boundary layer is at ambient temperature. A sample temperature contour plot at high modified Rayleigh number (near the isolated plate limit) is shown in Figure 3.3(b). Two separate boundary layers are shown between the two channel walls. At high modified Rayleigh number, since the temperature difference that drives the heat transfer is ΔT_{max}, all curves for different values of T_R^* closely approach the isolated flat plate asymptote. So at high modified Rayleigh number, ΔT_{max} is the best temperature difference for correlating the hot wall average Nusselt number. In contrast, at low modified Rayleigh numbers the curves for different values of T_R^* approach distinctly different conduction asymptotes. This shows that a correlation technique could be applied to the data using ΔT_{max} as the characteristic temperature difference.

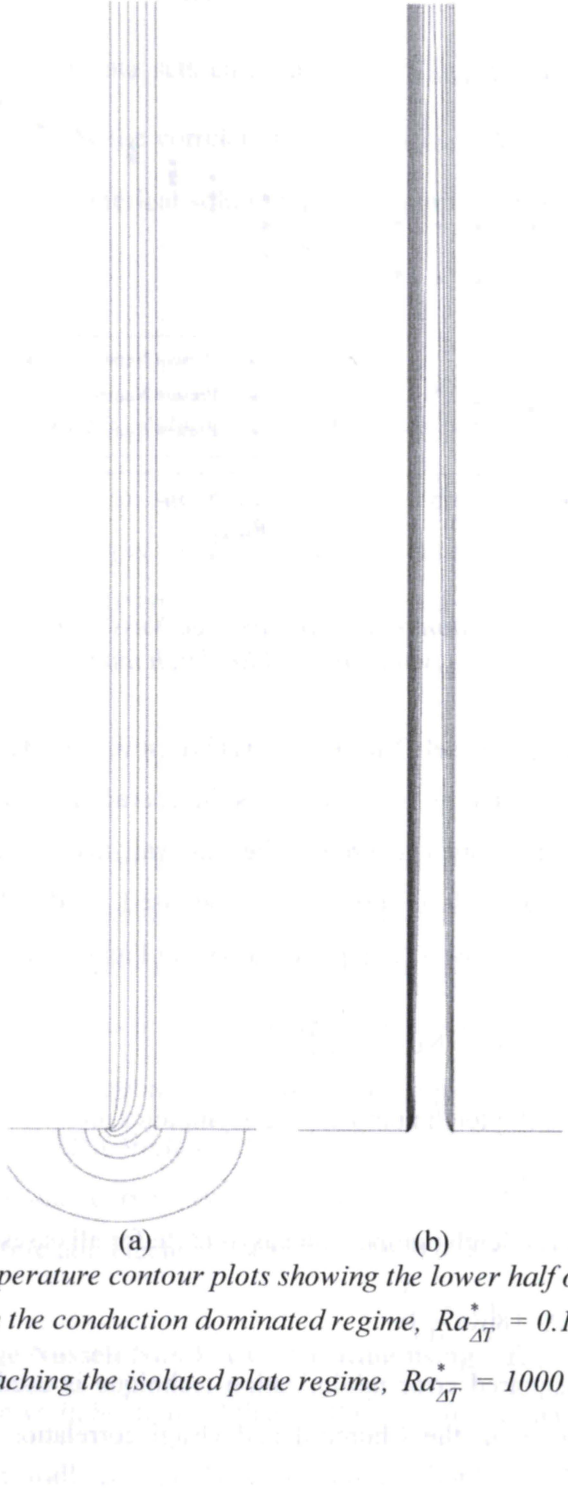

(a) (b)

Figure 3.3: Temperature contour plots showing the lower half of the channel for $T_R^* = 0.5$*: (a) in the conduction dominated regime,* $Ra^*_{\overline{\Delta T}} = 0.1$ *and* $L/b = 100$ *and (b) approaching the isolated plate regime,* $Ra^*_{\overline{\Delta T}} = 1000$ *and* $L/b = 50$*.*

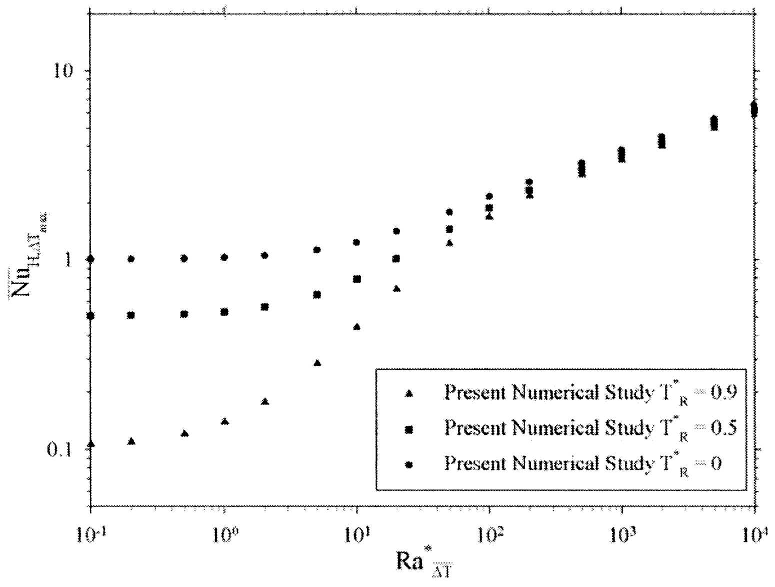

Figure 3.4: Variation of hot wall average Nusselt number based on ΔT_{max} with modified Rayleigh number.

3.2.1 Hot Wall Average Nusselt Number Correlation using ΔT_{max}

Figure 3.4 shows that by using ΔT_{max} as the characteristic temperature difference, a correlation can be developed to predict the hot wall average Nusselt number. The method of Churchill and Usagi (1972) will be used to develop a correlation that incorporates the upper and lower asymptotes shown in Figure 3.4:

$$\overline{Nu} = \left(\left(\overline{Nu}_{Ra^*_{\Delta T}\to 0}\right)^n + \left(\overline{Nu}_{Ra^*_{\Delta T}\to \infty}\right)^n\right)^{\frac{1}{n}} \tag{3.5}$$

where at low modified Rayleigh numbers, the asymptotes are:

$$\overline{Nu}_{Ra^*_{\Delta T}\to 0} = 1 - T^*_R \tag{3.6}$$

and at high modified Rayleigh numbers, the asymptote for all cases approaches:

$$\overline{Nu}_{Ra^*_{\Delta T}\to \infty} = 0.618\left(Ra^*_{\Delta T}\right)^{\frac{1}{4}} \tag{3.7}$$

A least sum-squared error minimization technique is used on the correlation to calculate the constant n in the Churchill and Usagi correlation technique. The sum squared error is:

$$E = \sum_{i=1}^{K} \left(\left(\frac{ \left(\overline{Nu}_{H,\Delta T_{max}} \right)_{Cor} - \left(\overline{Nu}_{H,\Delta T_{max}} \right)_{Data} }{ \left(\overline{Nu}_{H,\Delta T_{max}} \right)_{Data} } \right)^{2} \right)_{i} \tag{3.8}$$

where K is the number of data sets calculated, $\left(\overline{Nu}_{H,\Delta T_{max}} \right)_{Cor}$ is the hot wall average Nusselt number predicted by the correlation, and $\left(\overline{Nu}_{H,\Delta T_{max}} \right)_{Data}$ is the hot wall average Nusselt number from the numerical solution. The minimization is achieved by adjusting the constant n until:

$$\frac{\partial E}{\partial n} \cong 0 \tag{3.9}$$

where $\frac{\partial E}{\partial n} \cong \frac{(\delta E)_n + (\delta E)_{n+\delta n}}{\delta n}$, where δE_n is the sum-squared error calculated using constant n, and $\delta E_{n+\delta n}$ is the sum-squared error calculated using constant n + δn, and δn = 0.001. Once the minimization is completed on the data using ΔT_{max} as the characteristic temperature difference, the constant n was determined to be 3.368. Therefore, the correlation becomes:

$$\overline{Nu}_{H,\Delta T_{max}} = \left(\left(1 - T_R^*\right)^{3.368} + \left(0.618 \left(Ra_{\overline{\Delta T}}^* \right)^{\frac{1}{4}} \right)^{3.368} \right)^{\frac{1}{3.368}} \tag{3.10}$$

This correlation is presented in Figure 3.5 along with the numerical hot wall average Nusselt number data as comparison. Figure 3.5 shows that this correlation does not fit the data well for the modified Rayleigh number range of interest in this study. For the case of T_R^* = 0, the correlation fits the data very well, but because the cases of T_R^* = 0.5 and T_R^* = 0.9 have an inflection point between the upper and lower asymptotes, the Churchill and Usagi (1972) correlation technique is unable to fit the data through the inflection point on the data curve. This shows that some further analysis of the data is required before this correlation technique can be applied to the data.

3.3 Hot Wall Average Nusselt Number Correlation using ΔT_{eff}

It has been shown in Section 3.2 that as $Ra_{\overline{\Delta T}}^* \rightarrow 0$, the characteristic temperature difference in the hot wall average Nusselt number should be ΔT_{walls}, while at high modified Rayleigh number the characteristic temperature difference should be ΔT_{max}. So to produce a characteristic temperature difference that correlates the hot wall average Nusselt number over the complete range of modified Rayleigh numbers in this study, it is proposed to use a "blended" effective temperature difference as follows:

$$\Delta T_{eff} = A(\Delta T_{walls}) + (1 - A)(\Delta T_{max}) \tag{3.11}$$

where A is a weighting function that varies from A = 1 at $Ra^*_{\overline{\Delta T}} \rightarrow 0$, to A = 0 as $Ra^*_{\overline{\Delta T}} \rightarrow \infty$. Several different weighting functions with the above characteristic were tested. The weighting function that was found to give the best fit to the data is shown in Figure 3.6 and is given by:

$$A = \frac{C}{\left(Ra^*_{\overline{\Delta T}}\left(\frac{\Delta T_{max}}{\overline{\Delta T}}\right)\right)^m + C} = \frac{38.583}{\left(Ra^*_{\overline{\Delta T}}\left(\frac{\Delta T_{max}}{\overline{\Delta T}}\right)\right)^{1.128} + 38.583} \tag{3.12}$$

The constant C and exponent m in equation (3.12) were both adjusted to minimize the sum-squared error between the empirical correlations and the numerical data. The modified Rayleigh number is used as the determining variable in the weighting function, but it uses a conversion factor of $\frac{\Delta T_{max}}{\overline{\Delta T}}$ to become a general equation for all values of T^*_R. It should be noted that:

$$\frac{\Delta T_{max}}{\overline{\Delta T}} = \frac{2}{1 + T^*_R} \tag{3.13}$$

Figure 3.7 shows the hot wall average Nusselt number variation with modified Rayleigh number, with the new proposed ΔT_{eff} as the characteristic temperature difference in the Nusselt number. It is defined as:

$$\overline{Nu}_{H,\Delta T_{eff}} = \frac{q_H \cdot b}{L \cdot k_f \cdot \Delta T_{eff}} \tag{3.14}$$

It can be seen that the data for all values of T^*_R collapse onto almost one curve. The scatter in the data is approximately ±10%. It should be noted that with this proposed blended temperature difference, there are well-defined asymptotes at high and low modified Rayleigh number. Given the clearly defined asymptotes, the method of

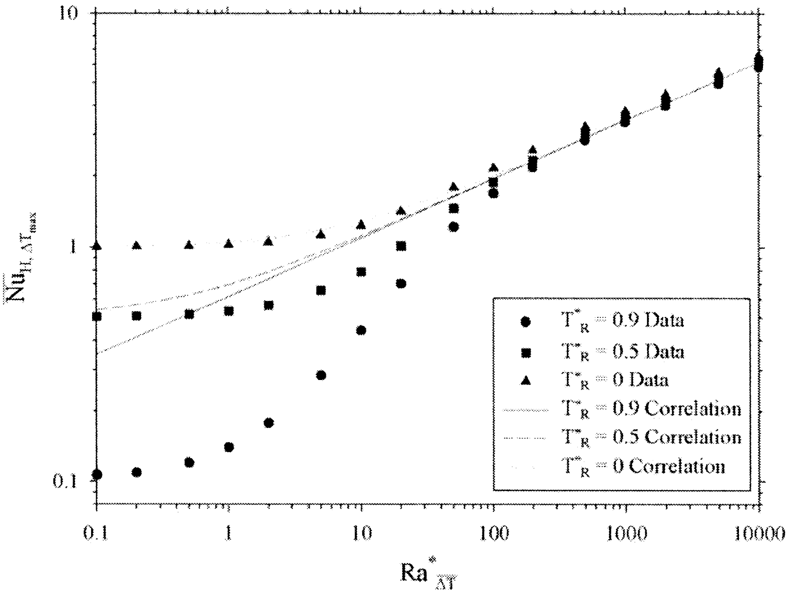

Figure 3.5: Hot wall average Nusselt number correlation and variation of hot wall average Nusselt number based on ΔT_{max} with modified Rayleigh number.

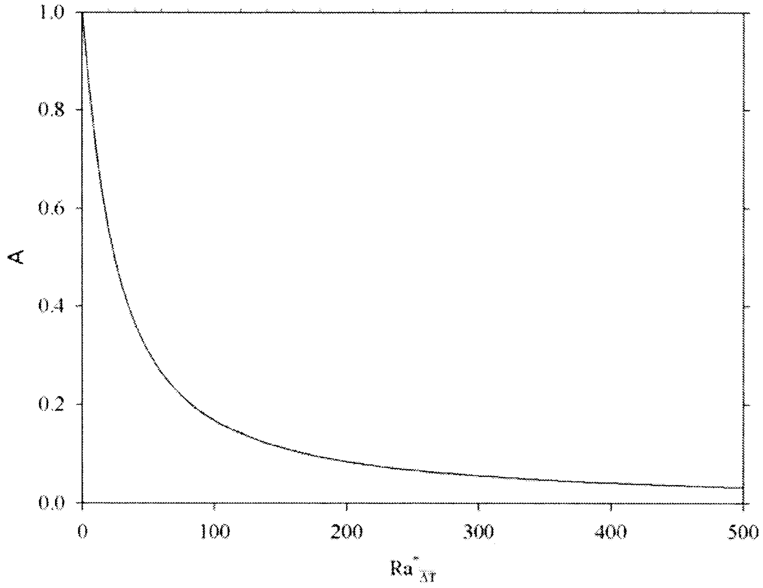

Figure 3.6: Variation of weighting function A with respect to modified Rayleigh number

Churchill and Usagi (1972) is easily applied to develop an empirical correlation over the full range of modified Rayleigh numbers. In this method, the upper and lower asymptotic limits for Nusselt number are combined as follows:

$$\overline{Nu} = \left(\left(\overline{Nu}_{Ra^*_{\overline{\Delta T}} \to 0} \right)^n + \left(\overline{Nu}_{Ra^*_{\overline{\Delta T}} \to \infty} \right)^n \right)^{\frac{1}{n}} \tag{3.5}$$

where the lower asymptote approaches 1, as discussed previously:

$$\overline{Nu}_{Ra^*_{\overline{\Delta T}} \to 0} = 1 \tag{3.15}$$

and the upper asymptote approaches the isolated flat plate limit:

$$\overline{Nu}_{Ra^*_{\overline{\Delta T}} \to \infty} = 0.618 \left(Ra^*_{\overline{\Delta T}} \right)^{\frac{1}{4}} \tag{3.7}$$

The upper asymptote, $Ra^*_{\overline{\Delta T}} \to \infty$, is taken from Raithby and Hollands (1998) using the upper asymptote of the correlation for the overall channel average Nusselt number. After a least squares minimization of the percentage error between the numerical data and the empirical correlations predicted results, the hot wall average Nusselt number correlation is:

$$\overline{Nu}_{H,\Delta T_{eff}} = \left[1 + \left(0.618 \left(Ra^*_{\overline{\Delta T}} \right)^{\frac{1}{4}} \right)^{3.011} \right]^{\frac{1}{3.011}} \tag{3.16}$$

This correlation is shown in Figure 3.7 along with the numerical data. This correlation fits the data with a standard deviation of ±2% and a maximum error of ±11%. The dashed lines show ±10% error of the correlation given in equation (3.16). The data fits well within this ±10% boundary.

The cold wall average Nusselt number can now be calculated using an energy balance for the overall channel as:

$$\overline{Nu}_{C,\overline{\Delta T}} = 2\overline{Nu}_{O,\overline{\Delta T}} - \overline{Nu}_{H,\Delta T_{eff}} \left(\frac{\Delta T_{eff}}{\overline{\Delta T}} \right) \tag{3.17}$$

In applying equation (3.17), the hot wall average Nusselt number is calculated from equation (3.16) and the overall channel average Nusselt number is calculated from the empirical correlation from Raithby and Hollands (1998) and Aung (1972) which is:

$$\overline{Nu}_{fd} = \frac{4T_R^{*2} + 7T_R^* + 4}{90\left(1 - T_R^*\right)^2} Ra^*_{\overline{\Delta T}} \tag{1.11}$$

$$\overline{Nu}_{O,\overline{\Delta T}} = \left[\left(\overline{Nu}_{fd}\right)^{-1.9} + \left(0.618\left(Ra^*_{\overline{\Delta T}}\right)^{0.25}\right)^{-1.9}\right]^{\frac{1}{-1.9}} \tag{1.16}$$

Figure 3.8 shows the variation of the cold wall average Nusselt number with modified Rayleigh number for different values of T_R^*. This is defined as:

$$\overline{Nu}_{C,\overline{\Delta T}} = \frac{q_C \cdot b}{L \cdot k_f \cdot \overline{\Delta T}} \tag{3.18}$$

where q_C is the convective heat transfer rate of the cold wall. It can be seen that equation (3.17) fits the numerical data closely for all values of T_R^*. Even the cases of $T_R^* = 0.5$ and 0.9, where $\overline{Nu}_{C,\overline{\Delta T}}$ changes sign with the modified Rayleigh number, are well predicted.

3.3.1 Least Sum-Squared Minimization Technique

It should be mentioned that the constant C and exponent m in equation (3.12) and the exponent n in equation (3.16) were adjusted to simultaneously minimize the error in both the cold and hot wall average Nusselt number correlations. The sum squared error is defined as:

$$E_{Hot} = \sum_{i=1}^{K}\left(\left(\frac{\left(\overline{Nu}_{H,\Delta T_{eff}}\right)_{Cor} - \left(\overline{Nu}_{H,\Delta T_{eff}}\right)_{Data}}{\left(\overline{Nu}_{H,\Delta T_{eff}}\right)_{Data}}\right)^2\right)_i \tag{3.19a}$$

$$E_{Cold} = \sum_{i=1}^{K}\left(\left(\frac{\left(\overline{Nu}_{C,\overline{\Delta T}}\right)_{Cor} - \left(\overline{Nu}_{C,\overline{\Delta T}}\right)_{Data}}{\left(\overline{Nu}_{C,\overline{\Delta T}}\right)_{Data}}\right)^2\right)_i \tag{3.19b}$$

$$E = E_{Hot} + E_{Cold} \tag{3.19c}$$

where K is the number of data sets, $\left(\overline{Nu}_{H,\Delta T_{eff}}\right)_{Cor}$ is the hot wall average Nusselt number predicted by the correlation, $\left(\overline{Nu}_{H,\Delta T_{eff}}\right)_{Data}$ is the hot wall average Nusselt number from

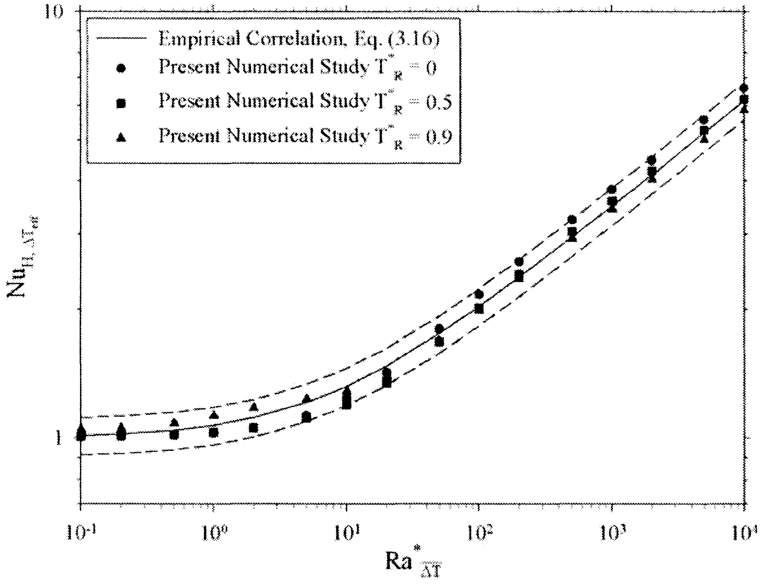

Figure 3.7: Hot wall average Nusselt number correlation and variation of hot wall average Nusselt number based on ΔT_{eff} with modified Rayleigh number.

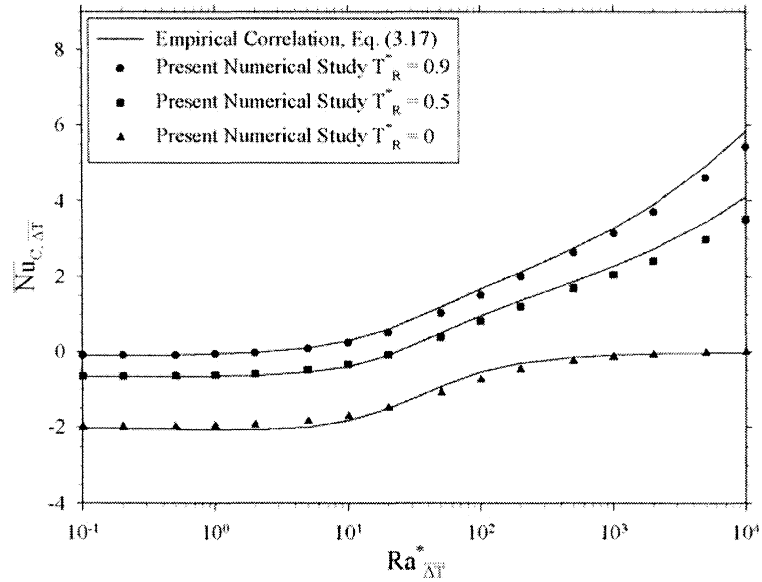

Figure 3.8: Cold wall average Nusselt number correlation and variation of cold wall average Nusselt number based on $\overline{\Delta T}$ with modified Rayleigh number.

the numerical solution, $\left(\overline{\mathrm{Nu}}_{C.\overline{\Delta T}}\right)_{Cor}$ is the cold wall average Nusselt number predicted by the correlation, and $\left(\overline{\mathrm{Nu}}_{C.\overline{\Delta T}}\right)_{Data}$ is the cold wall average Nusselt number from the numerical solution. The cold wall average Nusselt number approaches or crosses zero in all three cases of T_R^*. This will cause E_{Cold} to approach ∞, which will make the minimization procedure forcing the cold wall average Nusselt number correlation to match more closely than the hot wall average Nusselt number correlation. Because of this, the denominator in equation (2.23b), $\left(\overline{\mathrm{Nu}}_{C.\overline{\Delta T}}\right)_{Data}$ is fixed to $\overline{\mathrm{Nu}}_{C,\overline{\Delta T}}$ solved at $Ra_{\overline{\Delta T}}^* = 0.1$ and $T_R^* = 0$ for all data sets used in calculating E_{Cold}. The minimization is achieved by adjusting the constants C, m and n until:

$$\frac{\partial E}{\partial C} \cong \frac{\partial E}{\partial m} \cong \frac{\partial E}{\partial n} \cong 0 \tag{3.20}$$

with $\frac{\partial E}{\partial C} \cong \frac{(\delta E)_C + (\delta E)_{C+\delta C}}{\delta C}$, where δE_C is the sum-squared error calculated using constant C, and $\delta E_{C+\delta C}$ is the sum-squared error calculated using constant $C + \delta C$, and $\delta C = 0.001$. Similarly, $\frac{\partial E}{\partial m} \cong \frac{(\delta E)_m + (\delta E)_{m+\delta m}}{\delta m}$, where δE_m is the sum-squared error calculated using constant m, and $\delta E_{m+\delta m}$ is the sum-squared error calculated using constant $m + \delta m$, $\delta m = 0.001$, and $\frac{\partial E}{\partial n} \cong \frac{(\delta E)_n + (\delta E)_{n+\delta n}}{\delta n}$, where δE_n is the sum-squared error calculated using constant n, $\delta E_{n+\delta n}$ is the sum-squared error calculated using constant $n + \delta n$, and $\delta n = 0.001$. Constants C, m and n are adjusted until equation (3.20) is satisfied, giving $C = 38.583$, $m = 1.128$, and $n = 3.011$. These constants are then used in their respective correlations, which are used for calculating the channel convective heat transfer in the complex fenestration problem discussed in the next chapter.

PROPERTY OF
RYERSON UNIVERSITY LIBRARY

Chapter 4

Simplified Model of a Complex Fenestration System

4.1 Introduction

A complex fenestration system is composed of single or multiple window glazings with some type of shading device present. This can include many types of blind (e.g., Venetian or roller blind) and many different locations of the blind (e.g., inside, outside or in between the window glazings). Huang et al. (2006) studied the system where a Venetian blind is located in between two window glazings. A simplified model was produced that could predict the heat transfer of the system accurately when compared with experimental results. A similar approach is presented here, but in this case a Venetian blind is hung on the indoor side of the window glazing. The geometry of the window and Venetian blind is shown in Figure 4.1(a). For the system studied here, it is modeled as a combination of two classical heat transfer geometries. The first geometry is free convection in an asymmetrically heated vertical channel, where the correlations of the previous chapter are utilized. The second geometry is free convection from a vertical flat plate, using existing correlations from the literature. The geometry of the vertical channel and flat plate approximation is shown in Figure 4.1(b). With this model, the Venetian blind is approximated as an impermeable vertical surface.

If we look at the case where the Venetian blind slats are at an angle of 90°, there is no flow through the blind slats as they are completely closed. It can be assumed that the top surfaces of the blind slats interact only with the window surface similar to a channel and the bottom surface of the blind slats interact only with the ambient similar to a flat plate. Figure 4.2 shows an experimental case conducted by Machin (1998) of a Venetian blind with a blind slat angle of 90°. In this figure, even though the blind slats are not heated, there is no flow between the blind slats showing that this simplified model approximation can be considered. As the blind slat angle decreases, the blind slats interact with the flow, as will be discussed in more detail in the next chapter (see Figure 5.2). This simplified model uses some adjustable constants to account for the interaction of the blind slats.

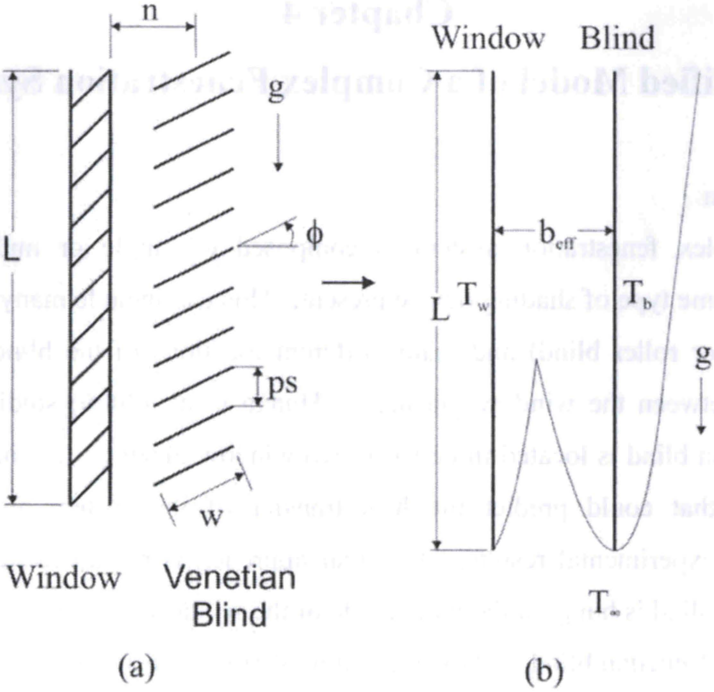
n
g
φ
L
ps
w
Window
Venetian Blind
Window
Blind
b_eff
L
T_w
T_b
g
T_∞
(a)
(b)

Figure 4.1: (a) Window and Venetian blind problem geometry; (b) Channel and flat plate approximation geometry.

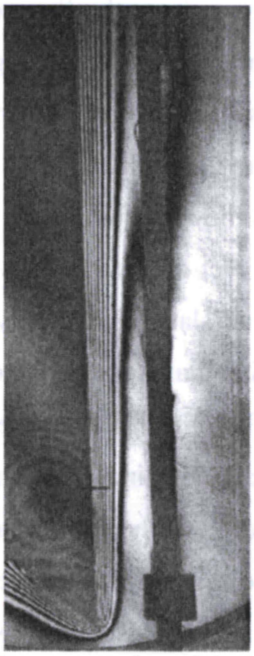

Figure 4.2: Infinite fringe interferograms from Machin (1998) with blind slats at 90°.

A detailed description of the simplified model and the various techniques used is presented here. A detailed calculation of a sample problem using this simplified model is provided in Appendix B. This model is used to predict various results to compare with experimental and numerical data (Machin 1998, Collins et al. 2002b, and Collins 2001).

4.1.1 Effective Channel Width

One of the adjustable parameters in this model is the effective channel width, b_{eff}. This is accomplished by using an adjustable constant, N, that changes the spacing between the tip of the blind slat to the window surface to increase the accuracy of the simplified model. This is a similar approach to the one used by Huang et al. (2006). Figure 4.3 shows the geometry of the blind-to-window spacing, n, and the effective channel width, b_{eff}. The effective channel width is defined as:

$$b_{eff} = n - \frac{w}{2}\cos(\phi) + t\sin(\phi) + N\frac{w}{2}\cos(\phi) \tag{4.1}$$

where t is the curvature spacing. The effective channel width is calculated with a straight

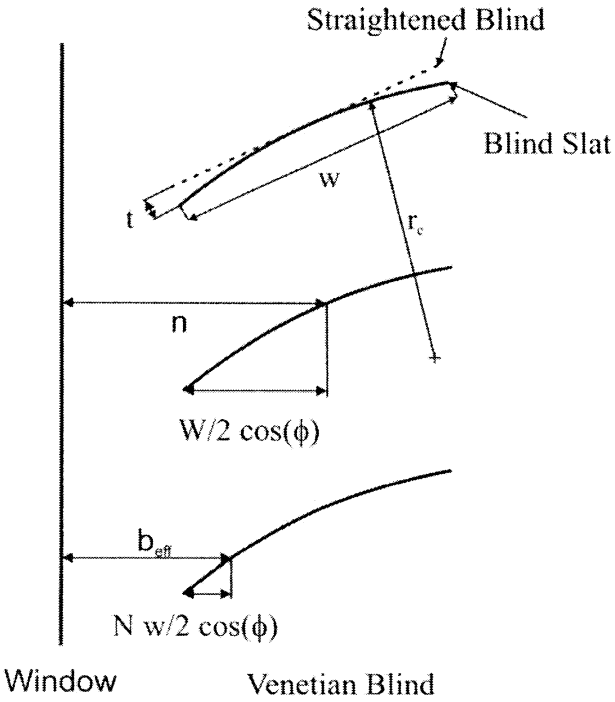

Figure 4.3: Geometry of blind-to-window spacing, n, and effective channel width, b_{eff}.

blind slat, but because there is a slight curve in the blind slat, this creates a slight error in the blind-to-window spacing. To overcome this error, the curvature spacing is calculated:

$$t = r_c\left(1-\cos\left(\frac{w}{2r_c}\right)\right) \tag{4.2}$$

where r_c is the radius of curvature of the blind slat. The effective channel width is calculated and then used as the channel width when calculating the modified Rayleigh number of the channel. The modified Rayleigh number then affects the average Nusselt number calculations (Eqs. (3.16), (3.17), (1.11), and (1.16)), which affects the heat transfer rates.

4.2 Blind Slat Energy Balance

In order to develop the simplified model, a method of balancing the heat transfer of the system is required. This is accomplished by developing an energy balance on a single blind slat as shown in Figure 4.4. This is an iterative process, which is explained in further detail in section 4.2.5. The energy balance on the blind slat is:

$$q_{solar} = F_1 q_{conv,ch} + F_2 q_{conv,fp} + q_{rad} \tag{4.3}$$

where q_{solar} is the solar heat absorbed by the blind slat, $q_{conv,ch}$ is the channel convective heat transfer rate, $q_{conv,fp}$ is the convective flat plate heat transfer rate, q_{rad} is the radiation heat transfer rate from the blind slat, and F_1 and F_2 are the two adjustable fractions of the channel and flat plate convective heat transfer rates. The solar heat absorbed by the blind slat is a known quantity in this problem, as determined by an appropriate solar optical model such as Kotey and Wright (2006). The other heat transfer rates are determined in the following sections.

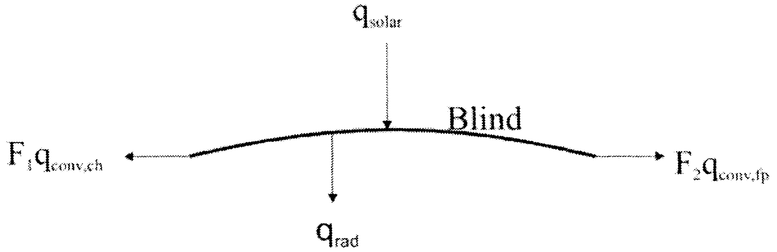

Figure 4.4: Energy balance of a single blind slat

4.2.1 Hottel's Crossed String Method

In order to calculate the view factors for the radiation model, $F_{i\text{-}k}$ and $F_{k\text{-}i}$, Hottel's crossed string method (Hottel 1967) is used. The basis of this method is that the view factor between two surfaces separated by some distance can be determined by the strings between the corners of the surfaces. The strings are represented by the dashed and dotted lines in Figure 4.5. The view factors are determined by:

$$F_{k-i} = \frac{\sum\left(\text{Crossed strings}\right) - \sum\left(\text{uncrossed strings}\right)}{2 \cdot \text{Length surface k}} \tag{4.4}$$

The crossed strings are the dashed lines in Figure 4.5 and the uncrossed strings are the dotted lines. For further clarification, two surfaces AB and CD, as shown in Figure 4.5(a), are used to calculate the view factor, $F_{AB\text{-}CD}$:

$$F_{AB-CD} = \frac{(AD + BC) - (AC + BD)}{2(AB)} \tag{4.5}$$

where AD, BC, AC, AB and BD are the distances between the points. For another two surfaces, AC and CB that join at point C as shown in Figure 4.5(b), a similar method can be used to calculate the view factor $F_{AC\text{-}CB}$:

$$F_{AC-CB} = \frac{(AC + CB) - (AB)}{2(AC)} \tag{4.6}$$

As Figure 4.5(c) shows, the corner can be moved apart to show the lengths of interest similar to Figure 4.5(a), except that the strings at point C have no length. This method was used to calculate all the required view factors for the four surface radiation model.

4.2.2 Four Surface Radiation Model and Radiative Heat Transfer

The first heat transfer rate to be determined is the radiation heat transfer rate, q_{rad}. This is determined by a simple four surface grey diffuse radiation model. It is assumed that only the center glass region is of interest and therefore it can be approximated that the Venetian blind and window system are of an infinite length in both upward and downward directions as shown in Figure 4.6(a). Since the Venetian blind and window are of infinite length, the view factor from the window to the Venetian blind is the same

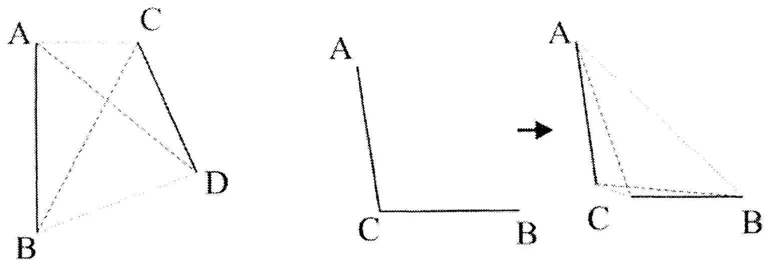

(a) (b) (c)

Figure 4.5: Hottel's crossed string method: (a) Two surfaces (strings showing); (b) Two surfaces with a common corner; (c) Two surfaces with a common corner (strings showing).

regardless of the spacing between the Venetian blind and the window. The Venetian blind can then be placed directly beside the window (shown in Figure 4.6(b)), creating an array of boxes because of this. If a single box is taken into account, as shown in Figure 4.6(c), a four surface model is left: (1) window surface, ε_w, T_w; (2) lower blind slat surface, ε_b, T_b; (3) ambient, $\varepsilon_\infty = 1$, T_∞; (4) upper blind slat surface, ε_b, T_b. A radiation analysis is performed on this single box to determine the radiation heat transfer rates of the window and blind slat.

An iterative method developed by Bevans and Dunkel (Wiebelt, 1966) for a multi-surface grey diffuse enclosure was used to calculate the radiation heat transfer. This method requires the calculation of two equations for each surface, the radiation heat transfer, $q_{rad,i}$, and the radiosity, j_i. The radiation heat transfer is calculated by the amount of energy emitted (radiosity) subtracted by the amount of irradiation as shown in equations (4.7a) and (4.7b):

$$q_{rad,i} = A_i j_i - G_i \tag{4.7a}$$

where A_i is the area of the surface, G_i is the irradiation, and i is the surface number.

$$q_{rad,i} = A_i j_i - \sum_{k=1}^{M} j_k A_k F_{k-i} \tag{4.7b}$$

where M is the number of surfaces (in this case 4). The radiosity of each surface is given by:

$$j_i = \varepsilon_i e_i + \rho_i \sum_{k=1}^{M} j_k F_{i-k} \tag{4.8}$$

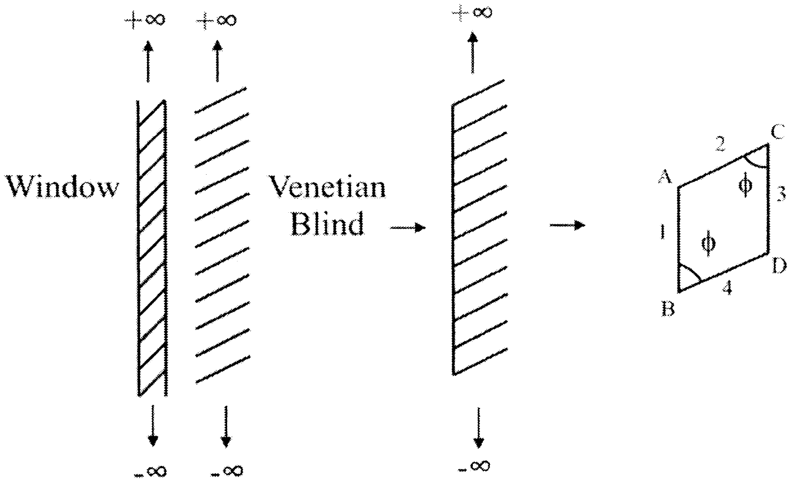

(a) (b) (c)

Figure 4.6: (a) Infinite length Venetian blind on inside surface of an infinite length window; (b) Infinite array of 4 surface boxes; (c) Four surface radiation model.

where ε_i is the emissivity of the surface, ρ_i is the reflectivity of the surface ($\rho = 1 - \varepsilon$), and e_i is the blackbody emissive power of each surface, which is expressed as:

$$e_i = \sigma T_i^4 \qquad (4.9)$$

where σ is the Stefan-Boltzman constant and T_i is the temperature of the surface. This model calculates radiation of all four surfaces in Figure 4.6(c). All surfaces of the radiation model are treated as opaque surfaces, so $\rho = 1 - \varepsilon$. It should be noted that surfaces 2 and 4 combine to give the radiative heat transfer rate of the blind slat, $q_{rad,b}$ and surface 1 is the radiative heat transfer rate of the window, $q_{rad,w}$, which are the two radiative heat transfer rates of interest.

An eight surface radiation model was also solved by taking the four surface radiation model and splitting each surface into two surfaces. The difference in results between the 8 surface and 4 surface radiation model is less than 2%, so the four surface radiation model was used for simplicity.

4.2.3 Channel Convective Heat Transfer

The channel convective heat transfer rate, $q_{conv,ch}$, is given by the following Nusselt number correlations that were developed in the previous chapter.

$$\overline{Nu}_{H,\overline{\Delta T}} = \left(1+\left(0.618\left(Ra^*_{\overline{\Delta T}}\right)^{0.25}\right)^{3.011}\right)^{\frac{1}{3.011}} \cdot \left(\frac{\Delta T_{eff}}{\overline{\Delta T}}\right) \tag{3.16}$$

$$\overline{Nu}_{C,\overline{\Delta T}} = 2\overline{Nu}_{O,\overline{\Delta T}} - \overline{Nu}_{H,\Delta T_{eff}} \tag{3.17}$$

where $Ra^*_{\overline{\Delta T}}$, $\overline{\Delta T}$ and ΔT_{eff} are previously defined. The hot wall average Nusselt number is converted to be based on $\overline{\Delta T}$ for simplification in calculating the heat transfer coefficient (see Appendix B). The overall average channel Nusselt number is given by Aung (1972) and Raithby and Hollands (1998):

$$\overline{Nu}_{fd} = \frac{4\cdot T_R^{*2} + 7\cdot T_R^* + 4}{90\cdot\left(1+T_R^*\right)^2} Ra^*_{\overline{\Delta T}} \tag{1.11}$$

$$\overline{Nu}_{O,\overline{\Delta T}} = \left(\left(\overline{Nu}_{fd}\right)^{-1.9} + \left(0.618\cdot Ra^{*\frac{1}{4}}_{\overline{\Delta T}}\right)^{-1.9}\right)^{\frac{1}{-1.9}} \tag{1.16}$$

The channel convective heat transfer coefficient, $h_{b,ch}$ is defined as:

$$h_{b,ch} = \frac{\overline{Nu}\cdot k_f}{b_{eff}} \tag{4.10}$$

where k_f is the conductivity of the fluid (air in this case), b_{eff} is the effective channel width, and $\overline{Nu}$ is the average Nusselt number. In any window and blind problem, there are two cases to consider: (i) the case of the blind being hotter than the window or (ii) the case of the blind being colder than the window surface. The average Nusselt number in equation (4.10) is dependant on which of these two cases is present in the problem. If the blind is hotter than the window surface (i), then the average Nusselt number is $\overline{Nu}_{H,\overline{\Delta T}}$ and equation (3.16) is utilized. If the window surface is hotter than the blind (ii), then $\overline{Nu}_{C,\overline{\Delta T}}$ in equation (3.17) is utilized as the average Nusselt number. The convection coefficient for the window is then defined as:

$$h_{w,ch} = \frac{\overline{Nu}\cdot k_f}{b_{eff}} \tag{4.11}$$

where $\overline{Nu}$ is dependant on the two cases mentioned previously. For case (i), $\overline{Nu}$ is

$\overline{\mathrm{Nu}}_{C,\overline{\Delta T}}$, and for case (ii), $\overline{\mathrm{Nu}}$ is $\overline{\mathrm{Nu}}_{H,\overline{\Delta T}}$, which are the opposite of the blind's average Nusselt numbers in each case. The channel convective heat transfer rate is defined as:

$$q_{conv,ch} = h_{b,ch} \cdot A_b \cdot \left(\overline{\Delta T}\right) \tag{4.12}$$

where A_b is the surface area of one side the blind slat, which is taken as a unit length by the pitch of the blind slats, ps.

4.2.4 Flat Plate Convective Heat Transfer

The flat plate convection coefficient, $h_{b,fp}$, is from the average Nusselt number of a flat plate developed by Churchill and Chu (1975):

$$\overline{\mathrm{Nu}}_{fp} = 0.68 + \frac{0.67 \cdot \mathrm{Ra}_L^{\;0.25}}{\left(1+\left(\frac{0.492}{\mathrm{Pr}}\right)^{\frac{9}{16}}\right)^{\frac{4}{9}}} = \frac{h_{b,fp} \cdot L}{k_f} \tag{4.13}$$

where

$$\mathrm{Ra}_L = \mathrm{Gr}_L\ \mathrm{Pr} \tag{4.14}$$

and

$$\mathrm{Gr}_L = \frac{g\beta(T_b - T_\infty)L^3}{\nu_f^{\;2}} \tag{4.15}$$

The heat transfer rate is defined as:

$$q_{conv,fp} = h_{b,fp} \cdot A_b \cdot \left(T_b - T_\infty\right) \tag{4.16}$$

4.2.5 Correction Functions for Convective Flat Plate and Channel Heat Transfer

The correction functions F_1 and F_2 are used to adjust the fraction of flat plate and channel convective heat transfer of the blind slat in the energy balance. The model is set with a blind slat angle of 90° (closed Venetian blind) and compared with the experimental results of Machin (1998) at the same angle. Both correction functions are set to 1, so that half of the blind slat surface area is channel convective heat transfer and the other half of the blind slat surface area is flat plate convective heat transfer. The comparisons are shown in Table 4.1 and they show agreement between the model and the experimental

Table 4.1: Comparison of the experimental measurements (Machin et. al. 1998) with the current model for $\varepsilon_w = 0.81$, $\varepsilon_b = 0.81$, $q''_{solar} = 0\ W/m^2$, $T_w = 316.5\ K$, $T_\infty = 297\ K$, and $L = 379.6\ mm$.

SLAT ANGLE	BLIND-TO-WINDOW SPACING	MACHIN ET AL. (1998)		CURRENT MODEL		ERROR		MACHIN ET AL. (1998)	CURRENT MODEL	ERROR
ϕ	n (mm)	$q''_{conv,w}$ (W/m^2)	$q''_{rad,w}$ (W/m^2)	$q''_{conv,w}$ (W/m^2)	$q''_{rad,w}$ (W/m^2)	CONV (%)	RAD (%)	q''_{room} (W/m^2)	q''_{room} (W/m^2)	ROOM (%)
90°	13.0	71.57	78.32	74.32	63.90	-3.85	18.41	149.89	138.22	-7.78
90°	14.5	73.91	80.12	74.36	62.94	-0.61	21.44	154.03	137.30	-10.86
90°	17.0	70.98	83.16	74.15	61.79	-4.47	25.69	154.14	135.93	-11.80

results. It should be noted that in this experimental case, the radiation heat transfer was determined by the same four surface radiation model explained in section 4.2.2 by using the average temperature of the blind slats recorded by the experiment. With the limit of the correction functions being 1 when the blind slat angle is 90°, two equations are set up to define the functions:

$$F_1 = C_1 \cdot (1 + \cos(2 \cdot \phi)) + 1 \tag{4.17}$$

$$F_2 = C_2 \cdot (1 + \cos(2 \cdot \phi)) + 1 \tag{4.18}$$

where C_1 and C_2 are adjustable constants. These constants are adjusted using a least sum squares minimization procedure with a wide range of data sets mentioned in more detail in the next chapter.

4.2.6 Iteration Process of the Energy Balance

The energy balance requires an iterative process in order to obtain a converged solution. The iteration requires an initial guess of the Venetian blind temperature, T_b. This Venetian blind temperature is used for calculating the heat transfer rates from sections 4.2.2 through 4.2.4. Once the heat transfers are determined, the energy balance is set up to solve for an updated Venetian blind temperature. The process is then repeated with the updated Venetian blind temperature until a converged solution (i.e. the updated and the old Venetian blind temperatures are the same value) is obtained. A flow diagram of this process is shown in Figure 4.7. It should be noted that the flow chart is for solving a given case with the constants (C_1, C_2, and N) are given. (It does not include the least-squares minimization procedure). The converged solution is then used for comparison to

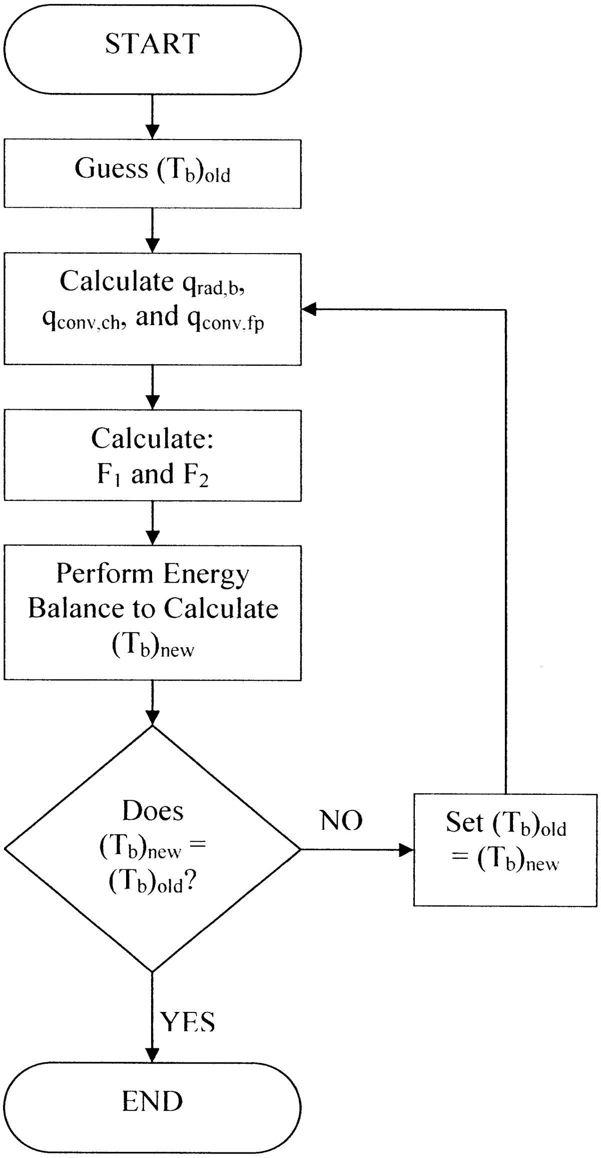
START
Guess $(T_b)_{old}$
Calculate $q_{rad,b}$, $q_{conv,ch}$, and $q_{conv,fp}$
Calculate: F_1 and F_2
Perform Energy Balance to Calculate $(T_b)_{new}$
Does $(T_b)_{new} = (T_b)_{old}$?
NO
Set $(T_b)_{old} = (T_b)_{new}$
YES
END

Figure 4.7: Flowchart showing the calculation procedure of the simplified model for a specific case with given constants C_1, C_2, and N.

existing results. Refer to Appendix B for a single iteration calculation of updating T_b. The computer code of the simplified model is presented in Appendix C. This code was developed using Matlab (2004).

4.3 Convective and Radiative Heat Transfer of the Window

The energy balance of the blind slat uses the heat transfers of the blind slat, but existing experimental and numerical results only report the convective and radiative heat fluxes of the window surface. So for comparison, the convective and radiative heat fluxes of the window surface are calculated:

$$q''_{conv,w} = h_{w,ch}\overline{\Delta T} \tag{4.19}$$

$$q''_{rad,w} = \frac{q_{rad,w}B}{L} \tag{4.20}$$

where B is the number of blind slats in the system. These equations produce the predicted results that are compared against the experimental work of Machin (1998) and Collins et al. (2002b) and the numerical work of Collins (2001).

Chapter 5

Comparison of the Simplified Model with Experimental and Numerical Results

5.1 Introduction

The comparisons of the experimental and numerical data (Machin et al. 1998, Collins et al. 2002b, and Collins 2001) with the predicted results of the simplified model are presented in this chapter. All the predicted results were calculated from the simplified model developed in the previous chapter. There are three different comparisons made: (i) the comparison of the convective and radiative heat fluxes with the experimental data only, (ii) the comparison of the convective and radiative heat fluxes with the numerical data only, and (iii) the comparison of the room heat flux with both the experimental and numerical data. A sampling of some significant results are presented and discussed in this chapter, but further results are presented in Appendix C. While looking at the comparisons in detail, some interesting patterns were present in the numerical work (Collins, 2001) that motivated an interferometric experiment to validate these patterns.

5.1.1 Least Sum-Squares Minimization

The constants (C_1, C_2, and N) were determined by a least sum-squares minimization procedure. There were two sum-squared error components that were calculated: the convection sum-squared error, E_{conv}, and the radiation sum-squared error, E_{rad}, which were both determined by comparing the experimental results to the predicted results.

$$E_{conv} = \sum_{i=1}^{K}\left(\left(\frac{\left(q''_{conv,w}\right)_{model} - \left(q''_{conv,w}\right)_{exp/num}}{\left(q''_{conv,w}\right)_{exp/num}}\right)^2\right)_i \tag{5.1a}$$

$$E_{rad} = \sum_{i=1}^{K}\left(\left(\frac{\left(q''_{rad,w}\right)_{model} - \left(q''_{rad,w}\right)_{exp/num}}{\left(q''_{rad,w}\right)_{exp/num}}\right)^2\right)_i \tag{5.1b}$$

$$E = E_{conv} + E_{rad} \tag{5.1c}$$

where K is the number of data sets used. The minimization is achieved by setting:

$$\frac{\partial E}{\partial C_1} \cong \frac{\partial E}{\partial C_2} \cong \frac{\partial E}{\partial N} \cong 0 \tag{5.2}$$

where $\frac{\partial E}{\partial C_1} \cong \frac{(E)_{C_1} - (E)_{C_1+\delta C_1}}{\delta C_1}$, $(E)_{C_1}$ is the sum-squared error calculated using constant C_1, and $(E)_{C_1+\delta C_1}$ is the sum-squared error calculated using constant $C_1 + \delta C_1$. Similarly, $\frac{\partial E}{\partial C_2} \cong \frac{(E)_{C_2} - (E)_{C_2+\delta C_2}}{\delta C_2}$, $\frac{\partial E}{\partial N} \cong \frac{(E)_N - (E)_{N+\delta N}}{\delta N}$, $(E)_{C_2}$ is the sum-squared error calculated using constant C_2, $(E)_{C_2+\delta C_2}$ is the sum-squared error calculated using constant $C_2 + \delta C_2$. $(E)_N$ is the sum-squared error calculated using constant N, and $(E)_{N+\delta N}$ is the sum-squared error calculated using constant $N + \delta N$. Note that $\delta C_1 = \delta C_2 = \delta N = 0.01$ in this minimization scheme. The constants are adjusted until equation (5.2) is satisfied, which means the sum-squared error between the experimental results and the simplified models predicted results is minimized. This scheme is used on multiple data sets to determine the constants that best fit the data used.

5.1.2 Percent Error

The percent error is determined by comparing the experimental and numerical results with the simplified models results. There are two percent errors associated with the presentation of the results, the convection percent error and the radiation percent error.

$$(\text{error})_{conv} = \frac{\left(q''_{conv,w}\right)_{model} - \left(q''_{conv,w}\right)_{exp/num}}{\left(q''_{conv,w}\right)_{exp/num}} \times 100\% \tag{5.3a}$$

$$(\text{error})_{rad} = \frac{\left(q''_{rad,w}\right)_{model} - \left(q''_{rad,w}\right)_{exp/num}}{\left(q''_{rad,w}\right)_{exp/num}} \times 100\% \tag{5.3b}$$

For the experimental data sets, $\left(q''_{rad,w}\right)_{exp/num}$ is calculated using the four surface radiation model of section 4.2.2, using the average of the blind slat temperatures measured in the experiments. For the numerical data sets, $\left(q''_{rad,w}\right)_{exp/num}$ is from the literature (Collins 2001).

5.2 Comparison with Experimental Results

Experimental results were obtained from the literature (Machin et al. 1998 and Collins et al. 2002b) and used to compare against the predicted results of the simplified model. Upon inspection of the work of Machin et al. (1998), there were only 3 sets of data that were useful for this comparison. These were for unheated blind slats at an angle of 90°, for three different blind-to-window spacings. These three data sets are used as the base case as none of the three adjustable constants affect the results for a blind slat angle of 90°. Collins et al. (2002b) had performed experimental work on 8 different cases, but again only three data sets were useful. These were for a heated blind slat at three different blind slat angles (45°, 0°, and -45 °). Four of the data sets are for bidirectional flow (where the ambient temperature is between the window and blind temperatures (See Appendix D)) and the fifth data set has some explained inaccuracy that made it unusable for this study. These three data sets were used to calculate the three constants to obtain better accuracy in the predicted results.

The constants are calculated to be: $C_1 = 1.21$, $C_2 = -1.05$ and $N = 0.24$ using the three experimental data sets of Collins et al. (2002b). This shows that the channel convective heat transfer coefficient is significantly increased with blind slat angle and the flat plate convective heat transfer coefficient is significantly decreased with blind slat angle. The effective channel width constant, N, that produces the best fit to the data is positive which shows that the effective channel width is larger than the distance between the blind slat tip and window surface.

The results of the comparisons between the experimental result and the simplified models results are shown in Table 4.1 and Table 5.1. These tables show that there is moderate agreement between the predicted model and the experimental work. Table 4.1 shows the comparison between the experimental work of Machin et al. (1998) and the predictions of the simplified model. The convective heat flux is predicted within 5%, but the radiative heat flux is between 18% and 26%. Table 5.1 compares the work of Collins et al. (2002b) and the simplified model. The convective heat flux and radiative heat flux both have a difference of 20% or better. This shows that when calibrating the constants for the three experimental cases of Collins et al. (2002b) and using the three experimental cases of Machin (1998) as the base cases, the predictions of the simplified model are reasonable for many design / modeling purposes.

5.3 Comparison with Numerical Results

Since there are only six useful experimental data sets, some of numerical data of Collins (2001) was used to calibrate the constants of the simplified model over a wider range of variables. The numerical data sets include three absorbed solar heat fluxes on the blind slats, two different window temperatures, three blind-to-window spacings, three blind emissivities, and three window emissivities. A sampling of fifty-four data sets was taken from the numerical work of Collins (2001) to calibrate the simplified model. The three constants were calculated to be $C_1 = 0.58$, $C_2 = 0.34$, and $N = -0.19$. Relative to the experimental results only, the constants have been significantly adjusted to fit the wider range of variables. Both the channel convective heat transfer coefficient and the flat plate convective heat transfer coefficient are increased as the blind slat angle increases, which is shown by the positive constants C_1 and C_2. The effective channel width is decreased by constant N, which shows that the effective channel width is smaller than the distance between the blind slat tips to window surface of the physical geometry.

Tables 5.2 through 5.4 show some comparisons between the numerical results and the simplified models predicted results. Table 5.2 shows comparison of the case where the blind slats are heated with an absorbed solar heat flux of 25 W/m^2 and there is a blind-to-window spacing of 20 mm. The percent error of the convective heat flux of this case is under 6%, but the radiative heat flux has a percent error of 30% to 59%. Table 5.3 shows the case where the blind-to-window spacing is 30 mm and the absorbed solar heat flux on the blind slats is 75 W/m^2. The convective heat flux is less accurate with a percent error of up to 35%, but the percent error of the radiative heat flux is within 5.5%. The last comparison of the numerical results discussed here is Table 5.4, which shows the convective heat flux has a percent error of 70% to 90%. It should be noted that this seems like a large error when presented in this way, but the absolute error is quite small

Table 5.1: Comparison of the experimental measurements (Collins et al. 2002b) with the current model for $\varepsilon_w = 0.81$, $\varepsilon_b = 0.81$, $q''_{solar} = 150\ W/m^2$, $T_w = 298\ K$, $T_\infty = 297\ K$, and $L = 379.6\ mm$.

SLAT ANGLE	**BLIND-TO-WINDOW SPACING**	**COLLINS ET AL. (2002B)**		**CURRENT STUDY**		**ERROR**	
ϕ	**n (mm)**	**$q''_{conv,w}$ (W/m^2)**	**$q''_{rad,w}$ (W/m^2)**	**$q''_{conv,w}$ (W/m^2)**	**$q''_{rad,w}$ (W/m^2)**	**CONV (%)**	**RAD (%)**
45°	15.4	-20.6	-28.24	-23.84	-33.76	15.73	19.55
0°	20.0	-25.1	-33.16	-20.45	-28.80	-18.53	-13.15
-45°	15.4	-28.9	-29.11	-30.85	-27.78	6.75	-4.57

Table 5.2: Comparison of the numerical results (Collins 2001) with the current model for $\varepsilon_w = 0.3$, $\varepsilon_b = 0.3$, $q''_{solar} = 25\ W/m^2$, $T_w = 297\ K$, $T_\infty = 297\ K$, and $L = 379.6\ mm$.

SLAT ANGLE	**BLIND-TO-WINDOW SPACING**	**COLLINS (2001)**		**CURRENT STUDY**		**ERROR**	
ϕ	**n (mm)**	**$q''_{conv,w}$ (W/m^2)**	**$q''_{rad,w}$ (W/m^2)**	**$q''_{conv,w}$ (W/m^2)**	**$q''_{rad,w}$ (W/m^2)**	**CONV (%)**	**RAD (%)**
45°	20.0	-7.70	-2.77	-8.16	-1.68	-5.97	39.28
0°	20.0	-8.71	-2.17	-8.62	-0.90	1.03	58.64
-45°	20.0	-6.47	-2.60	-6.80	-1.80	-5.09	30.76

Table 5.3: Comparison of the numerical results (Collins 2001) with the current model for $\varepsilon_w = 0.3$, $\varepsilon_b = 0.6$, $q''_{solar} = 75\ W/m^2$, $T_w = 311\ K$, $T_\infty = 297\ K$, and $L = 379.6\ mm$.

SLAT ANGLE	**BLIND-TO-WINDOW SPACING**	**COLLINS (2001)**		**CURRENT STUDY**		**ERROR**	
ϕ	**N (mm)**	**$q''_{conv,w}$ (W/m^2)**	**$q''_{rad,w}$ (W/m^2)**	**$q''_{conv,w}$ (W/m^2)**	**$q''_{rad,w}$ (W/m^2)**	**CONV (%)**	**RAD (%)**
45°	30.0	37.34	17.78	50.40	17.48	-34.97	1.69
0°	30.0	36.57	19.13	49.44	20.13	-35.20	-5.23
-45°	30.0	39.44	17.70	50.56	17.56	-28.19	0.79

Table 5.4: Comparison of the numerical results (Collins 2001) with the current model for $\varepsilon_w = 0.84$, $\varepsilon_b = 0.9$, $q''_{solar} = 125\ W/m^2$, $T_w = 297\ K$, $T_\infty = 297\ K$, and $L = 379.6\ mm$.

SLAT ANGLE	**BLIND-TO-WINDOW SPACING**	**COLLINS (2001)**		**CURRENT STUDY**		**ERROR**	
ϕ	**N (mm)**	**$q''_{conv,w}$ (W/m^2)**	**$q''_{rad,w}$ (W/m^2)**	**$q''_{conv,w}$ (W/m^2)**	**$q''_{rad,w}$ (W/m^2)**	**CONV (%)**	**RAD (%)**
45°	40.0	-7.08	-26.98	-0.45	-30.97	93.70	-14.78
0°	40.0	-7.26	-27.19	-0.74	-24.31	89.76	10.59
-45°	40.0	-1.58	-29.75	-0.33	-20.98	79.03	-4.15

as the convective heat flux is close to zero and a small quantity when compared with the dominant heat flux of radiation in this case, which is within 5.5%. This is the case where the absorbed solar heat flux is 125 W/m^2 and the blind-to-window spacing is 40 mm. These three comparisons show that the simplified model is not very accurate in these presented cases. Even though not presented here, the same can be seen across all fifty-four numerical data sets used. Of particular interest is the fact that the accuracy of the convective heat flux deteriorates as both the absorbed solar heat flux increases and the blind-to-window spacing increases.

It was discovered that at a larger blind-to-window spacing and higher absorbed solar heat flux, the convective heat transfer predicted by the numerical work varied by a substantial amount according to different blind slat angles. For instance, looking closer at Table 5.4 where the blind-to-window spacing is 40 mm and the absorbed solar heat flux is 125 W/m^2, it can be seen that the convective heat flux for a blind slat angle of -45° from Collins (2001) is -7.08 W/m^2 and for 0° it is -7.26 W/m^2, but for an angle of 45° the convective heat flux is only -1.58 W/m^2. Table 5.4 also shows that for the current model, the convective heat flux is -0.45 W/m^2 for -45°, -0.74 W/m^2 for the 0° and -0.33 W/m^2 for 45°. The simplified model can not predict a low enough convective heat flux in these cases. Between the 45° and -45° cases, the predicted convective heat flux has a difference of 26.7%, where the numerical data in these two cases has a difference of 77.7%. The model presented here cannot predict this large change of convective heat flux with blind slat angle, especially since in this model both the -45° and 45° cases are calculated very similarly. This is due to the fact that the only factors that are adjusted based on blind slat angle are the radiation model and the effective channel width. The radiation model only affects the results of the radiative heat flux and the effective channel width only varies by about 3 mm between the -45° and 45° blind slat angle cases, which is not enough to account for the large change in convective heat flux based on blind slat angle shown by the numerical data of Collins (2001). This discrepancy motivated an experimental study of a larger blind-to-window spacing and higher absorbed solar heat flux to investigate the accuracy of the numerical work.

5.3.1 Experimental Results of a Larger Blind-to-Window Spacing and Higher Absorbed Solar Heat Flux on the Blind Slats

An interferometric study was performed on a window with a Venetian blind at a larger blind-to-window spacing and a higher absorbed solar heat flux to validate some of the results found in the numerical work of Collins (2001). The same apparatus that was used by Collins et al. (2002b) experimental work is used to perform this experiment. This apparatus is the same geometry used by the simplified model in the previous chapter (refer to Figure 4.1(a)). A painted aluminum plate is used to simulate the window surface. The aluminum plate has a height of 379.6 mm and is set to the ambient temperature of 295.5 K. The blind slats are from a commercially available aluminum Venetian blind. The geometry of the Venetian blind is the same as those presented in the previous chapter (refer to Figures 4.1 and 4.3). The absorbed solar heat flux of the blind slats is set to 125 W/m^2 by using two thin foil electric heaters. The blind-to-window spacing is set to 40 mm. The emissivities of the blind and the window are both the same at 0.81. Three different blind slat angles (-45°, 0°, and 45°) are used to compare with the numerical results.

A 200 mm diameter beam Mach-Zehnder interferometer (MZI) was used to visualize the temperature field. A plan view of the MZI is shown in Figure 5.1. The beam from a 15 mW He-Ne laser is split into two beams of approximately the same intensity and in the same phase. One of the beams passes through the ambient air, which is the reference beam, and the other beam, which is the test beam, passes through the experimental model. The heated air in the experimental model causes the index of refraction to change in the test beam, which causes the test beam to be out of phase with the reference beam. When these two beams are combined, the phase shift produces a pattern in the output of the MZI, which is what is photographed and presented in Figure 5.2. The isotherms in the infinite fringe mode shown in Figure 5.2 are constructive and deconstructive interference fringes that are produced when the reference beam and the test beam are parallel when they are combined. Interferometry can be used to determine the heat transfer rates, but only the temperature field visualization is required for this study.

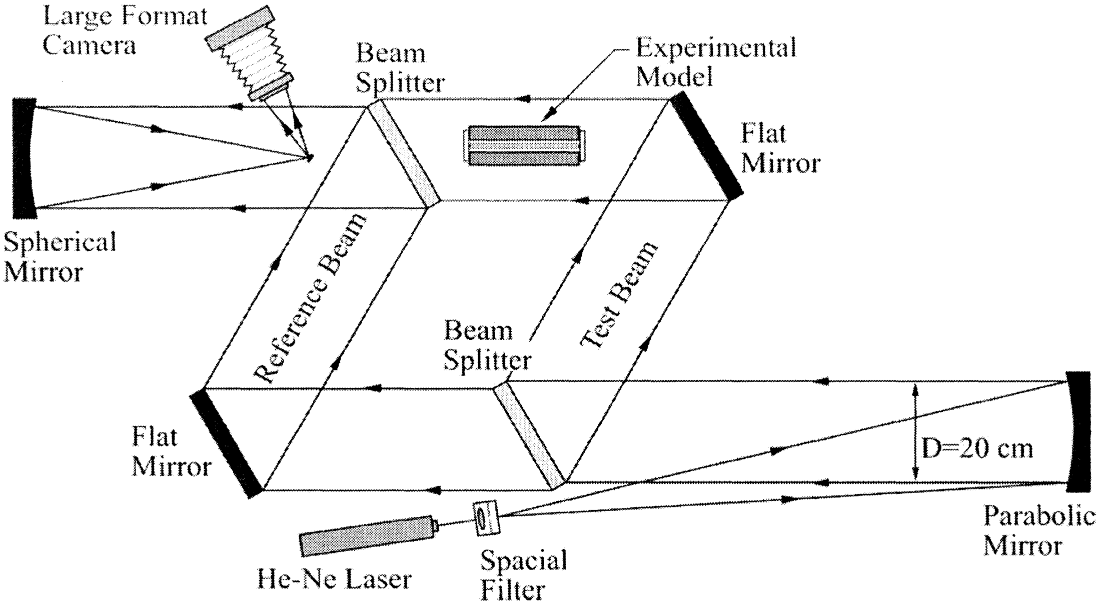
Large Format Camera
Beam Splitter
Experimental Model
Flat Mirror
Spherical Mirror
Reference Beam
Test Beam
Beam Splitter
Flat Mirror
D=20 cm
Parabolic Mirror
He-Ne Laser
Spacial Filter

Figure 5.1: Plan view of a Mach-Zehnder Interferometer (not to scale).

Figure 5.2 shows the infinite fringe interferometric pictures of the window and Venetian blind system. This figure shows that the approximation of the Venetian blind being impermeable in the simplified model is not an accurate approximation for larger blind-to-window spacings and higher absorbed solar heat fluxes. Looking at Figures 5.2(a) and 5.2(b), with blind slat angles of -45° and 0 °, it can be seen that the heat flow is entrained through the blind slats from the ambient and onto the window glazing. This shows that the heat transfer of the window is increased over the amount the approximated model can predict. The other blind slat angle of 45°, in Figure 5.2(c), shows that the air is entrained from the channel between the window and blind slats and into the ambient. This increases the heat transfer into the room and decreases the heat transfer on the window. Figure 5.2 shows that as both the blind-to-window spacing and absorbed solar heat flux are increased the approximations made by the simplified model are no longer valid. This experimental case also shows that the heat flow of complex fenestration systems is more complex than initially thought when this simplified model was developed.

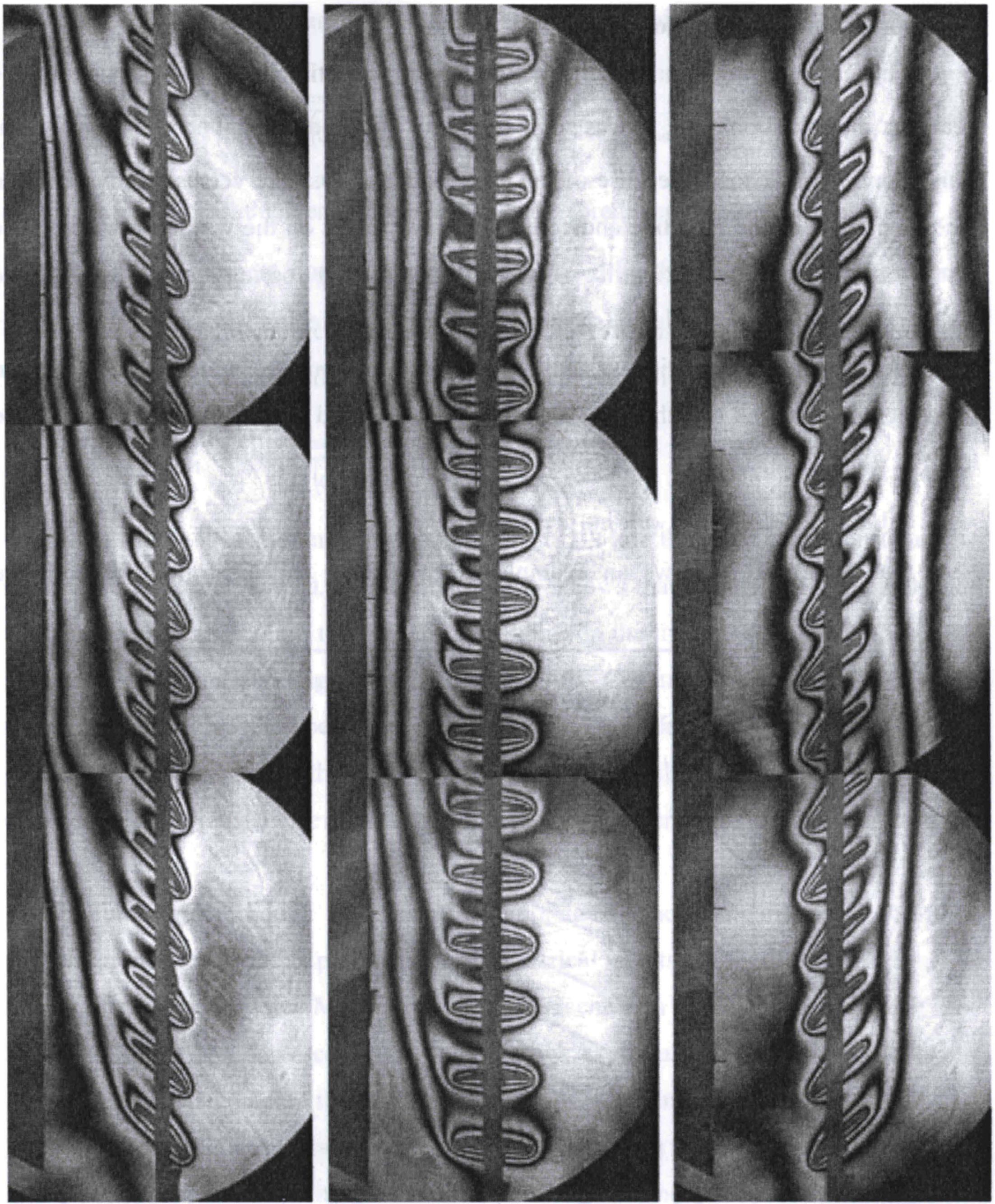

(a) (b) (c)

Figure 5.2: Interferometric pictures of a window with a Venetian blind on the inside window surface with test conditions of $T_\infty = 22.5$ *°C,* $T_w = 22.5$ *°C,* $\varepsilon_p = 0.81$*,* $\varepsilon_w = 0.81$*,* $q''_{solar} = 125$ W/m^2, and n = 40 mm at (a)$\phi = -45°$, (b) $\phi = 0°$, (c) $\phi = 45°$.

5.4 Room Heat Transfer Comparisons

Instead of trying to predict the radiation and convection heat fluxes separately, the heat flux into the room, q''_{room}, was compared with the experimental and numerical data. This quantity was chosen because of the issue with the absolute versus relative error in the comparison of the radiative and convective heat fluxes on the window surface. The heat flux into the room is primarily of interest in predicting cooling loads as well. If we take a room as a control volume, shown in Figure 5.3, there are 3 inputs of heat transfer from the complex fenestration system: (i) convection from the window, (ii) radiation from the window, and (iii) the solar absorption of the blind slats. The heat flux into the room is:

$$q''_{room} = q''_{solar} + q''_{conv,w} + q''_{rad,w} \tag{5.4}$$

Note that section B.3 shows an example of calculating this heat flux for both the

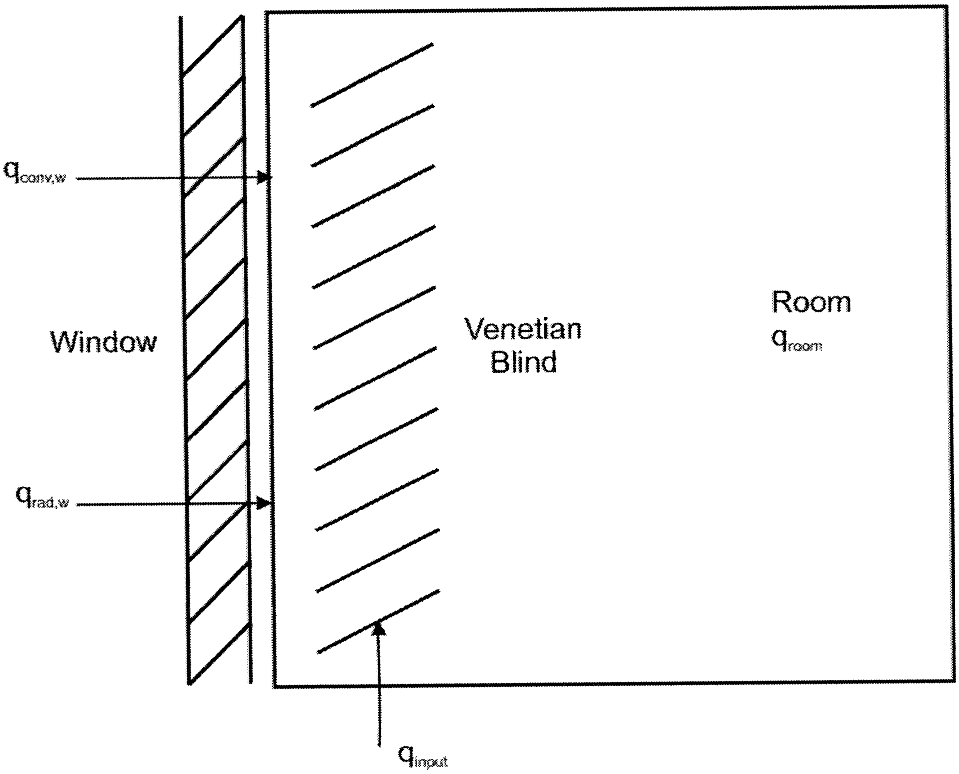

Figure 5.3: Diagram of a control volume of a room with the complex fenestration system as the only source of heat input or output.

predicted model and an experimental case. The sum-squared error of the room, E_{room}, is:

$$E_{room} = \sum_{i=1}^{K}\left(\left(\frac{\left(q''_{room}\right)_{model} - \left(q''_{room}\right)_{exp/num}}{\left(q''_{room}\right)_{exp/num}}\right)^2\right)_i \tag{5.5}$$

where $\left(q''_{room}\right)_{model}$ is the heat flux into the room predicted by the current model and $\left(q''_{room}\right)_{exp/num}$ is the heat flux of the room determined by the experimental or numerical data. Again, the sum-squared error of the room heat flux is minimized by adjusting the three constants in the simplified model. The percent error of the room heat flux is:

$$(\text{error})_{room} = \frac{\left(q''_{room}\right)_{model} - \left(q''_{room}\right)_{exp/num}}{\left(q''_{room}\right)_{exp/num}} \times 100\% \tag{5.6}$$

The least squares minimization of the heat flux into the room gives constants C_1 = 0.28, C_2 = 0.10, and N = -0.12. The constant N shows that the effective channel width uses a closer channel width than the distance between the tip of the blind slat to window surface as the blind slat angle decreases from 90°. Constant C_1 increases the channel convective heat transfer coefficient as blind slat angle decreases from 90°, which is dominant in this case. On the other hand, there is only a slight increase in the flat plate convective heat transfer coefficient as blind slat angle decreases, as shown by constant C_2.

Tables 5.5 through 5.8 show a sampling of the comparisons between the simplified model and the experimental and numerical results. It should be noted that the results of comparison with Machin (1998) are presented in Table 4.1 because at a blind slat angle of 90°, the three constants do not apply, as discussed in the previous chapter. Tables 4.1 and 5.5 compare the experimental results (Machin et al. 1998 and Collins et al. 2002b) and the predicted results of the simplified model. In these two tables the heat flux into the room is predicted within 24%. In Table 5.5, the window convective and radiative heat fluxes still have a high inaccuracy, with the percent error being as high as about 95%. This experimental case shows that a higher absorbed solar heat flux (150 W/m^2) on the blind slats increases the inaccuracy of the simplified model even at a smaller blind-to-window spacing (15.4 mm – 20.0 mm).

Tables 5.6 through 5.8 are a sampling of the results of the numerical results of Collins (2001) compared with the predicted results of the simplified model. Further results are presented in Appendix D. All three tables show that the predicted results agree with the numerical data within 11% for the heat flux into the room. The same trend applies as before to the comparisons in that the larger the blind-to-window spacing and higher the absorbed solar heat flux, the more inaccurate the window convective heat flux of the simplified model becomes. This can easily be seen in Table 5.8, as at both low blind-to-window spacing (20 mm) and low absorbed solar heat flux (25 W/m^2), the convective heat flux is within 19%, but the radiative heat flux is within 42%. In Table 5.9, at both high blind-to-window spacing (40 mm) and high absorbed solar heat flux (125 W/m^2), the window convective heat flux is predicted within 95%, but the radiative heat flux is within 26%. This trend is also shown across the additional 45 data sets presented in Appendix D. The window convective and radiative heat fluxes are not predicted very well with this simplified model, but the heat flux into the room can be predicted more accurately.

Table 5.5: Comparison of the experimental measurements (Collins et al. 2002b) with the current model for $\varepsilon_w = 0.81$, $\varepsilon_b = 0.81$, $q''_{solar} = 150\ W/m^2$, $T_w = 298\ K$, $T_\infty = 297\ K$, and $L = 379.6\ mm$.

SLAT ANGLE	**BLIND-TO-WINDOW SPACING**	**COLLINS ET AL. (2002b)**		**CURRENT STUDY**		**ERROR**		**COLLINS ET AL. (2002b)**	**CURRENT STUDY**	**ERROR**
ϕ	**n (mm)**	$q''_{conv,w}$ **(W/m^2)**	$q''_{rad,w}$ **(W/m^2)**	$q''_{conv,w}$ **(W/m^2)**	$q''_{rad,w}$ **(W/m^2)**	**CONV (%)**	**RAD (%)**	q''_{room} **(W/m^2)**	q''_{room} **(W/m^2)**	**ROOM (%)**
-45°	15.4	-28.9	-29.11	-53.90	-27.03	86.50	-7.15	91.99	69.08	-24.91
0°	20.0	-25.1	-33.16	-42.23	-23.81	68.25	-28.21	91.74	83.97	-8.48
45°	15.4	-20.6	-28.24	-40.18	-30.67	95.02	8.62	101.16	79.15	-21.76

Table 5.6: Comparison of the numerical results (Collins 2001) with the current model for $\varepsilon_w = 0.3$, $\varepsilon_b = 0.3$, $q''_{solar} = 25\ W/m^2$, $T_w = 297\ K$, $T_\infty = 297\ K$, and $L = 379.6\ mm$.

SLAT ANGLE	**BLIND-TO-WINDOW SPACING**	**COLLINS (2001)**		**CURRENT STUDY**		**ERROR**		**COLLINS (2001)**	**CURRENT STUDY**	**ERROR**
ϕ	**n (mm)**	$q''_{conv,w}$ **(W/m^2)**	$q''_{rad,w}$ **(W/m^2)**	$q''_{conv,w}$ **(W/m^2)**	$q''_{rad,w}$ **(W/m^2)**	**CONV (%)**	**RAD (%)**	q''_{room} **(W/m^2)**	q''_{room} **(W/m^2)**	**ROOM (%)**
-45°	20.0	-7.70	-2.77	-8.84	-1.97	14.82	-28.92	14.53	14.19	-2.33
0°	20.0	-8.71	-2.17	-10.32	-1.26	18.52	-41.71	14.12	13.41	-5.01
45°	20.0	-6.47	-2.60	-7.20	-2.07	11.32	-20.22	15.93	15.72	-1.30

Table 5.7: Comparison of the numerical results (Collins 2001) with the current model for $\varepsilon_w = 0.3$, $\varepsilon_b = 0.6$, $q''_{solar} = 75\ W/m^2$, $T_w = 311\ K$, $T_\infty = 297\ K$, and $L = 379.6\ mm$.

SLAT ANGLE	**BLIND-TO-WINDOW SPACING**	**COLLINS (2001)**		**CURRENT STUDY**		**ERROR**		**COLLINS (2001)**	**CURRENT STUDY**	**ERROR**
ϕ	**n (mm)**	$q''_{conv,w}$ **(W/m^2)**	$q''_{rad,w}$ **(W/m^2)**	$q''_{conv,w}$ **(W/m^2)**	$q''_{rad,w}$ **(W/m^2)**	**CONV (%)**	**RAD (%)**	q''_{room} **(W/m^2)**	q''_{room} **(W/m^2)**	**ROOM (%)**
-45°	30.0	37.34	17.78	50.80	16.58	36.05	-6.76	130.12	142.38	9.42
0°	30.0	36.57	19.13	49.97	19.11	36.63	-0.11	130.70	144.07	10.23
45°	30.0	39.44	17.70	50.99	16.63	29.27	-6.02	132.14	142.62	7.93

Table 5.8: Comparison of the numerical results (Collins 2001) with the current model for $\varepsilon_w = 0.84$, $\varepsilon_b = 0.9$, $q''_{solar} = 125\ W/m^2$, $T_w = 297\ K$, $T_\infty = 297\ K$, and $L = 379.6\ mm$.

SLAT ANGLE	**BLIND-TO-WINDOW SPACING**	**COLLINS (2001)**		**CURRENT STUDY**		**ERROR**		**COLLINS (2001)**	**CURRENT STUDY**	**ERROR**
ϕ	**n (mm)**	$q''_{conv,w}$ **(W/m^2)**	$q''_{rad,w}$ **(W/m^2)**	$q''_{conv,w}$ **(W/m^2)**	$q''_{rad,w}$ **(W/m^2)**	**CONV (%)**	**RAD (%)**	q''_{room} **(W/m^2)**	q''_{room} **(W/m^2)**	**ROOM (%)**
-45°	40.0	-7.08	-26.98	-0.42	-33.95	-94.11	25.81	90.94	90.64	-0.33
0°	40.0	-7.26	-27.19	-0.66	-28.88	-90.89	6.21	90.55	95.46	5.42
45°	40.0	-1.58	-29.75	-0.31	-33.96	-80.19	14.15	93.67	90.73	-3.14

Chapter 6

Summary, Conclusions and Recommendations

6.1 Summary and Conclusions

A simplified model has been developed to predict the convective and radiative heat transfer rates through a complex fenestration system. This model was developed for a Venetian blind located on the indoor window surface. The solution of the simplified model applies to "daytime" and "nighttime" conditions, including the effects of solar irradiation on the blind surfaces.

The model consisted of utilizing a four surface radiation model to determine the radiative heat transfer and an approximation was used for the convective heat transfer. The Venetian blind layer in the simplified model was approximated as an impermeable flat plate for the convective heat transfer. This created a flat plate convective flow from the Venetian blind to the ambient and a convective channel flow between the Venetian blind and the window surface. The convective flat plate heat transfer was determined from Churchill and Chu (1972). For the convective channel heat flow, the heat transfer of each channel wall was required, but simple correlations were not readily available from the literature. Therefore, a numerical study was performed to develop correlations to determine the heat transfer of each channel wall separately in a channel flow.

Laminar free convective heat transfer in an asymmetrically, isothermally heated vertical channel has been solved numerically in order to develop empirical correlations for use in the simplified model. There are two key components to the parametric study that was performed on this data:

- Multiple characteristic temperature differences were tested for the hot wall average Nusselt numbers, but the numerical data collapsed onto almost a single curve when using a blended characteristic temperature difference. The hot wall average Nusselt number data was then correlated using the method of Churchill and Usagi (1972) because the numerical data provided two clear asymptotes at upper and lower modified Rayleigh numbers.

- A heat balance was used for developing the cold wall average Nusselt number. This involved using the previously developed hot wall average Nusselt number correlation and an overall channel average Nusselt number correlation from the literature.

These correlations were needed in the simplified model, but they will also be applicable to many other engineering applications.

Once the convective and radiative heat transfers were determined by the simplified model, the results were compared with the existing experimental and numerical data of Machin (1998), Collins et al. (2002b) and Collins (2001). The simplified model produced poor agreement with the experimental and numerical data when comparing the convective / radiative split at the window glazing surface. Because of this the heat transfer into the room was used as comparison. The simplified model predicted the heat transfer into the room within about 25% of the experimental and numerical data. When looking at the convective heat transfer more closely, two trends were observed in the simplified models predicted results:

- As the blind-to-window spacing increased, the convective heat transfer decreased in accuracy.
- As the absorbed solar heat flux on the blind slats increased, the convective heat transfer decreased in accuracy.

Because of the larger inaccuracy of the simplified models predicted results at higher blind-to-window spacing and higher absorbed solar heat flux on the blind slats, an interferometric study was performed.

An interferometric experiment was conducted with a Venetian blind located at the indoor window surface. This experimental study was used to visualize the interaction of the fluid flow between a Venetian blind and the indoor window surface for the conditions of a large blind-to-window spacing and a high solar absorbed heat flux on the blind slats. Three different blind slat angles were used to investigate the flow pattern. This study showed that:

- For blind slat angles of 0° and -45°, the air flowed from the ambient side of the Venetian blind through the blind slats and onto the window surface.

This increased the amount of heat transfer on the window surface because the heat generated at the blind surfaces transferred towards the window.

- For a blind slat angle of 45°, the air flowed from the window surface through the blind slats and into the ambient room. This decreased the amount of heat transfer at the window surface because the heat generated by both the window and blind surfaces was transferred away from the window and into the ambient room.

This experimental study showed that the approximation of the simplified model was not valid for larger blind-to-window spacing and higher solar absorbed heat flux on the blind slats. With these two conditions, the approximation of the Venetian blind as an impermeable flat plate (with convective channel heat transfer between the window surface and the blind layer and convective flat plate heat transfer between the blind layer and the ambient room) was not a reasonable approximation to the experimental case. The experimental flow is dependent on the blind slat angle, which could not be satisfied by the current simplified model.

6.2 Recommendations

Because of the complex flow found in the interferometric study, it is of the opinion of the author that there is not much more that can be done to improve the simplified model presented in this thesis. The approximation used is appropriate for close blind-to-window spacings and a low amount of absorbed solar heat flux on the blind slats. At larger blind-to-window spacings and higher absorbed solar heat flux on the blind slats, there is a significant change in the flow pattern that requires further study and possibly a different approach to apply a simplified calculation of the heat transfer. Some recommendations for further work are as follows:

1. Further experimental study of a Venetian blind located at the indoor window surface would be beneficial. It was found that there were only a few useable experimental data points available in the literature. Most of the useable experimental data concentrated on close blind-to-window spacings. Further experimental work at larger blind-to-window spacings would verify the numerical data used to calibrate the simplified model. Also, because of the

complex flow found in the experimental study, it would be of great interest to further examine the flow at different blind slat angles and larger blind-to-window spacings.

2. This simplified model only considers cases where both the window and the blind are heated at or above the ambient temperature of the room so that the fluid flow is unidirectional. It would be of interest to study the interaction of the Venetian blind and the indoor window surface in a bidirectional flow, where the blind slats are heated above the ambient temperature and the window surface is below the ambient temperature. This may create instability in the flow, which might require turbulence modeling. A few cases were performed experimentally by Collins et al. (2002b), but further study both experimentally and numerically would be useful. This could be extended to develop a similar simplified model to the current study that included the bidirectional flow cases.
3. Similar to the previous suggestion, a correlation could be developed for bidirectional natural convective flow in an asymmetrically heated vertical channel similar to the method used to develop the hot and cold wall average Nusselt number correlations in this thesis. Experimental and numerical work could be used to obtain data that could be used in a parametric study to develop correlations. Some numerical work has been attempted as shown in Appendix E. Only a few data points were obtained because the flow is very unstable. This will require a transient or turbulence model to obtain a wider range of results, especially at larger modified Rayleigh numbers. It would be beneficial not only to complex fenestration modeling, but also for many other engineering applications to have correlations to determine the overall channel, hot wall, and cold wall average Nusselt numbers of a bidirectional natural convective flow inside an asymmetrically heated vertical channel.
4. Turbulent flow in a complex fenestration system could also be studied. Many realistic complex fenestration systems involve windows of large heights, which may involve some turbulent flow. A current study at Ryerson University involves an experiment with a complex fenestration

system with a larger height. This larger height is to investigate the transition zone between the laminar and turbulent zone in the complex fenestration system. It is of great interest to study the effect of turbulence has on the heat transfer in a complex fenestration system.

5. This simplified model is for the center of glass region of the complex fenestration system only. In order for this model to be more accurate for realistic conditions, the edge of glass and frame effects should be studied. When including a Venetian blind on the indoor window surface, the geometry of the framing and Venetian blind have many variations, which may require multiple studies.

APPENDIX A

Richardson Extrapolation Performed on the Numerical Model

A.1 Introduction

The Richardson extrapolation (Celik, 2006) is used in Chapter 2 to report the discretization error estimation of the two grids that are used in the numerical solution. This method is calculated in this appendix for the two grids that are used in this study. Both grids are composed of the same number of nodes, but Grid 1, used for low modified Rayleigh number solutions, has a channel aspect ratio of 100, and Grid 2, used for high modified Rayleigh number solutions, has a channel aspect ratio of 50. Both of these grids are analyzed to ensure that the numerical solution is reasonable.

A.2 Calculation of the Estimation of Discretization Error for Grid 1

This is the Richardson extrapolation calculation for Grid 1, which has a channel aspect ratio of 100 for use in the numerical solution at low modified Rayleigh numbers.

Step 1: The first step of the Richardson extrapolation is to determine three representative grid sizes: h_1, h_2, and h_3 such that $h_1 < h_2 < h_3$.

$$h_1 = \left[\frac{1}{N}\sum_{i=1}^{N}\Delta A_i\right]^{\frac{1}{2}} = \left[\frac{1}{81201}541\right]^{\frac{1}{2}} = 0.082$$

$$h_2 = \left[\frac{1}{N}\sum_{i=1}^{N}\Delta A_i\right]^{\frac{1}{2}} = \left[\frac{1}{41956}541\right]^{\frac{1}{2}} = 0.114 \qquad \text{(A.1)}$$

$$h_3 = \left[\frac{1}{N}\sum_{i=1}^{N}\Delta A_i\right]^{\frac{1}{2}} = \left[\frac{1}{21076}541\right]^{\frac{1}{2}} = 0.160$$

Step 2: These three grids are then used to solve for the critical variable, ϕ, which is $\overline{Nu}_{O,\overline{\Delta T}}$ in this case.

$$\phi_1 = \overline{Nu}_{O,\overline{\Delta T},1} = 0.04086$$

$$\phi_2 = \overline{Nu}_{O,\overline{\Delta T},2} = 0.04091$$

$$\phi_3 = \overline{Nu}_{O,\overline{\Delta T},3} = 0.04097$$

Step 3: The apparent order, p, of the method is calculated next using an iterative method.

$$p = \frac{1}{\ln(r_{21})}\left|\ln\left|\frac{\varepsilon_{32}}{\varepsilon_{21}}\right| + q(p)\right| \tag{A.2}$$

$$q(p) = \ln\left(\frac{r_{21}^{p} - s}{r_{32}^{p} - s}\right) \tag{A.3}$$

$$s = 1 \cdot \mathrm{sign}\left(\frac{\varepsilon_{32}}{\varepsilon 21}\right) \tag{A.4}$$

where

$$\varepsilon_{32} = \phi_3 - \phi_2 = 6.0 \times 10^{-5}, \tag{A.5a}$$

$$\varepsilon_{21} = \phi_2 - \phi_1 = 5.0 \times 10^{-5}, \tag{A.5b}$$

$$r_{21} = \frac{h_2}{h_1} = 1.390, \text{ and} \tag{A.6a}$$

$$r_{32} = \frac{h_3}{h_2} = 1.404\,. \tag{A.6b}$$

It should also be noted that:

$$\mathrm{sign}(x) = \begin{cases} -1 & \rightarrow \quad x < 0 \\ 0 & \rightarrow \quad x = 0 \\ 1 & \rightarrow \quad x > 0 \end{cases} \tag{A.7}$$

The apparent order of this grid: p = 0.1168.

Step 4: The extrapolated values are:

$$\begin{aligned} \phi_{ext}^{21} &= \frac{r_{21}^{p}\phi_1 - \phi_2}{r_{21}^{p} - 1} = 0.04055 \\ \phi_{ext}^{32} &= \frac{r_{32}^{p}\phi_2 - \phi_3}{r_{32}^{p} - 1} = 0.04055 \end{aligned} \tag{A.8}$$

Step 5: The approximate relative error:

$$e_a^{21} = \left|\frac{\phi_1 - \phi_2}{\phi_1}\right| = 0.0012 \rightarrow 0.12\% \tag{A.9}$$

RYERSON UNIVERSITY LIBRARY

The extrapolated relative error:

$$e_{ext}^{21} = \left|\frac{\phi_{ext}^{21} - \phi_1}{\phi_{ext}^{21}}\right| = 0.0075 \rightarrow 0.75\% \tag{A.10}$$

The fine grid convergence index:

$$GCI_{fine}^{21} = \frac{1.25e_a^{21}}{r_{21}^p - 1} = 0.0094 \rightarrow 0.94\% \tag{A.11}$$

The approximate relative error, the extrapolated relative error, the fine grid convergence index, and the apparent order of the method are all reported here. For Grid 1, the numerical uncertainty is 0.94%.

A.3 Calculation of the Estimation of Discretization Error for Grid 2

This is the Richardson extrapolation calculation for Grid 2, which is used for the numerical solution at high modified Rayleigh numbers.

Step 1: The three grid sizes are:

$$\begin{aligned} h_1 &= \left[\frac{1}{N}\sum_{i=1}^{N}\Delta A_i\right]^{\frac{1}{2}} = \left[\frac{1}{81201}491\right]^{\frac{1}{2}} = 0.078 \\ h_2 &= \left[\frac{1}{N}\sum_{i=1}^{N}\Delta A_i\right]^{\frac{1}{2}} = \left[\frac{1}{41956}491\right]^{\frac{1}{2}} = 0.108 \\ h_3 &= \left[\frac{1}{N}\sum_{i=1}^{N}\Delta A_i\right]^{\frac{1}{2}} = \left[\frac{1}{21076}491\right]^{\frac{1}{2}} = 0.153 \end{aligned} \tag{A.1}$$

Step 2: The critical variables of the solved three grids:

$$\phi_1 = \overline{Nu}_{O,\overline{\Delta T},1} = 3.352$$

$$\phi_2 = \overline{Nu}_{O,\overline{\Delta T},2} = 3.360$$

$$\phi_3 = \overline{Nu}_{O,\overline{\Delta T},3} = 3.361$$

Step 3: The apparent order of Grid 2, p = 3.505 where:

$$\varepsilon_{32} = 0.001, \tag{A.5a}$$

$$\varepsilon_{21} = 0.008, \tag{A.5b}$$

$$r_{21} = 1.390, \text{ and} \tag{A.6a}$$

$$r_{32} = 1.404. \tag{A.6b}$$

Step 4: The extrapolated values are:

$$\phi_{ext}^{21} = \frac{r_{21}^{p}\phi_1 - \phi_2}{r_{21}^{p} - 1} = 3.351$$
$$\phi_{ext}^{21} = \frac{r_{32}^{p}\phi_2 - \phi_3}{r_{32}^{p} - 1} = 3.360 \tag{A.8}$$

Step 5: The approximate relative error:

$$e_a^{21} = \left|\frac{\phi_1 - \phi_2}{\phi_1}\right| = 0.0024 \rightarrow 0.24\% \tag{A.9}$$

The extrapolated relative error:

$$e_{ext}^{21} = \left|\frac{\phi_{ext}^{21} - \phi_1}{\phi_{ext}^{21}}\right| = 0.0003 \rightarrow 0.03\% \tag{A.10}$$

The fine grid convergence index:

$$GCI_{fine}^{21} = \frac{1.25e_a^{21}}{r_{21}^{p} - 1} = 0.0004 \rightarrow 0.04\% \tag{A.11}$$

The numerical uncertainty of Grid 2 is 0.04%.

Appendix B

Sample Calculation of the Simplified Model

B.1 Problem Introduction

This section is a companion to Chapter 4, as a sample calculation is presented here to further explain the process described in Chapter 4. The calculation is based on an experimental case performed by Collins et al. (2002b). The main properties of this case are: (i) the blind slat is at an angle, ϕ, of 45°, (ii) the blinds have an absorbed solar heat flux, q''_{solar}, of 150 W/m^2, (iii) the window temperature, T_w, is at 298 K, and (iv) the ambient temperature, T_∞, is at 297 K. The geometry of the blind and window is shown in Figure 4.1(a) and the geometry of the channel and flat plate approximation is shown in Figure 4.1(b). The geometric measurements, some properties of the ambient air, and some constants that are used in this calculation are presented in Table B.1. The properties of air are determined from Touloukian et al. (1970), Touloukian et al. (1975), Touloukian and Malita (1970), and Incropera and DeWitt (2002). Since this is an iterative method, an initial guess of the blind temperature is required. For this calculation the blind temperature, T_b, is initially set to 305 K.

Table B.1: Geometric measurements, constants, and properties of the ambient air at 297 K determined from Touloukian et al. (1970), Touloukian et al. (1975), Touloukian and Malita (1970), and Incropera and DeWitt (2002).

ps (mm)	**w (mm)**	**r_c (mm)**	**n (mm)**	**L (mm)**
22.2	25.4	0.0523	15.4	379.6
ε_w	ε_b	ε_∞	**g (m/s^2)**	**σ (W/m^{2}K^4)**
0.81	0.81	1	9.81	5.67×10^{-8}
k_f (W/mK)	**ρ (kg/m^3)**	**β (1/K)**	**ν_f (m^2/s)**	**Pr**
0.026	1.17	3.33×10^{-3}	1.59×10^{-5}	0.707

B.1.1 Effective Channel Width

The effective channel width (b_{eff}) geometry is shown in Figure 4.3 along with the effect of the blind curvature spacing, t. The correction factor N is -0.12, as determined in Section 5.4. The curvature spacing is calculated from equation (4.2):

$$t = r_c \cdot \left(1 - \cos\left(\frac{w}{2 \cdot r_c}\right)\right) = 0.0523\text{mm} \cdot \left(1 - \cos\left(\frac{0.0254\text{m}}{2 \cdot 0.0523\text{m}}\right)\right) = 1.534 \times 10^{-3}\text{m}$$

The effective blind width is determined from equation (4.1):

$$b_{eff} = n - \frac{w}{2}\cos(\phi) + t \cdot \sin(\phi) + N \cdot \frac{w}{2} \cdot \cos(\phi)$$

$$b_{eff} = 0.0154\text{m} - \frac{0.0254\text{m}}{2} \cdot \cos(45°) + 1.534 \times 10^{-3}\text{m} \cdot \sin(45°) +$$

$$(-0.12) \cdot \frac{0.0254\text{m}}{2} \cdot \cos(45°)$$

$$b_{eff} = 6.427 \times 10^{-3}\text{m}$$

B.2: Energy Balance

The energy balance on a single blind slat is given by equation (4.3):

$$q_{solar} = F_1 \cdot q_{conv,ch} + F_2 \cdot q_{conv,fp} + q_{rad} \tag{4.3}$$

The solar heat absorbed by the blind is calculated through the absorbed solar heat flux given in the problem statement. For a single blind of a unit length:

$$q_{solar} = q''_{solar} \cdot w \cdot L = 150\frac{\text{W}}{\text{m}^2} \cdot 0.0254\text{m} \cdot 1\text{m} = 3.81\text{W}$$

B.2.1: Hottel's Crossed String Method

The four surface radiation model is shown in Figure 4.6(c) with number labels for each surface and letter labels for each corner. The view factors are required to determine the radiative heat transfer rates of each surface. The lengths between the points are calculated for the view factor calculations:

$$AB = ps = 22.2\text{mm}$$

$$AC = w = 25.4\text{mm}$$

$$AD = \left(w^2 + ps^2 - 2 \cdot w \cdot ps \cdot \cos(\phi)\right)^{0.5}$$

$$AD = \left((25.4\mathrm{mm})^2 + (22.2\mathrm{mm})^2 - 2 \cdot 25.4\mathrm{mm} \cdot 22.2\mathrm{mm} \cdot \cos(45°)\right)^{0.5} = 18.45\mathrm{mm}$$

$$BC = \left(w^2 + ps^2 - 2 \cdot w \cdot ps \cdot \cos(\gamma)\right)^{0.5}$$

$$BC = \left((25.4\mathrm{mm})^2 + (22.2\mathrm{mm})^2 - 2 \cdot 25.4\mathrm{mm} \cdot 22.2\mathrm{mm} \cdot \cos(135°)\right)^{0.5} = 43.99\mathrm{mm}$$

$$BD = w = 25.4\mathrm{mm}$$

$$CD = ps = 22.2\mathrm{mm}$$

The view factors are determined from Hottel's crossed strings method (Hottel 1967) as described in section 4.2.1 and equation (4.4):

$$F_{k-i} = \frac{\sum\left(\text{Crossed strings}\right) - \sum\left(\text{uncrossed strings}\right)}{2 \cdot \text{Length } k}$$

$$F_{1-1} = 0$$

$$F_{1-2} = \frac{(AC + AB) - (BC)}{2 \cdot AB} = \frac{(25.4\mathrm{mm} + 22.2\mathrm{mm}) - (43.99\mathrm{mm})}{2 \cdot 22.2\mathrm{mm}} = 0.081$$

$$F_{1-3} = \frac{(AD + BC) - (AC + BD)}{2 \cdot AB}$$

$$F_{1-3} = \frac{(18.45\mathrm{mm} + 43.99\mathrm{mm}) - (25.4\mathrm{mm} + 25.4\mathrm{mm})}{2 \cdot 22.2\mathrm{mm}} = 0.263$$

$$F_{1-4} = \frac{(AB + BD) - (AD)}{2 \cdot AB} = \frac{(22.2\mathrm{mm} + 25.4\mathrm{mm}) - (18.45\mathrm{mm})}{2 \cdot 22.2\mathrm{mm}} = 0.656$$

To check that the view factors are correct, the sum of all the view factors should be 1:

$$\sum_{k=1}^{4} F_{1-k} = 0 + 0.081 + 0.263 + 0.656 = 1$$

Similar calculations are applied to the other 3 surfaces, but will not be reproduced here. The view factors are presented in Table B.2.

Table B.2: View factors calculated from Hottel's crossed strings method (Hottel 1967) for use in the four surface radiation model.

$F_{1\text{-}1} = 0$	$F_{2\text{-}1} = 0.071$	$F_{3\text{-}1} = 0.263$	$F_{4\text{-}1} = 0.574$
$F_{1\text{-}2} = 0.081$	$F_{2\text{-}2} = 0$	$F_{3\text{-}2} = 0.656$	$F_{4\text{-}2} = 0.355$
$F_{1\text{-}3} = 0.263$	$F_{2\text{-}3} = 0.574$	$F_{3\text{-}3} = 0$	$F_{4\text{-}3} = 0.071$
$F_{1\text{-}4} = 0.656$	$F_{2\text{-}4} = 0.355$	$F_{3\text{-}4} = 0.081$	$F_{4\text{-}4} = 0$

B.2.2: Calculating the Four Surface Radiation Model

The first step of the energy balance calculation is to determine the radiation heat transfer components of the blind and window. The Bevans and Dunkel technique (Wieblet 1966) is used on the four surface model developed in section 4.2.1. Because all 4 surfaces are treated as opaque, $\rho_i = 1 - \varepsilon_i$. To start the iteration an initial guess for j_i is required, so the blackbody emissive power, e_i is chosen. It is calculated from equation (4.9):

$$e_i = \sigma T_i^4$$

$$e_1 = \sigma T_1^4 = 5.67 \times 10^{-8} \frac{W}{m^2 K^4} \cdot (298K)^4 = 447.14 \frac{W}{m^2}$$

$$e_2 = 5.67 \times 10^{-8} \frac{W}{m^2 K^4} \cdot (305K)^4 = 490.66 \frac{W}{m^2}$$

$$e_3 = 5.67 \times 10^{-8} \frac{W}{m^2 K^4} \cdot (297K)^4 = 441.17 \frac{W}{m^2}$$

$$e_4 = 5.67 \times 10^{-8} \frac{W}{m^2 K^4} \cdot (305K)^4 = 490.66 \frac{W}{m^2}$$

The first iteration starts by calculating the updated radiosity of surface 1, j_1, which requires determining $j_k F_{i\text{-}k}$ for surfaces 2, 3 and 4.

$$\text{Surface 2:} \quad j_2 F_{1-2} = 490.66 \frac{W}{m^2} \cdot 0.081 = 39.74 \frac{W}{m^2}$$

$$\text{Surface 3:} \quad j_3 F_{1-3} = 441.17 \frac{W}{m^2} \cdot 0.263 = 116.03 \frac{W}{m^2}$$

$$\text{Surface 4:} \quad j_4 F_{1-4} = 490.66 \frac{W}{m^2} \cdot 0.656 = 321.87 \frac{W}{m^2}$$

The sum is:

$$\sum_{k=1}^{3} j_k F_{1-k} = 39.74\frac{W}{m^2} + 116.03\frac{W}{m^2} + 321.87\frac{W}{m^2} = 477.64\frac{W}{m^2}$$

This is multiplied by the reflectivity, which gives the result for the right hand term of equation (4.8).

$$\rho_1\left(\sum_{k=1}^{3} j_k F_{1-k}\right) = 0.19\left(477.64\frac{W}{m^2}\right) = 90.75\frac{W}{m^2}$$

The left hand term of equation (4.8) is:

$$\varepsilon_1 e_1 = 0.81 \cdot 447.14\frac{W}{m^2} = 362.18\frac{W}{m^2}$$

These two are then combined to calculate the updated radiosity (Eq. (4.8)):

$$j_1 = \varepsilon_1 e_1 + \rho_1\left(\sum_{k=1}^{3} j_k F_{1-k}\right) = 362.18\frac{W}{m^2} + 90.75\frac{W}{m^2} = 452.93\frac{W}{m^2}$$

This is repeated for the other 3 surfaces to obtain updated radiosities for all 4 surfaces to complete the first iteration. Table B.3 shows the iteration process for calculating the radiosities. The first column indicates the view factors as well as the formulas to be calculated to determine the updated radiosity. The iteration continues until the updated radiosity is equal to the old radiosity. The results are the updated radiosities:

$j_1 = 452.18\ W/m^2$

$j_2 = 484.38\ W/m^2$

$j_3 = 441.17\ W/m^2$

$j_4 = 485.37\ W/m^2$

The irradiation is calculated from the radiosities using the second term of equation (4.7b):

$$G_1 = \sum_{k=1}^{4} A_1 j_k F_{1-k} = A_1 j_1 F_{1-1} + A_1 j_2 F_{1-2} + A_1 j_3 F_{1-3} + A_1 j_4 F_{1-4}$$

$$G_1 = 0.0222m^2 \cdot 452.18\frac{W}{m^2} \cdot 0 + 0.0222m^2 \cdot 484.38\frac{W}{m^2} \cdot 0.081 +$$

$$0.0222m^2 \cdot 441.17\frac{W}{m^2} \cdot 0.263 + 0.0222m^2 \cdot 485.37\frac{W}{m^2} \cdot 0.656$$

$$G_1 = 10.52W$$

$$G_2 = 11.62W$$

$$G_3 = 10.57W$$

TABLE B.2: Iterative calculation of the radiosities for the radiation model.

NODE PAIR		**ITERATION 1**		**ITERATION 2**		**CONVERGED SOLUTION**	
i-k	j_k	j_k	j_kF_{i-k}	j_kF_{i-k}	F_{i-k}	j_kF_{i-k}	F_{i-k}
1-2	0.081	490.66	39.74	484.75	39.26	484.38	39.23
1-3	0.263	441.17	116.03	441.17	116.03	441.17	116.03
1-4	0.656	490.66	321.87	485.47	318.47	485.37	318.40
$\sum j_kF_{1-k}$			477.64		473.76		473.66
$\rho_1(\sum j_kF_{1-k})$			90.75		90.01		90.00
$\varepsilon_1 e_1$			362.18		362.18		362.18
j_1			452.93		452.19		452.18
2-1	0.071	452.93	32.16	452.19	32.11	452.18	32.10
2-3	0.574	441.17	253.23	441.17	253.23	441.17	253.23
2-4	0.355	490.66	174.18	485.47	172.34	485.37	172.31
$\sum j_kF_{3-k}$			459.57		457.68		457.64
$\rho_2(\sum j_kF_{3-k})$			87.32		86.96		86.95
$\varepsilon_2 e_2$			397.43		397.43		397.43
j_2			484.75		484.39		484.38
3-1	0.263	452.93	119.12	452.19	118.93	452.18	118.92
3-2	0.656	484.75	318.00	484.39	317.76	484.38	317.75
3-4	0.081	490.66	39.74	485.47	39.32	485.37	39.31
$\sum j_kF_{3-k}$			476.86		476.01		475.98
$\rho_3(\sum j_kF_{3-k})$			0.00		0.00		0.00
$\varepsilon_3 e_3$			441.17		441.17		441.17
j_3			441.17		441.17		441.17
4-1	0.574	452.93	259.98	452.19	259.56	452.18	259.55
4-2	0.355	484.75	172.09	484.39	171.96	484.38	171.95
4-3	0.071	441.17	31.32	441.17	31.32	441.17	31.32
$\sum j_kF_{4-k}$			463.39		462.84		462.82
$\rho_4(\sum j_kF_{4-k})$			88.04		87.94		87.94
$\varepsilon_4 e_4$			397.43		397.43		397.43
j_4			485.47		485.37		485.37

$$G_4 = 11.76\,\mathrm{W}$$

And finally, the radiation heat transfer rate of each surface is determined from equation (4.7a):

$$q_{rad,i} = j_i A_i - G_i$$

$$q_{rad,1} = 452.18\frac{\mathrm{W}}{\mathrm{m}^2}\cdot 0.0222\mathrm{m}\cdot 1\mathrm{m} - 10.52\mathrm{W} = -0.482\mathrm{W}$$

$$q_{rad,2} = 0.683\mathrm{W}$$

$$q_{rad,3} = -0.776\mathrm{W}$$

$$q_{rad,4} = 0.568\mathrm{W}$$

The radiation of the blind is the sum of surfaces 2 and 4 and the radiation of the window is surface 1. Thus, $q_{rad,b}$ is 1.251 W and $q_{rad,w}$ is -0.482 W with an area of one pitch by a unit length.

B.2.3: Calculating the Channel Convective Heat Transfer Rates

The next step is to calculate the convective heat transfer rate. In this case, as per the initial guess, $T_b = 305$ K and $T_w = 298$ K. Thus case (ii) applies: the hot surface is the blinds and the cold surface is the window (i.e. $T_H = T_b$ and $T_C = T_w$). The various temperature differences are:

From equation (1.10):

$$\overline{\Delta T} = \frac{T_H + T_C}{2} - T_\infty = \frac{T_b + T_w}{2} - T_\infty = \frac{305\mathrm{K} + 298\mathrm{K}}{2} - 297\mathrm{K} = 4.5\mathrm{K}$$

From equation (3.3):

$$\Delta T_{walls} = T_H - T_C = T_b - T_w = 305\mathrm{K} - 298\mathrm{K} = 7.0\mathrm{K}$$

From equation (1.4):

$$\Delta T_{max} = T_H - T_\infty = T_b - T_\infty = 305\mathrm{K} - 297\mathrm{K} = 8.0\mathrm{K}$$

and from equation (1.9):

$$T_R^* = \frac{T_C - T_\infty}{T_H - T_\infty} = \frac{T_w - T_\infty}{T_b - T_\infty} = \frac{298\mathrm{K} - 297\mathrm{K}}{305\mathrm{K} - 297\mathrm{K}} = 0.125$$

The modified Rayleigh number based on the effective channel width is required for the channel approximation. This is determined from equation (1.12):

$$\mathrm{Ra}^*_{\overline{\Delta T}} = \mathrm{Gr}_{\overline{\Delta T}}\,\mathrm{Pr}\frac{b}{L} = \frac{g\cdot\beta\cdot\overline{\Delta T}\cdot b_{\mathrm{eff}}^3}{\nu_f^2}\mathrm{Pr}\frac{b}{L}$$

$$\mathrm{Ra}^*_{\overline{\Delta T}} = \frac{9.81\frac{\mathrm{m}}{\mathrm{s}^2}\cdot 3.33\times10^{-3}\frac{1}{\mathrm{K}}\cdot 4.5\mathrm{K}\cdot\left(6.427\times10^{-3}\mathrm{m}\right)^3}{\left(1.59\times10^{-5}\frac{\mathrm{m}^2}{\mathrm{s}}\right)^2}0.716\frac{6.427\times10^{-3}\mathrm{m}}{0.3796\mathrm{m}}$$

$$\mathrm{Ra}^*_{\overline{\Delta T}} = 1.871$$

With the modified Rayleigh number, the average Nusselt numbers can be determined for the window and blind. The channel correlations developed in chapter 3 are used to determine the hot wall average Nusselt number for the blind and the cold wall average Nusselt number for the window. The hot wall average Nusselt number requires the calculation of the weighting factor A and the effective temperature difference ΔT_{eff}.

The weighting factor is from equation (3.12):

$$A = \frac{38.583}{\left(\mathrm{Ra}^*_{\overline{\Delta T}}\cdot\frac{\Delta T_{\max}}{\overline{\Delta T}}\right)^{1.128}+38.583} = \frac{38.583}{\left(1.871\cdot\frac{8.0\mathrm{K}}{4.5\mathrm{K}}\right)^{1.128}+38.583} = 0.909$$

and the effective temperature difference is from equation (3.11):

$$\Delta T_{\mathrm{eff}} = A\cdot\Delta T_{\mathrm{walls}} + (1-A)\cdot\Delta T_{\max} = 0.909\cdot 7.0\mathrm{K} + (1-0.909)\cdot 8.0\mathrm{K} = 7.091\mathrm{K}$$

The hot wall average Nusselt number is determined from equation (3.16):

$$\overline{\mathrm{Nu}}_{H,\Delta T_{\mathrm{eff}}} = \left(1+\left(0.618\cdot\left(\mathrm{Ra}^*_{\overline{\Delta T}}\right)^{0.25}\right)^{3.011}\right)^{\frac{1}{3.011}} = \left(1+\left(0.618\cdot(1.871)^{0.25}\right)^{3.011}\right)^{\frac{1}{3.011}}$$

$$\overline{\mathrm{Nu}}_{H,\Delta T_{\mathrm{eff}}} = 1.112$$

The average hot wall Nusselt number is based on ΔT_{eff}, but to ease further calculations this will be converted to be based on $\overline{\Delta T}$. A conversion is calculated:

$$\overline{\mathrm{Nu}}_{H,\overline{\Delta T}} = \overline{\mathrm{Nu}}_{H,\Delta T_{\mathrm{eff}}}\cdot\left(\frac{\Delta T_{\mathrm{eff}}}{\overline{\Delta T}}\right) = 1.112\cdot\left(\frac{7.091\mathrm{K}}{4.5\mathrm{K}}\right) = 1.752$$

Since case (ii) applies, the hot wall average Nusselt number is used in equation (4.10):

$$h_{b,ch} = \frac{\overline{Nu}_{H,\overline{\Delta T}} \cdot k_f}{b} = \frac{1.752 \cdot 0.026 \frac{W}{m \cdot K}}{6.427 \times 10^{-3} m} = 7.088 \frac{W}{m^2 \cdot K}$$

The overall channel average Nusselt number from Raithby and Hollands (1998) is required to calculate the cold wall average Nusselt number. The fully developed flow average Nusselt number from Aung (1972) is determined from equation (1.11):

$$\overline{Nu}_{fd} = \frac{4 \cdot T_R^{*2} + 7 \cdot T_R^* + 4}{90 \cdot \left(1 + T_R^*\right)^2} Ra^* = \frac{4 \cdot 0.125^2 + 7 \cdot 0.125 + 4}{90 \cdot (1 + 0.125)^2} 1.871 = 0.0801$$

The overall channel average Nusselt number is calculated from equation (1.16):

$$\overline{Nu}_{O,\overline{\Delta T}} = \left(\left(\overline{Nu}_{fd}\right)^{-1.9} + \left(0.618 \cdot Ra_{\overline{\Delta T}}^{*\ 0.25}\right)^{-1.9}\right)^{\frac{1}{-1.9}}$$

$$\overline{Nu}_{O,\overline{\Delta T}} = \left((0.0801)^{-1.9} + \left(0.618 \cdot 1.871^{0.25}\right)^{-1.9}\right)^{\frac{1}{-1.9}}$$

$$\overline{Nu}_{O,\overline{\Delta T}} = 0.0795$$

Equation (3.17) is used to calculate the cold wall average Nusselt number:

$$\overline{Nu}_{C,\overline{\Delta T}} = 2 \cdot \overline{Nu}_{O,\overline{\Delta T}} - \overline{Nu}_{H,\overline{\Delta T}} = 2 \cdot 0.080 - 1.752 = -1.592$$

and the heat transfer coefficient, $h_{w,ch}$ is determined from equation (4.11) as case (ii) applies:

$$h_{w,ch} = \frac{\overline{Nu}_{C,\overline{\Delta T}} \cdot k_f}{b_{eff}} = \frac{-1.592 \cdot 0.026 \frac{W}{m \cdot K}}{6.427 \times 10^{-3} m} = -6.440 \frac{W}{m^2 \cdot K}$$

The heat transfer rate is calculated from equation (4.12) leaving the blind temperature as an unknown and using a single pitch by a unit length as the area of the blind slat:

$$q_{conv,ch} = h \cdot A_b \cdot \Delta T = h_{b,ch} \cdot ps \cdot \overline{\Delta T} = h_{b,ch} \cdot ps \cdot \left(\frac{T_w + T_b}{2} - T_\infty\right)$$

$$q_{conv,ch} = 7.088 \frac{W}{m^2 \cdot K} \cdot 0.0222 m^2 \cdot \left(\frac{298K + T_b}{2} - 297K\right)$$

$$q_{conv,ch} = -23.29 W + 0.079 \frac{W}{K} \cdot T_b$$

B.2.4 Calculating the Flat Plate Convective Heat Transfer

The Rayleigh number based on length is calculated for the flat plate average Nusselt number using equation (4.14) and (4.15):

$$Ra_L = Gr_L\,Pr = \frac{g\cdot\beta\cdot\left(T_b - T_\infty\right)\cdot L^3}{{\nu_f}^2}Pr$$

$$Ra_L = \frac{9.81\frac{m}{s^2}\cdot 3.33\times10^{-3}\frac{1}{K}\cdot\left(305K - 297K\right)\cdot\left(0.3796m\right)^3}{\left(1.59\times10^{-5}\frac{m^2}{s}\right)^2}0.716 = 4.05\times10^7$$

The flat plate Nusselt number is from Churchill and Chu (1975) using equation (4.13):

$$\overline{Nu}_{fp} = 0.68 + \frac{0.67\cdot {Ra_L}^{\frac{1}{4}}}{\left(1+\left(\frac{0.492}{Pr}\right)^{\frac{9}{16}}\right)^{\frac{4}{9}}} = 0.68 + \frac{0.67\cdot\left(4.05\times10^8\right)^{\frac{1}{4}}}{\left(1+\left(\frac{0.492}{0.707}\right)^{\frac{9}{16}}\right)^{\frac{4}{9}}} = 73.60$$

The convection coefficient is also determined from equation (4.13):

$$h_{b,fp} = \frac{\overline{Nu}_{fp}\cdot k_f}{L} = \frac{73.60\cdot 0.026\frac{W}{m\cdot K}}{0.3796m} = 5.041\frac{W}{m^2\cdot K}$$

Equation (4.16) is the used to calculate the heat transfer rate, again leaving the blind temperature as an unknown and using the area of a single pitch by a unit length:

$$q_{conv,fp} = h\cdot A\cdot\Delta T = h_{b,fp}\cdot ps\cdot\left(T_b - T_\infty\right) = 5.041\frac{W}{m^2\cdot K}\cdot 0.0222m^2\cdot\left(T_b - 297K\right)$$

$$q_{conv,fp} = -33.24W + 0.11\cdot T_b W$$

B.2.5 Calculating the Correction Functions

The correction functions, F_1 and F_2 are calculated with C_1 and C_2 being determined from calibration of the simplified model with multiple data sets (Chapter 5). The correction functions are determined from equations (4.17) and (4.18):

$$F_1 = C_1\cdot\left(1+\cos(2\cdot\phi)\right)+1 = 0.28\cdot\left(1+\cos(2\cdot45°)\right)+1 = 1.28$$

$$F_2 = C_2\cdot\left(1+\cos(2\cdot\phi)\right)+1 = 0.10\cdot\left(1+\cos(2\cdot45°)\right)+1 = 1.10$$

The corrective functions show that both the channel and flat plate convective heat transfer coefficients need to be increased to obtain more accurate results. This is due to the interaction of the blind slats on the heat flow in the system.

B.2.6 Calculating the Energy Balance

With the heat transfer rates determined, the energy balance on the blind can be calculated. Since this is an iterative process, the purpose of this energy balance is to determine an updated T_b and compare it with the initial guess. Substituting the calculated heat transfers into the energy balance of equation (4.3) and solving for T_b:

$$q_{solar} = F_1 \cdot q_{conv,ch} + F_2 \cdot q_{conv,fp} + q_{rad,b}$$

$$3.81\mathrm{W} = 1.28 \cdot \left(-23.29\mathrm{W} + 0.079 \frac{\mathrm{W}}{\mathrm{K}} \cdot T_b \right) + 1.10 \cdot \left(-33.24\mathrm{W} + 0.11 \frac{\mathrm{W}}{\mathrm{K}} \cdot T_b \right) + 1.251\mathrm{W}$$

Solving for T_b gives:

$$T_b = 326.52\mathrm{K}$$

This updated blind temperature is then used to recalculate the heat transfer rates starting from section A.2.2, which would be the start of iteration 2, as shown in the flowchart in Figure 4.7. This iteration continues until the updated blind temperature is equal to the old T_b. For this case, T_b equals 307.72 K when the iteration is complete. This produces a $\overline{\Delta T}$ of 5.86 K. The radiation of the blind and window surfaces are: $q_{rad,b}$ = 1.724 W and $q_{rad,w}$ = -0.685 W. The heat transfer coefficient of the window, h_w = -6.855 W/m^{2}K. These are the only values of interest for comparison purposes in the next section.

B.3 Comparing the Results

For comparison, the convective and radiative heat fluxes of the window are required, which are calculated from equations (4.19) and (4.20):

$$q''_{conv,w} = h_w \cdot \overline{\Delta T} = -6.855 \cdot 5.86 = -40.17 \frac{\mathrm{W}}{\mathrm{m}^2}$$

$$q''_{rad,w} = \frac{q_{rad,w} \cdot B}{L} = \frac{-0.685 \cdot 17}{0.3796} = -30.68 \frac{\mathrm{W}}{\mathrm{m}^2}$$

These heat fluxes are then used to compare with the experimentally obtained heat fluxes of Collins et al. (2002b). The comparisons are shown in Table A.4 for the present case that was solved here and the experimental results from Collins et al. (2002b). The error is calculated by equation (5.3a) and (5.3b):

$$(\mathrm{error})_{\mathrm{conv}} = \frac{\left(q''_{\mathrm{conv,w}}\right)_{\mathrm{model}} - \left(q''_{\mathrm{conv,w}}\right)_{\mathrm{exp}}}{\left(q''_{\mathrm{conv,w}}\right)_{\mathrm{exp}}} = \frac{-40.17 - -20.6}{-20.6} = 0.9500 = 95.00\%$$

$$(\mathrm{error})_{\mathrm{rad}} = \frac{\left(q''_{\mathrm{rad,w}}\right)_{\mathrm{model}} - \left(q''_{\mathrm{rad,w}}\right)_{\mathrm{exp}}}{\left(q''_{\mathrm{rad,w}}\right)_{\mathrm{exp}}} = \frac{-30.68 - -28.24}{-28.24} = 0.0864 = 8.64\%$$

The table and the calculations show that the convective heat flux has an error of about 95% and the radiative heat flux has much less error at about 9%. As discussed in Section 5.4, the heat transfer into the room was calculated with equation (5.4) for comparison:

$$\left(q''_{\mathrm{room}}\right)_{\mathrm{model}} = q''_{\mathrm{conv,w}} + q''_{\mathrm{rad,w}} + q''_{\mathrm{solar}} = -40.17 + -30.68 + 150\cdot = 79.15\mathrm{W}$$

The experimental q''_{room} is also calculated with equation (5.4), except using the experimental values of the heat fluxes:

$$\left(q''_{\mathrm{room}}\right)_{\mathrm{exp}} = q''_{\mathrm{conv,w}} + q''_{\mathrm{rad,w}} + q''_{\mathrm{solar}} = -20.6 + -28.24 + 150 = 101.16\mathrm{W}$$

This error of the heat flux into the room is determined by equation (5.6):

$$(\mathrm{error})_{\mathrm{room}} = \frac{\left(q''_{\mathrm{room}}\right)_{\mathrm{model}} - \left(q''_{\mathrm{room}}\right)_{\mathrm{exp}}}{\left(q''_{\mathrm{room}}\right)_{\mathrm{exp}}} = \frac{79.15 - 101.16}{101.16} = -0.2176 = -21.76\%$$

The comparison of the models heat flux into the room versus the experimental heat flux of the room produces an error of 21.76%.

TABLE B.3: Comparison of Collins et al. (2002b) and model sample calculations with $\varepsilon_p = 0.81$, $\varepsilon_b = 0.81$, $q''_{solar} = 150\ W/m^2$, $T_w = 298\ K$, and $T_\infty = 297\ K$.

SLAT ANGLE	**BLIND-TO-WINDOW SPACING**	**COLLINS ET AL. (2002B)**		**CURRENT STUDY**		**ERROR**		**COLLINS ET AL. (2002B)**	**CURRENT STUDY**	**ERROR**
ϕ	**n (mm)**	**$q''_{conv,w}$ (W/m^2)**	**$q''_{rad,w}$ (W/m^2)**	**$q''_{conv,w}$ (W/m^2)**	**$q''_{rad,w}$ (W/m^2)**	**Conv (%)**	**Rad (%)**	**q''_{room} (W)**	**q''_{room} (W)**	**ROOM (%)**
45°	15.4	-20.6	-28.24	-40.17	-30.68	95.00	8.64	101.16	79.15	-21.76

APPENDIX C

Simplified Model Computer Code

C.1 Simplified Model Computer Code Using Matlab (2004)

```
%Geometry
x=20;   %# of data sets
y=3;   %# of data points per data set

phi(1,1,1)=90*pi/180;
phi(1,2,1)=90*pi/180;
phi(1,3,1)=90*pi/180;

for i = 2:x
   phi(i,1,1)=-45*pi/180;
   phi(i,2,1)=0*pi/180;
   phi(i,3,1)=45*pi/180;
end

l=0.3796; %length of plate
ps=0.0222; %pitch of slats
w=0.0254; %width of slats
rc=0.0523;
t=rc*(1-cos(w/(2*rc)));

N=-0.12;
A1=0.14;
A2=0.05;

b(1,1,1)=0.017+N*w/2*cos(phi(1,1,1));
b(1,2,1)=0.0145+N*w/2*cos(phi(1,2,1));
b(1,3,1)=0.013+N*w/2*cos(phi(1,3,1));

for i = 2:7
   b(i,1,1)=0.02-w/2*cos(phi(i,1,1))+t*sin(phi(i,1,1))+N*w/2*cos(phi(i,1,1));
   b(i,2,1)=0.02-w/2*cos(phi(i,2,1))+N*w/2*cos(phi(i,2,1));
```

```
  b(i,3,1)=0.02-w/2*cos(phi(i,3,1))+t*sin(phi(i,3,1))+N*w/2*cos(phi(i,3,1));
end

for i = 8:13
  b(i,1,1)=0.03-w/2*cos(phi(i,1,1))+t*sin(phi(i,1,1))+N*w/2*cos(phi(i,1,1));
  b(i,2,1)=0.03-w/2*cos(phi(i,2,1))+N*w/2*cos(phi(i,2,1));
  b(i,3,1)=0.03-w/2*cos(phi(i,3,1))+t*sin(phi(i,3,1))+N*w/2*cos(phi(i,3,1));
end

for i = 14:19
  b(i,1,1)=0.04-w/2*cos(phi(i,1,1))+t*sin(phi(i,1,1))+N*w/2*cos(phi(i,1,1));
  b(i,2,1)=0.04-w/2*cos(phi(i,2,1))+N*w/2*cos(phi(i,2,1));
  b(i,3,1)=0.04-w/2*cos(phi(i,3,1))+t*sin(phi(i,3,1))+N*w/2*cos(phi(i,3,1));
end

b(20,1,1)=0.0154-w/2*cos(phi(i,1,1))+t*sin(phi(i,1,1))+N*w/2*cos(phi(i,1,1));
b(20,2,1)=0.02-w/2*cos(phi(i,2,1))+N*w/2*cos(phi(i,2,1));
b(20,3,1)=0.0154-w/2*cos(phi(i,3,1))+t*sin(phi(i,3,1))+N*w/2*cos(phi(i,3,1));

%Experimental Results
%Plate & Blind Properties
kp=0.026; %thermal diffusivity
Tp(1,1,1)=316.5;
eb(1,1,1)=0.81;
ep(1,1,1)=0.81; %emissivity
qint(1,1,1)=0;
qconv(1,1,1)=3.67*(316.5-297);
qr(1,1,1)=78.3177;
qconv(1,2,1)=3.79*(316.5-297);
qr(1,2,1)=80.1202;
qconv(1,3,1)=3.64*(316.5-297);
qr(1,3,1)=83.1553;

Tp(2,1,1)=273+24;
eb(2,1,1)=0.3;
ep(2,1,1)=0.3;
qint(2,1,1)=25;
```

```
qconv(2,1,1)=-7.70;
qr(2,1,1)=-2.77;
qconv(2,2,1)=-8.71;
qr(2,2,1)=-2.17;
qconv(2,3,1)=-6.47;
qr(2,3,1)=-2.60;

Tp(3,1,1)=273+24;
eb(3,1,1)=0.6;
ep(3,1,1)=0.57;
qint(3,1,1)=75;
qconv(3,1,1)=-17.13;
qr(3,1,1)=-16.13;
qconv(3,2,1)=-19.77;
qr(3,2,1)=-13.96;
qconv(3,3,1)=-13.42;
qr(3,3,1)=-14.94;

Tp(4,1,1)=273+24;
eb(4,1,1)=0.9;
ep(4,1,1)=0.84;
qint(4,1,1)=125;
qconv(4,1,1)=-23.52;
qr(4,1,1)=-39.90;
qconv(4,2,1)=-28.46;
qr(4,2,1)=-36.01;
qconv(4,3,1)=-17.94;
qr(4,3,1)=-37.38;

Tp(5,1,1)=273+38;
eb(5,1,1)=0.3;
ep(5,1,1)=0.3;
qint(5,1,1)=75;
qconv(5,1,1)=24.74;
qr(5,1,1)=15.49;
qconv(5,2,1)=17.52;
qr(5,2,1)=17.84;
```

```
qconv(5,3,1)=29.86;
qr(5,3,1)=16.85;

Tp(6,1,1)=273+38;
eb(6,1,1)=0.6;
ep(6,1,1)=0.57;
qint(6,1,1)=125;
qconv(6,1,1)=17.97;
qr(6,1,1)=15.82;
qconv(6,2,1)=8.61;
qr(6,2,1)=20.66;
qconv(6,3,1)=25.04;
qr(6,3,1)=19.81;

Tp(7,1,1)=273+38;
eb(7,1,1)=0.9;
ep(7,1,1)=0.84;
qint(7,1,1)=25;
qconv(7,1,1)=31.10;
qr(7,1,1)=49.23;
qconv(7,2,1)=27.31;
qr(7,2,1)=51.74;
qconv(7,3,1)=34.33;
qr(7,3,1)=52.26;

Tp(8,1,1)=273+24;
eb(8,1,1)=0.3;
ep(8,1,1)=0.57;
qint(8,1,1)=125;
qconv(8,1,1)=-14.14;
qr(8,1,1)=-14.28;
qconv(8,2,1)=-16.23;
qr(8,2,1)=-14.23;
qconv(8,3,1)=-7.00;
qr(8,3,1)=-14.06;

Tp(9,1,1)=273+24;
```

```
eb(9,1,1)=0.6;
ep(9,1,1)=0.84;
qint(9,1,1)=25;
qconv(9,1,1)=-3.47;
qr(9,1,1)=-6.97;
qconv(9,2,1)=-3.88;
qr(9,2,1)=-6.65;
qconv(9,3,1)=-2.43;
qr(9,3,1)=-6.52;

Tp(10,1,1)=273+24;
eb(10,1,1)=0.9;
ep(10,1,1)=0.3;
qint(10,1,1)=75;
qconv(10,1,1)=-8.07;
qr(10,1,1)=-7.97;
qconv(10,2,1)=-8.97;
qr(10,2,1)=-7.51;
qconv(10,3,1)=-4.78;
qr(10,3,1)=-7.86;

Tp(11,1,1)=273+38;
eb(11,1,1)=0.3;
ep(11,1,1)=0.84;
qint(11,1,1)=25;
qconv(11,1,1)=39.20;
qr(11,1,1)=46.78;
qconv(11,2,1)=38.72;
qr(11,2,1)=56.05;
qconv(11,3,1)=40.26;
qr(11,3,1)=46.19;

Tp(12,1,1)=273+38;
eb(12,1,1)=0.6;
ep(12,1,1)=0.3;
qint(12,1,1)=75;
qconv(12,1,1)=37.34;
```

```
qr(12,1,1)=17.78;
qconv(12,2,1)=36.57;
qr(12,2,1)=19.13;
qconv(12,3,1)=39.44;
qr(12,3,1)=17.70;

Tp(13,1,1)=273+38;
eb(13,1,1)=0.9;
ep(13,1,1)=0.57;
qint(13,1,1)=125;
qconv(13,1,1)=34.92;
qr(13,1,1)=24.26;
qconv(13,2,1)=33.80;
qr(13,2,1)=25.89;
qconv(13,3,1)=38.59;
qr(13,3,1)=23.77;

Tp(14,1,1)=273+24;
eb(14,1,1)=0.3;
ep(14,1,1)=0.3;
qint(14,1,1)=125;
qconv(14,1,1)=-8.88;
qr(14,1,1)=-6.89;
qconv(14,2,1)=-8.91;
qr(14,2,1)=-6.65;
qconv(14,3,1)=-1.56;
qr(14,3,1)=-7.74;

Tp(15,1,1)=273+24;
eb(15,1,1)=0.6;
ep(15,1,1)=0.57;
qint(15,1,1)=25;
qconv(15,1,1)=-2.13;
qr(15,1,1)=-4.21;
qconv(15,2,1)=-2.32;
qr(15,2,1)=-4.09;
qconv(15,3,1)=-1.06;
```

```
qr(15,3,1)=-4.32;

Tp(16,1,1)=273+24;
eb(16,1,1)=0.9;
ep(16,1,1)=0.84;
qint(16,1,1)=125;
qconv(16,1,1)=-7.08;
qr(16,1,1)=-26.98;
qconv(16,2,1)=-7.26;
qr(16,2,1)=-27.19;
qconv(16,3,1)=-1.58;
qr(16,3,1)=-29.75;

Tp(17,1,1)=273+38;
eb(17,1,1)=0.3;
ep(17,1,1)=0.57;
qint(17,1,1)=75;
qconv(17,1,1)=40.71;
qr(17,1,1)=32.47;
qconv(17,2,1)=40.01;
qr(17,2,1)=37.13;
qconv(17,3,1)=42.19;
qr(17,3,1)=31.39;

Tp(18,1,1)=273+38;
eb(18,1,1)=0.6;
ep(18,1,1)=0.84;
qint(18,1,1)=125;
qconv(18,1,1)=39.99;
qr(18,1,1)=37.60;
qconv(18,2,1)=38.94;
qr(18,2,1)=42.19;
qconv(18,3,1)=42.41;
qr(18,3,1)=34.53;

Tp(19,1,1)=273+38;
eb(19,1,1)=0.9;
```

```
ep(19,1,1)=0.3;
qint(19,1,1)=25;
qconv(19,1,1)=41.58;
qr(19,1,1)=23.08;
qconv(19,2,1)=41.41;
qr(19,2,1)=23.53;
qconv(19,3,1)=42.01;
qr(19,3,1)=22.88;

Tp(20,1,1)=298;
eb(20,1,1)=0.81;
ep(20,1,1)=0.81;
qint(20,1,1)=150;
qconv(20,1,1)=-28.9;
qr(20,1,1)=-29.11;
qconv(20,2,1)=-25.1;
qr(20,2,1)=-33.16;
qconv(20,3,1)=-20.6;
qr(20,3,1)=-28.24;

for i = 1:x
   for j = 1:y
      Tb(i,j,1) = 305;
   end
end

%Ambient Properties
Tinf=297; %Ambient temperature
einf=1; %Emissivity
g=9.81; %gravity constant
Beta=0.0033; %Beta
vf=0.0000159; %kinematic viscosity
cp=1006.3; %Specific heat
rho=1.1656; %Density
kf=0.026; %Thermal diffusivity
sigma=5.67*10^-8; %stefan-boltxman constant
```

```
alpha=kf/(rho*cp); %Alpha
Pr=vf/alpha;

for i = 1:x
  for j = 1:y
    F(1,1,i,j)=0;
    F(2,1,i,j)=(w+ps-(ps^2+w^2-2*w*ps*cos(pi/2+phi(i,j,1)))^0.5)/(2*ps);
    F(3,1,i,j)=((ps^2+w^2-2*w*ps*cos(pi/2+phi(i,j,1)))^0.5+(ps^2+w^2-2*w*ps*cos(pi/2-
               phi(i,j,1)))^0.5-2*w)/(2*ps);
    F(4,1,i,j)=(w+ps-(ps^2+w^2-2*w*ps*cos(pi/2-phi(i,j,1)))^0.5)/(2*ps);
    F(1,2,i,j)=(w+ps-(ps^2+w^2-2*w*ps*cos(pi/2+phi(i,j,1)))^0.5)/(2*w);
    F(2,2,i,j)=0;
    F(3,2,i,j)=(w+ps-(ps^2+w^2-2*w*ps*cos(pi/2-phi(i,j,1)))^0.5)/(2*w);
    F(4,2,i,j)=((ps^2+w^2-2*w*ps*cos(pi/2+phi(i,j,1)))^0.5+(ps^2+w^2-2*w*ps*cos(pi/2-
               phi(i,j,1)))^0.5-2*ps)/(2*w);
    F(1,3,i,j)=F(3,1,i,j);
    F(2,3,i,j)=F(4,1,i,j);
    F(3,3,i,j)=F(1,1,i,j);
    F(4,3,i,j)=F(2,1,i,j);
    F(1,4,i,j)=F(3,2,i,j);
    F(2,4,i,j)=F(4,2,i,j);
    F(3,4,i,j)=F(1,2,i,j);
    F(4,4,i,j)=F(2,2,i,j);
  end

  e(1,1,1)=ep(i,1,1);
  e(2,1,1)=eb(i,1,1);
  e(3,1,1)=einf;
  e(4,1,1)=eb(i,1,1);

  p(1,1,1)=1-e(1,1,1);
  p(2,1,1)=1-e(2,1,1);
  p(3,1,1)=1-e(3,1,1);
  p(4,1,1)=1-e(4,1,1);

  Area(1,1,1)=ps;
  Area(2,1,1)=w;
```

```
 Area(3,1,1)=ps;
 Area(4,1,1)=w;

for j = 1:y
    Tbnew = 0;
    count = 0;
    cc=0;

    while count < 1000
        count = count+1;

        T(1,1,1)=Tp(i,1,1);
        T(2,1,1)=Tb(i,j,1);
        T(3,1,1)=Tinf;
        T(4,1,1)=Tb(i,j,1);

        %Radiation Analysis
        E(1,1,1)=sigma*T(1,1,1)^4;
        E(2,1,1)=sigma*T(2,1,1)^4;
        E(3,1,1)=sigma*T(3,1,1)^4;
        E(4,1,1)=sigma*T(4,1,1)^4;

        J(1,1,1)=E(1,1,1);
        J(2,1,1)=E(2,1,1);
        J(3,1,1)=E(3,1,1);
        J(4,1,1)=E(4,1,1);

        Jn=zeros(4,1,1);
        ccc=0;

        while Jn(1,1,1)~=J(1,1,1)
            ccc=ccc+1;
            Jn=J;
            for m = 1:4
                K=0;
                L=0;
                for n=1:4
```

```
      K=K+J(n,1,1)*F(n,m,i,j);
    end
    J(m,1,1)=e(m,1,1)*E(m,1,1)+p(m,1,1)*K;
    for n=1:4
      L=L+J(n,1,1)*F(n,m,i,j)*Area(m,1,1);
    end
    q(m,1,1)=J(m,1,1)*Area(m,1,1)-L;
  end
end

Tbar=(Tp(i,1,1)+Tb(i,j,1))/2-Tinf;

%Convection Model
if Tb(i,j,1) > Tp(i,1,1)
  Tmax=Tb(i,j,1)-Tinf;
  Twalls=Tb(i,j,1)-Tp(i,1,1);
  Tstar=(Tp(i,1,1)-Tinf)/(Tb(i,j,1)-Tinf);
  Ra(i,j,1)=g*Beta*(Tbar)*b(i,j,1)^4/(alpha*vf*l);
  RaL=g*Beta*(Tb(i,j,1)-Tinf)*l^3/(alpha*vf);
  A=38.583/((Ra(i,j,1)*Tmax/Tbar)^1.128+38.583);
  Teff=A*Twalls+(1-A)*Tmax;
  NuH=((1+(0.618*Ra(i,j,1)^0.25)^3.011)^(1/3.011))*Teff/Tbar;
  hb=NuH*kf/b(i,j,1);
  Nufd=(4*Tstar^2+7*Tstar+4)/(90*(1+Tstar)^2)*Ra(i,j,1);
  NuO=((Nufd^-1.9)+(0.618*Ra(i,j,1)^0.25)^-1.9)^(1/-1.9);
  NuC=2*NuO-NuH;
  hp=NuC*kf/b(i,j,1);
else
  Tmax=Tp(i,1,1)-Tinf;
  Twalls=Tp(i,1,1)-Tb(i,j,1);
  Tstar=(Tb(i,j,1)-Tinf)/(Tp(i,1,1)-Tinf);
  Ra(i,j,1)=g*Beta*(Tbar)*b(i,j,1)^4/(alpha*vf*l);
  RaL=g*Beta*(Tb(i,j,1)-Tinf)*l^3/(alpha*vf);
  A=38.583/((Ra(i,j,1)*Tmax/Tbar)^1.128+38.583);
  Teff=A*Twalls+(1-A)*Tmax;
  NuH=((1+(0.618*Ra(i,j,1)^0.25)^3.011)^(1/3.011))*Teff/Tbar;
  hp=NuH*kf/b(i,j,1);
```

```
            Nufd=(4*Tstar^2+7*Tstar+4)/(90*(1+Tstar)^2)*Ra(i,j,1);
            NuO=((Nufd^-1.9)+(0.618*Ra(i,j,1)^0.25)^-1.9)^(1/-1.9);
            NuC=2*NuO-NuH;
            hb=NuC*kf/b(i,j,1);
          end

          NuFP=0.68+(0.67*RaL^0.25)/(1+(0.492/Pr)^(9/16))^(4/9);
          hFP=NuFP*kf/l;
          F1=A1*(1+cos(2*phi(i,j,1)))+0.5;
          F2=A2*(1+cos(2*phi(i,j,1)))+0.5;
          qchan=hb*2*ps*(Tp(i,1,1)/2-Tinf)*F1;
          qFP=-hFP*2*ps*Tinf*F2;
          qinput=qint(i,1,1)*w;
          qrad=(q(2,1,1)+q(4,1,1));
          Tbnew=(qinput-qrad-qFP-qchan)/(((hb*2*ps*F1)/2)+hFP*2*ps*F2);
          Tb(i,j,1)=Tb(i,j,1)*0.95+0.05*Tbnew;
        end

        qc(i,j,1)=hp*(Tbar);
        qradp(i,j,1)=q(1,1,1)*17/l;
        qtotal(i,j,1)=qc(i,j,1)+qradp(i,j,1);
        qtotalexp(i,j,1)=qconv(i,j,1)+qr(i,j,1);
        error(i,j,1)=(qc(i,j,1)-qconv(i,j,1))/qconv(i,j,1);
        error(i,j,2)=(qradp(i,j,1)-qr(i,j,1))/qr(i,j,1);
        error(i,j,3)=(qtotalexp(i,j,1)-qtotal(i,j,1));
    end
end

errorroom=0;
errortotal = 0;
errorqtotal = 0;
for i = 1:x
    for j = 1:y
        for k = 1:2
            errortotal = error(i,j,k)^2+errortotal;
        end
        errorqtotal=error(i,j,3)^2+errorqtotal;
        qroom(i,j,1)=(qradp(i,j,1)+qc(i,j,1)+qint(i,1,1));
        qroomt(i,j,1)=(qr(i,j,1)+qconv(i,j,1)+qint(i,1,1));
        errorqroom(i,j,1)=(qroom(i,j,1)-qroomt(i,j,1))/qroomt(i,j,1);
        errorroom=errorroom+errorqroom(i,j,1)^2;
    end
end
```

Appendix D

Comparison of Current Model Results versus the Numerical Data of Collins (2001)

D.1 Introduction

Chapter 5 compares the predicted results of the simplified model with the experimental and numerical data of Machin (1998), Collins (2001), and Collins et al. (2002b). Sixty data sets were used in total to calibrate the simplified model and calculate the constants used in the simplified model. The comparison with the six experimental data sets is presented in Table 4.1 and Table 5.5 and the comparison with nine numerical data sets is presented in Tables 5.6, 5.7 and 5.8. The comparison between the predicted results of the simplified model and the additional 45 numerical data sets from Collins (2001) are presented in this Appendix.

D.2 Tables of Comparison between the Numerical Data and the Current Model

Table D.1: Comparison of the numerical results (Collins 2001) with the current model for $\varepsilon_w = 0.57$, $\varepsilon_b = 0.6$, $q''_{solar} = 75$ *W/m2*, $T_w = 297$ *K*, $T_\infty = 297$ *K, and* $L = 379.6$ *mm.*

SLAT ANGLE	BLIND-TO-WINDOW SPACING	COLLINS (2001)		CURRENT STUDY		ERROR		COLLINS (2001)	CURRENT STUDY	ERROR
ϕ	n (mm)	$q''_{conv,w}$ (W/m²)	$q''_{rad,w}$ (W/m²)	$q''_{conv,w}$ (W/m²)	$q''_{rad,w}$ (W/m²)	CONV (%)	RAD (%)	q''_{room} (W)	q''_{room} (W)	ROOM (%)
-45°	20.0	-17.13	-16.13	-19.21	-12.63	12.13	-21.73	41.74	43.17	3.42
0°	20.0	-19.77	-13.96	-25.43	-9.05	28.62	-35.14	41.27	40.52	-1.82
45°	20.0	-13.42	-14.94	-14.03	-13.04	4.51	-12.70	46.64	47.93	2.77

Table D.2: Comparison of the numerical results (Collins 2001) with the current model for $\varepsilon_w = 0.84$, $\varepsilon_b = 0.9$, $q''_{solar} = 125$ W/m^2, $T_w = 297$ *K*, $T_\infty = 297$ *K, and* $L = 379.6$ *mm.*

SLAT ANGLE	BLIND-TO-WINDOW SPACING	COLLINS (2001)		CURRENT STUDY		ERROR		COLLINS (2001)	CURRENT STUDY	ERROR
ϕ	n (mm)	$q''_{conv,w}$ (W/m²)	$q''_{rad,w}$ (W/m²)	$q''_{conv,w}$ (W/m²)	$q''_{rad,w}$ (W/m²)	CONV (%)	RAD (%)	q''_{room} (W)	q''_{room} (W)	ROOM (%)
-45°	20.0	-23.52	-39.90	-25.50	-32.10	8.42	-19.56	61.58	67.40	9.46
0°	20.0	-28.46	-36.01	-36.95	-24.34	29.84	-32.40	60.53	63.70	5.24
45°	20.0	-17.94	-37.38	-17.46	-32.90	-2.67	-11.99	69.68	74.64	7.12

Table D.3: Comparison of the numerical results (Collins 2001) with the current model for $\varepsilon_w = 0.3$, $\varepsilon_b = 0.3$, $q''_{solar} = 75\ W/m^2$, *Tw = 311 K,* $T_\infty = 297$ *K, and L = 379.6 mm.*

SLAT ANGLE	BLIND-TO-WINDOW SPACING	COLLINS (2001)		CURRENT STUDY		ERROR		COLLINS (2001)	CURRENT STUDY	ERROR
ϕ	n (mm)	$q''_{conv,w}$ (W/m^2)	$q''_{rad,w}$ (W/m^2)	$q''_{conv,w}$ (W/m^2)	$q''_{rad,w}$ (W/m^2)	CONV (%)	RAD (%)	q''_{room} (W)	q''_{room} (W)	ROOM (%)
-45°	20.0	24.74	15.49	33.05	15.61	33.57	0.79	115.23	123.66	7.31
0°	20.0	17.52	17.84	13.79	17.52	-21.27	-1.82	110.36	106.31	-3.67
45°	20.0	29.86	16.85	43.34	16.49	45.16	-2.13	121.71	134.83	10.78

Table D.4: Comparison of the numerical results (Collins 2001) with the current model for $\varepsilon_w = 0.57$, $\varepsilon_b = 0.6$, $q''_{solar} = 125\ W/m^2$, $T_w = 311$ *K,* $T_\infty = 297$ *K, and L = 379.6 mm.*

SLAT ANGLE	BLIND-TO-WINDOW SPACING	COLLINS (2001)		CURRENT STUDY		ERROR		COLLINS (2001)	CURRENT STUDY	ERROR
ϕ	n (mm)	$q''_{conv,w}$ (W/m^2)	$q''_{rad,w}$ (W/m^2)	$q''_{conv,w}$ (W/m^2)	$q''_{rad,w}$ (W/m^2)	CONV (%)	RAD (%)	q''_{room} (W)	q''_{room} (W)	ROOM (%)
-45°	20.0	17.97	15.82	27.22	17.62	51.46	11.38	158.79	169.84	6.96
0°	20.0	8.61	20.66	5.62	21.57	-34.78	4.42	154.27	152.19	-1.35
45°	20.0	25.04	19.81	40.54	19.56	61.88	-1.24	169.85	185.10	8.98

Table D.5: Comparison of the numerical results (Collins 2001) with the current model for $\varepsilon_w = 0.84$, $\varepsilon_b = 0.9$, $q''_{solar} = 25\ W/m^2$, $T_w = 311$ *K,* $T_\infty = 297$ *K, and L = 379.6 mm.*

SLAT ANGLE	BLIND-TO-WINDOW SPACING	COLLINS (2001)		CURRENT STUDY		ERROR		COLLINS (2001)	CURRENT STUDY	ERROR
ϕ	n (mm)	$q''_{conv,w}$ (W/m^2)	$q''_{rad,w}$ (W/m^2)	$q''_{conv,w}$ (W/m^2)	$q''_{rad,w}$ (W/m^2)	CONV (%)	RAD (%)	q''_{room} (W)	q''_{room} (W)	ROOM (%)
-45°	20.0	31.10	49.23	40.75	44.79	31.04	-9.02	105.33	110.54	4.95
0°	20.0	27.31	51.74	29.57	44.89	8.29	-13.24	104.05	99.46	-4.41
45°	20.0	34.33	2.26	46.35	48.42	35.00	-7.35	111.59	119.77	7.33

Table D.6: Comparison of the numerical results (Collins 2001) with the current model for $\varepsilon_w = 0.57$, $\varepsilon_b = 0.3$, $q''_{solar} = 125\ W/m^2$, $T_w = 297$ *K,* $T_\infty = 297$ *K, and L = 379.6 mm.*

SLAT ANGLE	BLIND-TO-WINDOW SPACING	COLLINS (2001)		CURRENT STUDY		ERROR		COLLINS (2001)	CURRENT STUDY	ERROR
ϕ	n (mm)	$q''_{conv,w}$ (W/m^2)	$q''_{rad,w}$ (W/m^2)	$q''_{conv,w}$ (W/m^2)	$q''_{rad,w}$ (W/m^2)	CONV (%)	RAD (%)	q''_{room} (W)	q''_{room} (W)	ROOM (%)
-45°	30.0	-14.14	-14.28	-2.69	-15.57	-80.98	9.01	96.58	106.74	10.52
0°	30.0	-16.23	-14.23	-5.79	-12.53	-64.32	-11.92	94.54	106.67	12.84
45°	30.0	-7.00	-14.06	-1.67	-15.60	-76.17	10.97	103.94	107.73	3.64

Table D.7: Comparison of the numerical results (Collins 2001) with the current model for $\varepsilon_w = 0.84$, $\varepsilon_b = 0.6$, $q''_{solar} = 25\ W/m^2$, $T_w = 297\ K$, $T_\infty = 297\ K$, *and* $L = 379.6\ mm$.

SLAT ANGLE	BLIND-TO-WINDOW SPACING	COLLINS (2001)		CURRENT STUDY		ERROR		COLLINS (2001)	CURRENT STUDY	ERROR
ϕ	n (mm)	$q''_{conv,w}$ (W/m²)	$q''_{rad,w}$ (W/m²)	$q''_{conv,w}$ (W/m²)	$q''_{rad,w}$ (W/m²)	CONV (%)	RAD (%)	q''_{room} (W)	q''_{room} (W)	ROOM (%)
-45°	30.0	-3.47	-6.97	-1.89	-6.76	-45.42	-3.03	14.56	16.35	12.28
0°	30.0	-3.88	-6.65	-3.15	-5.74	-18.69	-13.66	14.47	16.10	11.29
45°	30.0	-2.43	-6.52	-1.26	-6.79	-47.95	4.17	16.05	16.94	5.57

Table D.8: Comparison of the numerical results (Collins 2001) with the current model for $\varepsilon_w = 0.3$, $\varepsilon_b = 0.9$, $q''_{solar} = 75\ W/m^2$, $T_w = 297\ K$, $T_\infty = 297\ K$, *and* $L = 379.6\ mm$.

SLAT ANGLE	BLIND-TO-WINDOW SPACING	COLLINS (2001)		CURRENT STUDY		ERROR		COLLINS (2001)	CURRENT STUDY	ERROR
ϕ	n (mm)	$q''_{conv,w}$ (W/m²)	$q''_{rad,w}$ (W/m²)	$q''_{conv,w}$ (W/m²)	$q''_{rad,w}$ (W/m²)	CONV (%)	RAD (%)	q''_{room} (W)	q''_{room} (W)	ROOM (%)
-45°	30.0	-8.07	-7.97	-2.43	-8.58	-69.87	7.65	58.96	63.99	8.53
0°	30.0	-8.97	-7.51	-4.97	-6.97	-44.55	-7.20	58.52	63.06	7.75
45°	30.0	-4.78	-7.86	-1.51	-8.60	-68.40	9.46	62.36	64.89	4.05

Table D.9: Comparison of the numerical results (Collins 2001) with the current model for $\varepsilon_w = 0.84$, $\varepsilon_b = 0.3$, $q''_{solar} = 25\ W/m^2$, $T_w = 311\ K$, $T_\infty = 297\ K$, *and* $L = 379.6\ mm$.

SLAT ANGLE	BLIND-TO-WINDOW SPACING	COLLINS (2001)		CURRENT STUDY		ERROR		COLLINS (2001)	CURRENT STUDY	ERROR
ϕ	n (mm)	$q''_{conv,w}$ (W/m²)	$q''_{rad,w}$ (W/m²)	$q''_{conv,w}$ (W/m²)	$q''_{rad,w}$ (W/m²)	CONV (%)	RAD (%)	q''_{room} (W)	q''_{room} (W)	ROOM (%)
-45°	30.0	39.20	46.78	49.51	46.71	26.30	-0.15	110.98	121.22	9.23
0°	30.0	38.72	56.05	49.28	56.32	27.28	0.49	119.77	130.60	9.04
45°	30.0	40.26	46.19	49.48	46.84	22.89	1.41	111.45	121.32	8.85

Table D.10: Comparison of the numerical results (Collins 2001) with the current model for $\varepsilon_w = 0.57$, $\varepsilon_b = 0.9$, $q''_{solar} = 125\ W/m^2$, $T_w = 311\ K$, $T_\infty = 297\ K$, *and* $L = 379.6\ mm$.

SLAT ANGLE	BLIND-TO-WINDOW SPACING	COLLINS (2001)		CURRENT STUDY		ERROR		COLLINS (2001)	CURRENT STUDY	ERROR
ϕ	n (mm)	$q''_{conv,w}$ (W/m²)	$q''_{rad,w}$ (W/m²)	$q''_{conv,w}$ (W/m²)	$q''_{rad,w}$ (W/m²)	CONV (%)	RAD (%)	q''_{room} (W)	q''_{room} (W)	ROOM (%)
-45°	30.0	34.92	24.26	52.08	20.77	49.13	-14.38	184.18	197.85	7.42
0°	30.0	33.80	25.89	50.56	26.79	49.58	3.46	184.69	202.34	9.56
45°	30.0	38.59	23.77	52.51	20.84	36.07	-12.35	187.36	198.34	5.86

Table D.11: Comparison of the numerical results (Collins 2001) with the current model for $\varepsilon_w = 0.3$, $\varepsilon_b = 0.3$, $q''_{solar} = 125\ W/m^2$, $T_w = 297\ K$, $T_\infty = 297\ K$, and $L = 379.6\ mm$.

SLAT ANGLE	BLIND-TO-WINDWO SPACING	COLLINS (2001)		CURRENT STUDY		ERROR		COLLINS (2001)	CURRENT STUDY	ERROR
ϕ	n (mm)	$q''_{conv,w}$ (W/m^2)	$q''_{rad,w}$ (W/m^2)	$q''_{conv,w}$ (W/m^2)	$q''_{rad,w}$ (W/m^2)	CONV (%)	RAD (%)	q''_{room} (W)	q''_{room} (W)	ROOM (%)
-45°	40.0	-8.88	-6.89	-0.45	-9.26	-94.88	34.38	109.23	115.29	5.54
0°	40.0	-8.91	-6.65	-0.70	-7.12	-92.16	7.13	109.44	117.18	7.07
45°	40.0	-1.56	-7.74	-0.34	-9.26	-77.92	19.68	115.70	115.39	-0.26

Table D.12: Comparison of the numerical results (Collins 2001) with the current model for $\varepsilon_w = 0.57$, $\varepsilon_b = 0.6$, $q''_{solar} = 25\ W/m^2$, $T_w = 297\ K$, $T_\infty = 297\ K$, and $L = 379.6\ mm$.

SLAT ANGLE	BLIND-TO-WINDOW SPACING	COLLINS (2001)		CURRENT STUDY		ERROR		COLLINS (2001)	CURRENT STUDY	ERROR
ϕ	n (mm)	$q''_{conv,w}$ (W/m^2)	$q''_{rad,w}$ (W/m^2)	$q''_{conv,w}$ (W/m^2)	$q''_{rad,w}$ (W/m^2)	CONV (%)	RAD (%)	q''_{room} (W)	q''_{room} (W)	ROOM (%)
-45°	40.0	-2.13	-4.21	-0.33	-5.06	-84.65	20.19	18.66	19.61	5.11
0°	40.0	-2.32	-4.09	-0.54	-4.21	-76.90	3.02	18.59	20.25	8.93
45°	40.0	-1.06	-4.32	-0.24	-5.07	-77.53	17.25	19.62	19.70	0.39

Table D.13: Comparison of the numerical results (Collins 2001) with the current model for $\varepsilon_w = 0.57$, $\varepsilon_b = 0.3$, $q''_{solar} = 75\ W/m^2$, $T_w = 311\ K$, $T_\infty = 297\ K$, and $L = 379.6\ mm$.

SLAT ANGLE	BLIND-TO-WINDOW SPACING	COLLINS (2001)		CURRENT STUDY		ERROR		COLLINS (2001)	CURRENT STUDY	ERROR
ϕ	n (mm)	$q''_{conv,w}$ (W/m^2)	$q''_{rad,w}$ (W/m^2)	$q''_{conv,w}$ (W/m^2)	$q''_{rad,w}$ (W/m^2)	CONV (%)	RAD (%)	q''_{room} (W)	q''_{room} (W)	ROOM (%)
-45°	40.0	40.71	32.47	51.76	29.70	27.13	-8.52	148.18	156.46	5.59
0°	40.0	40.01	37.13	51.27	36.56	28.14	-1.55	152.14	162.82	7.02
45°	40.0	42.19	31.39	51.76	29.71	22.69	-5.36	148.58	156.47	5.31

Table D.14: Comparison of the numerical results (Collins 2001) with the current model for $\varepsilon_w = 0.84$, $\varepsilon_b = 0.6$, $q''_{solar} = 125\ W/m^2$, $T_w = 311\ K$, $T_\infty = 297\ K$, and $L = 379.6\ mm$.

SLAT ANGLE	BLIND-TO-WINDOW SPACING	COLLINS (2001)		CURRENT STUDY		ERROR		COLLINS (2001)	CURRENT STUDY	ERROR
ϕ	n (mm)	$q''_{conv,w}$ (W/m^2)	$q''_{rad,w}$ (W/m^2)	$q''_{conv,w}$ (W/m^2)	$q''_{rad,w}$ (W/m^2)	CONV (%)	RAD (%)	q''_{room} (W)	q''_{room} (W)	ROOM (%)
-45°	40.0	39.99	37.60	53.46	29.23	33.68	-22.27	202.59	207.69	2.52
0°	40.0	38.94	42.19	52.99	40.70	36.08	-3.53	206.13	218.69	6.09
45°	40.0	42.41	34.53	53.49	29.23	26.13	-15.35	201.94	207.72	2.86

Table D.15: Comparison of the numerical results (Collins 2001) with the current model for $\varepsilon_w = 0.3$, $\varepsilon_b = 0.9$, $q''_{solar} = 25\ W/m^2$, $T_w = 311\ K$, $T_\infty = 297\ K$, *and* $L = 379.6\ mm$.

SLAT ANGLE	**BLIND-TO-WINDOW SPACING**	**COLLINS (2001)**		**CURRENT STUDY**		**ERROR**		**COLLINS (2001)**	**CURRENT STUDY**	**ERROR**
ϕ	**n (mm)**	$q''_{conv,w}$ **(W/m²)**	$q''_{rad,w}$ **(W/m²)**	$q''_{conv,w}$ **(W/m²)**	$q''_{rad,w}$ **(W/m²)**	**CONV (%)**	**RAD (%)**	q''_{room} **(W)**	q''_{room} **(W)**	**ROOM (%)**
-45°	40.0	41.58	23.08	48.54	21.69	16.73	-6.05	89.66	95.22	6.20
0°	40.0	41.41	23.53	48.40	22.92	16.88	-2.58	89.94	96.32	7.10
45°	40.0	42.01	22.88	48.50	21.70	15.45	-5.18	89.89	95.19	5.90

Appendix E

Bidirectional Flow in an Asymmetrically, Isothermally Heated Vertical Channel

E.1 Introduction

For the purposes of this thesis, the complex fenestration system cases of interest involved unidirectional flow. A unidirectional flow occurs when the buoyancy driven flow is in one direction. In these cases, the fluid flows into the channel through the inlet and out of the channel through the outlet. This occurs if both channel walls are heated above or both cooled below the ambient. It is also of interest to study a bidirectional flow, in which the output of the buoyancy driven flow is in two opposite directions. Such a case would be when one channel wall is heated above the ambient temperature, but the other channel wall is cooled below the ambient temperature. This type of condition applies to a Venetian blind located on the indoor window surface on a sunny day in the wintertime. The blinds will be heated above the ambient temperature by solar irradiance and the indoor glazing surface will be cooled below the ambient temperature by the colder weather outside the building. This will cause a bidirectional flow in between the window surface and the Venetian blind as the hotter blind will draw the flow upwards, but the colder window surface will draw the flow downwards. This may cause instabilities where the two opposing flows interact with each other.

Although not specifically needed in the present study, some analytical and numerical work was performed on bidirectional flow in an asymmetrically, isothermally heated channel. The analytical work proves that when all asymmetrically heated cases are non-dimensionalized, they can be reduced to a simple range of temperature difference ratios. Some numerical results are produced using Grid 2 from Chapter 2 with multiple negative temperature difference ratios. Using negative temperature difference ratios produced the bidirectional flow of interest. No parametric study has been performed on the numerical solutions, but the results that were obtained show that further intensive study is required.

E.2 Analytical Study of the Temperature Difference Ratio Range

For a unidirectional flow in an asymmetrically, isothermally heated vertical channel, it has been shown by Aung et al. (1972) that $0 < T_R^* < 1$ is the range of temperature difference ratios that encompasses all possible asymmetrical cases. This is due to the fact that when the cold wall is the same temperature as the hot wall in the channel, $T_R^* = 1$. If the cold wall is set at a higher temperature than the hot wall, then they switch with the cold wall becoming the hot wall, and the hot wall becoming the cold wall. This prevents temperature difference ratio from ever exceeding a value of 1. This becomes a crucial characteristic of a unidirectional flow in a vertical channel because it limits the range of asymmetrical cases.

Similar to the unidirectional case, the bidirectional case can be encompassed by the range $-1 < T_R^* < 1$. This can be proved mathematically by the following.

If $T_H - T_\infty > |T_C - T_\infty|$, then the standard temperature difference ratio is used:

$$T_R^* = \frac{T_C - T_\infty}{T_H - T_\infty} \tag{E.1}$$

and if $T_H - T_\infty < |T_C - T_\infty|$, then a modified temperature difference ratio is used:

$$T_{RM}^* = \frac{T_H - T_\infty}{T_C - T_\infty} \tag{E.2}$$

Again, this will be a crucial characteristic for further study in the bidirectional case because the range of cases is reduced. A couple sample cases are calculated to show how the modified temperature difference ratio works.

In sample case 1 shown in Figure E.1(a), the hot wall of the channel is 305 K, the cold wall is 290 K, and the ambient is 300 K. In this case, the dominant flow is in the downwards direction, but there is some fluid flow in the upwards direction as well. Solving for equation (E.2):

$$T_H - T_\infty < |T_C - T_\infty| \rightarrow 305 - 300 < |290 - 300| \rightarrow 5 < 10$$

$$T_{RM}^* = \frac{T_H - T_\infty}{T_C - T_\infty} = \frac{305 - 300}{290 - 300} = \frac{5}{-10} = -0.5$$

In the similar sample case 2 shown in Figure E.1(b), the hot wall of the channel is 310 K, the cold wall is 295 K, and the ambient is 300 K. The dominant flow is in the upwards direction in this case, but again there is still some fluid flow in the downwards direction. Solving for equation (E.1) in this case:

$$T_H - T_\infty > |T_C - T_\infty| \rightarrow 310 - 300 > |295 - 300| \rightarrow 10 > 5$$

$$T_R^* = \frac{T_C - T_\infty}{T_H - T_\infty} = \frac{295 - 300}{310 - 300} = \frac{-5}{10} = -0.5$$

Both these cases would produce a different temperature difference ratio if using the standard temperature difference ratio, but by using a modified temperature difference ratio both cases produce the same value. This is accomplished because a similar fluid flow is produced in each case, only in opposite directions. This is shown in Figure E.1, where case 1 has a downward dominant flow and case 2 has an upward dominant flow. This figure shows the approximate boundary layer to show the dominant flow in each case. This characteristic range can be used to simply the amount of cases required to obtain a range of useful data.

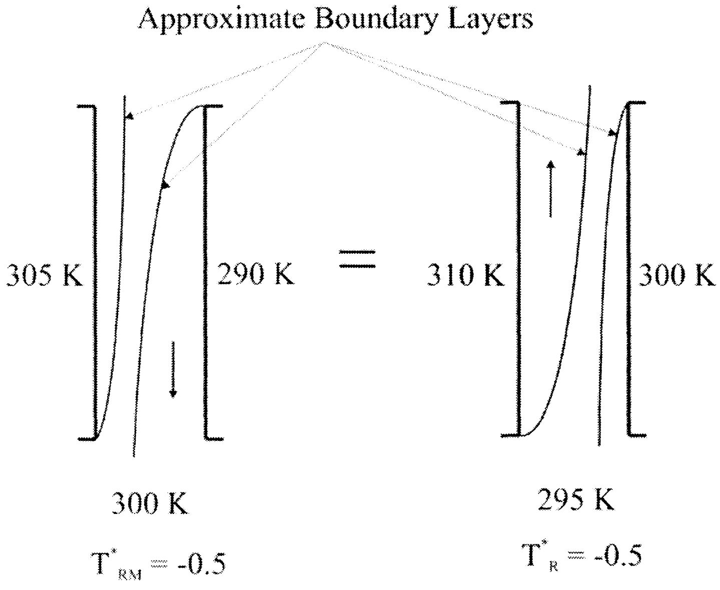

(a) (b)

Figure E.1: (a) Sample case 1 and (b) sample case 2 of a bidirectional flow in an asymmetrically, isothermally heated vertical channel.

E.3 Results of a Bidirectional Flow in an Asymmetrically Heated Vertical Channel

Some initial results were created for bidirectional flow in an asymmetrically, isothermally heated vertical channel. These results were created with Grid 2 from Chapter 2 using Fluent (2005). The methodology of Chapter 2 was utilized to obtain the solutions presented here. The results are presented in Figure E.2, where the overall channel average Nusselt numbers for various T_R^* are presented over a wide range of modified Rayleigh numbers. The overall channel average Nusselt numbers are determined for four different temperature difference ratios: $T_R^* = 0.0$, $T_R^* = -0.25$, $T_R^* = -0.5$, and $T_R^* = -.075$. Figure E.2 shows that for negative temperature difference ratios, the data does not fall onto the overall channel average Nusselt number correlation of Raithby and Hollands (1998). This shows that a more detailed study is required to develop a correlation that will fit the data at negative T_R^*. At higher modified Rayleigh numbers, there are fewer data points for the negative temperature difference ratios. This is because

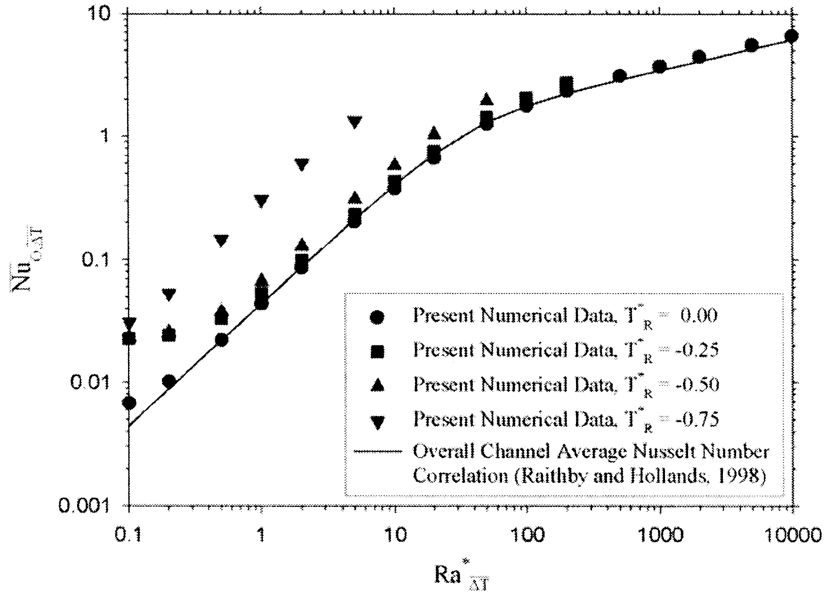

Figure E.2: Variation of the overall average Nusselt number based on $\overline{\Delta T}$ with modified Rayleigh number for bidirectional flow in a vertical channel.

as $T_R^* \rightarrow -1$, the CFD solution would not converge at higher modified Rayleigh numbers. This is due to the nature of the fluid flow in these cases. The fluid wants to flow in opposite directions on each channel wall, which causes instability when trying to solve in the laminar regime. The flow may be becoming turbulent, which will need to be addressed in a more detailed study. It should be noted that these results are the basic data taken from the CFD solution. There has been no parametric study conducted to attempt to correlate the bidirectional flow data. A more extensive study would require a detailed analysis of the data to obtain useable correlations of a bidirectional asymmetrically, isothermally heated vertical channel.

REFERENCES

Aihara, T., 1963, "Natural Convective Heat Transfer Between Vertical Parallel Plates," Transactions of the JSME, Vol. 29, pp 903 – 909.

Andreozzi, A., Manca, O., and Naso, V., 2002, "Natural Convection in Vertical Channels with an Auxiliary Plate," International Journal of Numerical Methods for Heat & Fluid Flow, Vol. 12, pp. 716 – 734.

Aung, W., Fletcher, L. S., and Sernas, V., 1972, "Developing Laminar Free Convection Between Vertical Flat Plates with Asymmetric Heating," International Journal of Heat and Mass Transfer, Vol. 15, pp. 2293-2308.

Aung, W., 1972, "Fully Developed Laminar Free Convection Between Vertical Plates Heated Asymmetrically," International Journal of Heat and Mass Transfer, Vol. 15, pp. 1577-1580.

Bar-Cohen, A. and Rohsenow, W. M., 1984, "Thermally Optimum Spacing of Vertical, Natural Convection Cooled, Parallel Plates," Journal of Heat Transfer, Vol. 106, pp. 116-123.

Bianco, N. and Nardini, S., 2005, "Numerical Analysis of Natural Convection in Air in a Vertical Convergent Channel with Uniformly Heated Conductive Walls," International Communications in Heat and Mass Transfer, Vol. 32, pp. 758 – 769.

Bodoia, J. R. and Osterle, J. F., 1962, "The Development of Free Convection Between Heated Vertical Plates," Journal of Heat Transfer, Vol. 84, pp. 40-44.

Boyalakuntla, D. S., Murthy, J. Y. and Amon, C. H., 2004, "Computation of Natural Convection in Channels with Pin Fins," IEEE Transactions on Components and Packaging Technologies, Vol. 27, pp. 138 – 146.

Campo, A., Manca, O. and Morrone, B., 2005, "Natural Convection in Vertical, Parallel-Plate Channels with Appended Unheated Entrances," International Journal for Numerical Methods in Heat & Fluid Flow, Vol. 15, pp. 183 – 203.

Chappidi, P. R. and Eno, B. E., 1990, "A Comparative Study of the Effect of Inlet Conditions on a Free Convection Flow in a Vertical Channel," Transactions of the ASME, Vol. 112, pp. 1082 – 1085.

Cho, S. H., Shin, K. S., and Zaheer-Ussin, M., 1995, "The Effect of Slat Angle of Windows with Venetian Blinds on Heating and Cooling Loads of Buildings in South Korea," Energy, Vol. 20, pp. 1225 – 1236.

Churchill, S. W. and Chu, H. H. S., 1975 "Correlating Equations for Laminar and Turbulent Free Convection from a Vertical Plate," International Journal of Heat Mass Transfer, Vol. 18, pp. 1323 – 1329.

Churchill, S. W. and Usagi, R., 1972, "A General Expression for the Correlation of Rates of Transfer and Other Phenomena," AIChE Journal, Vol. 18, No. 6, pp. 1121-1128.

Collins, M., 2001, "Analysis of Solar Heat Gain and Thermal Transmission for Windows with Louvered Shade Systems," Department of Mechanical Engineering, Queen's University, Kingston, Canada.

Collins, M., 2004, "Convective Heat Transfer Coefficients from an Internal Window Surface and Adjacent Sunlit Venetian Blind," Energy and Buildings, Vol. 36, pp. 309 – 318.

Collins, M. and Harrison, S. J., 1999, "Calorimetric Measurement of the Inward-Flowing Fraction of Absorbed Solar Radiation in Venetian Blinds," ASHRAE Transactions, Vol. 105, Part 2, pp. 1 – 9.

Collins, M. and S. J. Harrison, S. J., Naylor, D. and Oosthuizen, P. H., 2002a, "Heat Transfer From an Isothermal Vertical Surface With Adjacent Heated Horizontal Louvers: Numerical Analysis," Transactions of the ASME, Vol. 124, pp.1072 – 1077.

Collins, M., Harrison, S. J., Naylor, D. and Oosthuizen, P. H., 2002b, "Heat Transfer From an Isothermal Vertical Surface With Adjacent Heated Horizontal Louvers: Validation," Transactions of the ASME, Vol. 124, pp.1078 – 1087.

Currie, I. G. and Newman, W. A., 1970, "Natural Convection Between Isothermal Vertical Surfaces," Papers Presented at the Fourth International Heat Transfer Conference, Paris, France, pp. 1 – 8.

Desrayaud, G. and Fichera, A., 2002, "Laminar Natural Convection in a Vertical Isothermal Channel with Symmetric Surface-Mounted Rectangular Ribs," International Journal of Heat & Fluid Flow, Vol. 23, pp. 519 – 529.

Duarte, N., Naylor, D., Oosthuizen, P. H. and Harrison, S. J., 2001, "An Interferometric Study of Free Convection at a Window Glazing with a Heated Venetian Blind," Heating, Ventilating, Air Conditioning and Refrigerating Research, Vol. 7, pp. 169 – 184.

Elenbaas, W., 1942, "Heat Dissipation of Parallel Plates by Free Convection", Physica, Vol. 9, no. 1, pp. 1 – 28.

ESP-r, 2005, "ESP-r Software, Building Energy Simulation Code," Version 10.12, University of Strathclyde, Glasgow, United Kingdom. Available from: <http://www.esru.strath.ac.uk>

Fang, X. D. and Ge, X. S., 1993, "Experimental Study of Overall Heat Transfer Coefficients of the Glass Window with Venetian Blinds," Journal of Solar Energy, Vol. 14, pp. 138 – 142.

Fedorov, A. G. and Viskanta, R., 1997, "Turbulent Natural Convection Heat Transfer in an Asymmetrically Heated, Vertical Parallel-Plate Channel," International Journal of Heat and Mass Transfer, Vol. 40, pp. 3849 – 3860.

Fluent, 2004, Fluent Incorporated, Fluent version 6.2.16.

Finlayson, E. U., Arasteh, D. K., Huizenga, C., Rubin, M. D. and Reilly. M. D., 1993, "WINDOW 4.0: Documentation of Calculation Procedures," Energy and Environmental Division, Lawrence Berkeley Laboratory, Berkeley, United States.

Garnet, J. M., Fraser, R. A., Sullivan, H. F. and Wright, J. L., 1995, "Effect of Internal Venetian Blinds on Window Center-Glass U-Values," In Proceedings of Window Innovations, Toronto, Canada, pp. 273 – 279.

Guo, Z. Y., Song, Y. Z. and Zhao, X. W., 1988, "Experimental Investigation on Natural Convection in Channel by Laser Speckle Photography," Proceedings of the First World Conference on Experimental Heat Transfer, Fluid Mechanics, and Thermodynamics, Dubrovnik, Yugoslavia, pp. 412 – 418.

Habib, M. A., Said, S. A. M., Ahmed, S. A. and Asghar, A., 2002, "Velocity Characteristics of Turbulent Natural Convection in Symmetrically and Asymmetrically Heated Vertical Channels," Experimental Thermal and Fluid Science, Vol. 26, pp. 77 – 87.

Higuera, F. J. and Ryazantsev, Y. S., 2002, "Natural Convection Flow Due to a Heat Source in a Vertical Channel," International Journal of Heat & Mass Transfer, Vol. 45, pp. 2207 – 2212.

Hottel, H. C., 1967, Radiative Transfer, McGraw Hill, New York, United States.

Huang, N. Y. T., 2005, "Thermal Performance of Double Glazed Windows with Inter-Pane Venetian Blinds," Department of Mechanical Engineering, University of Waterloo, Waterloo, Canada.

Huang, N. Y. T., Wright, J. L. and Collins, M., 2006, "Thermal Resistance of a Window with an Enclosed Venetian Blind: Guarded Heater Plate Measurements," ASHRAE Transactions, Vol. 112, No. 2, pp. 13 – 21.

Incropera, F. P. and DeWitt, D. P., 2002, "Appendix A: Thermophysical Properties of Matter," Introduction to Heat Transfer 4th Ed., John Wiley & Sons, Inc., New York, United States, pp. 817 – 844.

IPCC, 2007, "Climate Change 2007: The Physical Science Basis," Working Group 1 Contribution to the IPCC Fourth Assessment Report, 2007.

Karim, F., Farouk, B. and Namer, I., 1986, "Natural Convection Heat Transfer From a Horizontal Cylinder Between Vertical Confining Adiabatic Walls," Journal of Heat Transfer, Vol. 108, pp. 291 – 298.

Kettleborough, C. F., 1971, "Transient Laminar Free Convection Between Heated Vertical Plates Including Entrance Effects," International Journal of Heat and Mass Transfer, Vol. 15, pp. 883 – 896.

Khodary, K. and Bhattacharyya, T. K., 2006, "Optimum Natural Convection from Square Cylinder in Vertical Channel," International Journal of Heat and Fluid Flow, Vol. 27, pp. 167 – 180.

Klems, J. H., 1994a, "A New Method for Predicting the Solar Heat Gain of a Complex Fenestration System: Overview and Derivation of the Matrix Layer Calculation," ASHRAE Transactions, Vol. 100, Part 1, pp. 1065 – 1072.

Klems, J. H., 1994a, "A New Method for Predicting the Solar Heat Gain of a Complex Fenestration System: Detailed Description of the Matrix Layer Calculation," ASHRAE Transactions, Vol. 100, Part 1, pp. 1073 – 1086.

Klems, J. H. and Kelley, G. O., 1996, "Calorimetric Measurements of Inward-Flowing Fraction for Complex Glazing and Shading Systems," ASHRAE Transactions, Vol. 102, Part 1, pp.947 – 954.

Kim, S. H., Anand, N. K. and Aung, W., 1990, "Effect of conduction on free convection between asymmetrically heated vertical plates: Uniform Wall Heat Flux," International Journal of Heat and Mass Transfer, Vol. 33, pp. 1013 – 1023.

Kotey, N. A. and Wright, J. L., 2006, "Simplified Solar Optical Calculations for Windows with Venetian Blinds", Proceedings of the 31st Conference of the Solar Energy Society of Canada, Montreal, Canada, pp. 1 – 8.

Lomanowski, B. A. and Wright, J. L., 2007, "Heat Transfer Analysis of Windows with Venetian Blinds: A Comparative Study," Proceedings of the 2nd Canadian Solar Buildings Conference, Calgary, Canada, pp. 1 – 9.

Lauber, T. S. and Welch, A. U., 1966, "Natural Convection Heat Transfer Between Vertical Flat Plates with Uniform Heat Flux," Proceedings of the Third International Heat Transfer Conference, Chicago, United States, pp. 126 – 131.

Machin, A. D., Harrison, S. J., Naylor, D. and Oosthuizen, P. H., 1998, "Experimental Study of Free Convection at an Indoor Glazing Surface with a Venetian Blind," HVAC&R Research, Vol. 4, No. 2, pp. 153 – 166.

Marcondes, F., Melo, V. S. and Gurgel, J. M., 2006, "Numerical Analysis of Natural Convection in Parallel, Convergent, and Divergent Open-Ended Channels," International Journal of Numerical Methods for Heat & Fluid Flow, Vol. 16, pp. 304 – 323.

Marsters, G. F., 1975, "Natural Convective Heat Transfer From a Horizontal Cylinder in the Presence of Nearby Walls," The Canadian Journal of Chemical Engineering, Vol. 53, pp. 144 – 149.

Martin, L., Raithby, G. D. and Yovanovich, M. M., 1991, "On the Low Rayleigh Number Asymptote for Natural Convection Through an Isothermal, Parallel-Plate Channel," Journal of Heat Transfer, Vol. 113, pp. 899 – 113.

Matlab, 2004, The Mathworks, Inc., Matlab Version 7.0.0.19920 (R14).

Miyatake, O. and Fujii, T., 1972, "Free Convective Heat Transfer Between Vertical Parallel Plates – One Plate Isothermally Heated and the Other Thermally Insulated", Heat Transfer – Japanese Research, Vol. 3, pp. 30-38.

Miyatake, O. and Fujii, T., 1973, "Natural Convective Heat Transfer between Vertical Parallel Plates with Unequal Heat Fluxes", Heat Transfer – Japanese Research, Vol. 3, pp. 29-33.

Nakamura, H., Asako, Y. and Naitou, T., 1982, "Heat Transfer by Free Convection Between Two Parallel Flat Plates," Numerical Heat Transfer, Vol. 5, pp. 95 – 106.

Naylor, D. and Lai, B. Y., 2007, "Experimental Study of Natural Convection in a Window with a Between-Panes Venetian Blind," Experimental Heat Transfer, Vol. 20, pp. 1 – 17.

Naylor, D., Duarte, N., Petryk, J. and Machin. A. D., 2000, "Flow- and Temperature-Field Visualization of a Window with a Heated Louvered Blind," Journal of Flow Visualization & Imaging Processing, Vol. 7, pp. 243 – 253.

Naylor, D., Shahid, H., Harrison, S. J. and Oosthuizen, P. H., 2006, "A Simplified Method for Modelling the Effect of Blinds on Window Thermal Performance," International Journal of Energy Research, Vol. 30, pp. 471 – 488.

Ostrach, S., 1953, "An Analysis of Laminar Free Convection Flow and Heat Transfer About a Flat Plate Parallel to the Direction of the Generating Body Force," National Advisory Committee for Aeronautics Report No. 1111.

Patamkar, S. V., 1980, "Numerical Heat Transfer and Fluid Flow," Hemisphere, Washington, United States.

Phillips, J., Naylor, D., Oosthuizen, P. H. and Harrison, S. J., 2001, "Numerical Study of Convective and Radiative Heat Transfer from a Window Glazing with a Venetian Blind," International Journal of Heating Ventilating, Air-Conditioning and Refrigerating Research, Vol. 7, pp. 383 – 402.

Raithby, G. D. and Hollands, K. G. T, 1998, "Chapter 4 Natural Convection," Handbook of Heat Transfer, 3rd Edition, ed. W. M. Rohsenow, J. P. Harnett, Y. I Cho, McGraw-Hill, New York, United States.

Ramanathan, S. and Kumar, R., 1991, "Correlations for Natural Convection between Heated Vertical Plates," Journal of Heat Transfer, Vol. 113, pp. 97 – 107.

Rheault, S. and E. Bilgen, E., 1989 "Heat Transfer Analysis in an Automated Venetian Blind Window System," Journal of Solar Energy Engineering, Vol. 111, pp. 89 – 95.

Rheault, S. and Bilgen, E., 1990, "Experimental Study of Full-Size Automated Venetian Blind Windows," Solar Energy, Vol. 44, pp. 157 – 160.

Shahid, H. and Naylor, D., 2005, "Energy Performance Assessment of a Window with a Horizontal Venetian Blind," Energy and Buildings, Vol. 36, pp. 836 – 843.

Touloukian, Y. S. and Makita, T., 1970, "Specific Heat: Nonmetallic Liquids and Gases," Thermophysical Properties of Matter, Vol. 6, pp. 293 – 295.

Touloukian, Y. S., Liley, P. E., and Saxena, S.C., 1970, "Thermal Conductivity: Nonmetallic Liquids and Gases," Thermophysical Properties of Matter, Vol. 3, pp. 512 – 513.

Touloukian, Y. S., Saxena, S. C., and Hestermans, P., 1975, "Viscosity," Thermophysical Properties of Matter, Vol. 11, pp. 611 – 612.

TRNSYS, 2000, "TRNSYS: A Transient Simulation Program," Version 1.5, Solar Energy Laboratory, University of Wisconsin-Madison, Madison, United States.

Van Doormal, J. P. and Raithby, G. D., 1984, "G. D. Enhancement of the Simple Method for Predicting Incompressible Flows," Numerical Heat Transfer, Vol. 7, pp. 147 – 163.

Webb, B. W. and Hill, D. P., 1989, "High Rayleigh Number Laminar Natural Convection in an Asymmetrically Heated Vertical Channel," Journal of Heat Transfer, Vol. 111, pp. 649 – 656.

Wiebelt, J. A., 1966, Engineering Radiation Heat Transfer, Holt, Rinehart, and Winston Inc, Toronto, Canada.

Wirtz, R. A. and Haag, T., 1985, "Effect of Unheated Entry on Natural Convection Between Vertical Parallel Plates," ASME Winter Annual Meeting, Miami Beach, United States, pp. 1 – 8.

Wright, J. L., 1992, "Glazing System Thermal Analysis," CANMET, Advanced Glazing System Laboratory, VISION3, Minister of Supply Services Canada, University of Waterloo, Waterloo, Canada.

Wright, J. L. and Kotey, N. A., 2006, "Solar Absorption by Each Element in a Glazing/Shading Layer Array," ASHRAE Transactions, Vol. 112, pp. 3 – 12.

Yahoda, D. S. and Wright, J. L., 2004a, "Heat Transfer of a Between-Panes Venetian Blind Using Effective Long-wave Radiative Properties," ASHRAE Transactions, Vol. 110, Part 1, pp. 455 – 462.

Yahoda, D. S. and Wright, J. L., 2004b, "Methods for Calculating the Effective Long-wave Radiative Properties of a Venetian Blind Layer," ASHRAE Transactions, Vol. 110, Part 1, pp. 463 – 473.

Yahoda, D. S. and Wright, J. L., 2005, "Methods for Calculating the Effective Solar-Optical Properties of a Venetian Blind Layer," ASHRAE Transactions, Vol. 111, Part 1, pp. 572 – 586.

Ye, P., 1997, "Effect of Venetian Blinds on Overall Heat Transfer through Window Systems: A Finite Element Numerical Solution," MESc Thesis, Department of Mechanical Engineering, Queen's University, Kingston, Canada.